

1       MEASUREMENT OF ELECTROWEAK PRODUCTION OF  
2       SAME-SIGN W BOSON PAIRS WITH ATLAS (WORKING  
3                   TITLE)

4                   William Kennedy DiClemente

5                   A DISSERTATION  
6                   in  
7                   Physics and Astronomy

8                   Presented to the Faculties of The University of Pennsylvania  
9                   in Partial Fulfillment of the Requirements for the Degree of Doctor of Philosophy  
10                  2019 *Last compiled: January 31, 2019*

---

11  
12                  I. Joseph Kroll, Professor, Physics  
13                   Supervisor of Dissertation

---

14  
15                  Joshua Klein, Professor, Physics  
16                   Graduate Group Chairperson

17                  Dissertation Committee  
18                  Elliot Lipeles, Associate Professor, Physics  
19                  Christopher Mauger, Associate Professor, Physics  
20                  Burt Ovrut, Professor, Physics  
21                  Justin Khoury, Professor, Physics  
22                  I. Joseph Kroll, Professor, Physics

23 MEASUREMENT OF ELECTROWEAK PRODUCTION OF SAME-SIGN W BOSON PAIRS  
24 WITH ATLAS (WORKING TITLE)

25 COPYRIGHT  
26 2019  
27 William Kennedy DiClemente

28 All rights reserved.

---

## Acknowledgements

---

<sup>30</sup> I'd like to thanks the Ghosts of Penn Students Past for providing me with such an amazing thesis  
<sup>31</sup> template.

32

## ABSTRACT

33 MEASUREMENT OF ELECTROWEAK PRODUCTION OF SAME-SIGN W BOSON PAIRS  
34 WITH ATLAS (WORKING TITLE)

35

William Kennedy DiClemente

36

J. Kroll

37

This is the abstract text.

---

# Contents

---

39	<b>Acknowledgements</b>	iii
40	<b>Abstract</b>	iv
41	<b>Contents</b>	v
42	<b>List of Tables</b>	ix
43	<b>List of Figures</b>	xii
44	<b>Preface</b>	xviii
45	<b>1 Introduction</b>	1
46	<b>2 Theoretical Framework</b>	2
47	2.1 Introduction to the Standard Model . . . . .	2
48	2.2 Electroweak symmetry breaking and the Higgs boson . . . . .	4
49	2.3 Diboson physics . . . . .	7
50	<b>3 LHC and the ATLAS Detector</b>	9
51	3.1 The Large Hadron Collider . . . . .	9
52	3.2 The ATLAS Detector . . . . .	9
53	3.2.1 The Inner Detector . . . . .	9
54	3.2.1.1 Pixel Detector . . . . .	9
55	3.2.1.2 Semiconductor Tracker . . . . .	9
56	3.2.1.3 Transition Radiation Tracker . . . . .	9

57	3.2.2	The Calorimeters . . . . .	10
58	3.2.2.1	Liquid Argon Calorimeters . . . . .	10
59	3.2.2.2	Tile Calorimeters . . . . .	10
60	3.2.3	The Muon Spectrometer . . . . .	10
61	3.2.4	Particle reconstruction . . . . .	11
62	3.2.4.1	Track reconstruction . . . . .	11
63	3.2.4.2	Muon reconstruction . . . . .	11
64	3.2.4.3	Electron reconstruction . . . . .	11
65	3.2.4.4	Jet reconstruction . . . . .	11
66	<b>4</b>	<b>Alignment of the ATLAS Inner Detector</b>	<b>12</b>
67	4.1	The alignment method . . . . .	13
68	4.1.1	Alignment levels . . . . .	16
69	4.1.2	Alignment coordinate systems . . . . .	17
70	4.2	Early 2015 alignment of the ATLAS detector . . . . .	19
71	4.2.1	June alignment procedure . . . . .	20
72	4.2.2	Alignment results . . . . .	21
73	4.2.2.1	Residual distributions from collisions . . . . .	22
74	4.2.2.2	Track parameter resolution from cosmic rays . . . . .	24
75	4.2.3	Error scaling . . . . .	25
76	4.3	Level 2 alignment of the TRT . . . . .	28
77	4.4	Momentum bias from sagitta deformations . . . . .	29
78	4.4.1	Sagitta bias monitoring with electron $E/p$ . . . . .	31
79	4.4.1.1	Measuring $\langle E/p \rangle$ . . . . .	32
80	4.4.1.2	Results in 13 TeV data . . . . .	34
81	<b>5</b>	<b>Measurement of same-sign <math>WW</math> production at <math>\sqrt{s} = 13</math> TeV with ATLAS</b>	<b>37</b>
82	5.0.2	Theoretical overview of vector boson scattering . . . . .	37
83	5.0.3	Same-sign $W^\pm W^\pm$ scattering . . . . .	39
84	5.0.4	Overview of backgrounds . . . . .	41
85	5.1	Data and Monte Carlo samples . . . . .	43
86	5.1.1	Monte Carlo samples . . . . .	43
87	5.2	Object and event selection . . . . .	44

88	5.2.1 Object selection . . . . .	44
89	5.2.1.1 Muon candidate selection . . . . .	45
90	5.2.1.2 Electron candidate selection . . . . .	47
91	5.2.1.3 Jet candidate selection . . . . .	47
92	5.2.1.4 Treatment of overlapping objects . . . . .	47
93	5.2.2 Signal event selection . . . . .	49
94	5.3 Background estimations . . . . .	51
95	5.3.1 Estimation of the $WZ$ background . . . . .	51
96	5.3.2 Estimation of the $V\gamma$ background . . . . .	52
97	5.3.3 Estimation of backgrounds from charge misidentification . . . . .	54
98	5.3.3.1 Validation of the charge misidentification estimate . . . . .	57
99	5.3.4.4 Estimation of non-prompt backgrounds with the fake factor method . . . . .	58
100	5.3.4.1 Overview of the default fake factor method . . . . .	58
101	5.3.4.2 The fake factor with $p_T^{\text{cone}}$ . . . . .	59
102	5.3.4.3 Application of the fake factor . . . . .	61
103	5.3.4.4 Systematic uncertainties . . . . .	66
104	5.3.4.5 Results of the fake factor . . . . .	66
105	5.3.4.6 Validation of the fake factor . . . . .	68
106	5.3.5 Reduction of $WZ$ background using custom overlap removal . . . . .	71
107	5.4 Cross section measurement . . . . .	74
108	5.4.1 Maximum likelihood fit . . . . .	75
109	5.4.2 Definition of the fiducial volume . . . . .	77
110	5.4.3 Cross section extraction . . . . .	78
111	5.5 Summary of uncertainties . . . . .	79
112	5.5.1 Experimental uncertainties . . . . .	80
113	5.5.2 Theoretical uncertainties . . . . .	81
114	5.5.2.1 Uncertainties from EWK-QCD interference . . . . .	81
115	5.6 Results . . . . .	82
116	<b>6 Prospects for same-sign <math>WW</math> at the High Luminosity LHC</b>	87
117	6.0.1 Analysis Overview . . . . .	88
118	6.1 Theoretical motivation . . . . .	88
119	6.1.1 Experimental sensitivity to longitudinal polarization . . . . .	89

120	6.2 Monte Carlo samples . . . . .	89
121	6.3 Background estimations . . . . .	91
122	6.3.1 Truth-based isolation . . . . .	92
123	6.4 Object and event selection . . . . .	93
124	6.4.1 Object selection . . . . .	93
125	6.4.2 Event selection . . . . .	93
126	6.5 Selection optimization . . . . .	94
127	6.5.1 Random grid search algorithm . . . . .	94
128	6.5.2 Inputs to the optimization . . . . .	96
129	6.5.3 Results of the optimization . . . . .	97
130	6.6 Results . . . . .	98
131	6.6.1 Event yields . . . . .	98
132	6.6.2 Uncertainties . . . . .	104
133	6.6.3 Cross section measurement . . . . .	104
134	6.6.4 Longitudinal scattering significance . . . . .	105
135	<b>7 Conclusion</b>	109
136	<b>A Additional material on truth isolation</b>	110
137	<b>B Additional material on <math>W^\pm W^\pm jj</math> measurement at <math>\sqrt{s} = 13\text{TeV}</math></b>	111
138	B.1 Impact of experimental uncertainty on MC background estimations . . . . .	111
139	<b>Bibliography</b>	113

---

## List of Tables

---

141	4.1	The four alignment levels for each of the detector subsystems. The total number of alignable structures and degrees of freedom (DoF) to be aligned are given for each level.	18
143	4.2	Summary of the highest level of alignment applied to each ID subsystem when deriving the June alignment. . . . .	21
145	4.3	Estimated value of the error scaling term $b$ for each subdetector component with the June alignment. . . . .	28
147	5.1	Predicted cross sections for EQK and QCD production of diboson processes relevant to VBS at $\sqrt{s} = 8\text{TeV}$ using the <b>SHERPA</b> MC generator. Loose generator level cuts are applied on lepton $p_T > 5\text{ GeV}$ , dilepton invariant mass $m_{ll} > 4\text{ GeV}$ , and at least two jets with $m_{jj} > 10\text{ GeV}$ . . . . .	40
151	5.2	Summary of MC samples used in the analysis. . . . .	45
152	5.3	Muon selection criteria. All muons are required to pass the preselection (top), and then either the signal (middle) or loose (bottom) criteria is applied to the preselected electrons. . . . .	46
154	5.4	Electron selection criteria. All electrons are required to pass the preselection (top), and then either the signal (middle) or loose (bottom) criteria is applied to the preselected electrons. . . . .	48
157	5.5	Jet selection criteria. All jets are required to pass the above selection in order to be used in the analysis. . . . .	48
159	5.6	Summary of the overlap removal procedure used in the analysis. If the criteria in the “check” column is met, in the “result” column, the object on the left of the arrow is removed in favor of the object on the right. . . . .	49
162	5.7	Summary of trigger requirements for electrons and muons for $\sqrt{s} = 13\text{TeV}$ data collected in 2015 and 2016. At least one of the triggers must be satisfied. . . . .	50
164	5.8	The signal event selection. . . . .	51
165	5.9	Event yields in the $WZ$ control region before normalization. All lepton flavor channels are combined. . . . .	52
167	5.10	Selection criteria for the $V\gamma$ control region. . . . .	53
168	5.11	Event yields in the $V\gamma$ control region. The $V\gamma$ scale factor of 1.77 is calculated by scaling up the $Z\gamma$ and $Z+\text{jets}$ backgrounds to account for the difference between the data and predicted total background. . . . .	54
171	5.12	Selection criteria for the same-sign inclusive validation region. . . . .	57

---

172	5.13 Event selection for the dijet region used for calculating the fake factor. The selected lepton can pass either the nominal (signal) or loose selections. In the case of the nominal leptons, the $p_T > 27$ GeV requirement is replaced with $p_T > 15$ GeV. . . . .	63
173		67
174		
175	5.14 Values of the fake factor in each $p_T$ bin and for each individual systematic source. . . . .	67
176		
177	5.15 Estimated yields for the fake lepton background. The estimated yield is shown in the first column together with the statistical uncertainty followed by the systematic uncertainties from variations of the the fake factors within their statistical (stat.) and systematic (syst.) uncertainties. The labels $f_e$ and $f_\mu$ indicate the fake factors for electrons and muons, respectively. . . . .	67
178		
179		
180		
181	5.16 Selection criteria for the same-sign top fakes validation region. . . . .	68
182		
183	5.17 Custom OR definition. Leptons must pass this selection in order to be counted for the trilepton veto. . . . .	74
184		
185	5.18 Definition of the fiducial volume. . . . .	77
186		
187	5.19 Impact of various systematic effects on the fiducial cross section measurement. The impact of a given source of uncertainty is computed by performing the fit with the corresponding nuisance parameter varied up or down by one standard deviation from its nominal value. . . . .	79
188		
189	5.20 List of sources of experimental uncertainties on the reconstruction of physics objects. . . . .	80
190		
191	5.21 Impact of experimental uncertainties for the $W^\pm W^\pm jj$ EWK processes in all channels. . . . .	81
192		
193	5.22 Impact of experimental uncertainties for the $WZ$ process in all channels. . . . .	81
194		
195	5.23 The set of generator level cuts used for generating the interference samples with <code>MadGraph</code> . . . . .	82
196		
197	5.24 Cross sections for each different $W^\pm W^\pm jj$ production mode (inclusive, EWK only, QCD only, and interference only) generated using <code>MadGraph</code> . The cross sections are calculated using a minimal set of generator level cuts from events where the $W$ decays to a muon. . . . .	82
198		
199	5.25 Table of the data and prediction event yields in the signal region before the fit. Numbers are shown for the six lepton flavor and charge channels and for all channels combined. Here the $WZ$ background yields are normalized to the data in the $WZ$ control region. The background estimations from the fake factor are included in the “Non-prompt” category, and backgrounds from $V\gamma$ production and electron charge misidentification are combined in the “ $e/\gamma$ conversions” category. Finally, $ZZ$ , $VVV$ , and $t\bar{t}V$ backgrounds are combined in the “Other prompt” category. . . . .	83
200		
201		
202		
203	5.26 Table of the data and prediction event yields in the signal region after the fit. Numbers are shown for the six lepton flavor and charge channels and for all channels combined. The background estimations from the fake factor are included in the “Non-prompt” category, and backgrounds from $V\gamma$ production and electron charge misidentification are combined in the “ $e/\gamma$ conversions” category. Finally, $ZZ$ , $VVV$ , and $t\bar{t}V$ backgrounds are combined in the “Other prompt” category. . . . .	84
204		
205		
206		
207		
208		
209	6.1 Summary of MC samples used in the analysis. . . . .	91
210	6.2 Truth-based isolation requirements for electrons and muons. . . . .	92
211	6.3 Summary of the signal event selection. . . . .	94
212	6.4 Updates to the $W^\pm W^\pm jj$ event selection criteria after optimization. Cuts not listed remain unchanged from the default selection in Table 6.3. . . . .	98
213		
214	6.5 Signal and background event yields using the default event selection for an integrated luminosity of $\mathcal{L} = 3000 \text{ fb}^{-1}$ . Events containing a fake or charge-flipped electron are removed from their respective sources and combined into a single entry each. . . . .	102
215		
216		
217	6.6 Signal and background event yields using the optimized event selection for an integrated luminosity of $\mathcal{L} = 3000 \text{ fb}^{-1}$ . Events containing a fake or charge-flipped electron are removed from their respective sources and combined into a single entry each. . . . .	102
218		
219		

220	6.7 Summary of estimated experimental and rate uncertainties. . . . .	104
221	A.1 Event yields prior to applying any form of truth-based isolation criteria. . . . .	110
222	A.2 Event yields after applying a test version of the truth-based isolation. . . . .	110
223	B.1 Experimental systematics uncertainties for the $W^\pm W^\pm jj$ QCD processes in all channels.	111
224	B.2 Experimental systematics uncertainties for triboson process in all channels. . . . .	111
225	B.3 Experimental systematics uncertainties for $t\bar{t}V$ processes in all channels. . . . .	112
226	B.4 Experimental systematics uncertainties for the $W\gamma$ process in all channels. . . . .	112
227	B.5 Experimental systematics uncertainties for the $Z\gamma$ process in all channels. . . . .	112
228	B.6 Experimental systematics uncertainties for the $ZZ$ process in all channels. . . . .	112

---

## List of Figures

---

230    2.1	An illustration of the potential term $V(\phi)$ in the cases where $\mu^2 > 0$ (left) and $\mu^2 < 0$ (right). The right-hand plot shows the Higgs potential, or ‘‘Mexican hat potential’’, with the minimum at $ \phi  = \sqrt{-\frac{\mu^2}{\lambda}}$ rather than at $ \phi  = 0$ as in the left-hand plot. . . . .	5
233    2.2	Vector boson fusion involving triple gauge couplings (left) and vector boson scattering involving a quartic gauge coupling (right). . . . .	7
235    2.3	Diboson diagrams involving the $s$ -channel (left) and $t$ -channel (right) exchanges of a Higgs boson. . . . .	8
237    3.1	General cut-away view of the ATLAS detector. . . . .	10
238    4.1	Graphical representation of the effect of a misaligned detector element. The reconstructed particle track (dashed arrow) differs from the actual trajectory of the particle (solid arrow) due to the shift in one of the detector elements. The cyan lines represent the track-to-hit residuals. . . . .	13
242    4.2	Graphical representation of the ID alignment chain. . . . .	16
243    4.3	A schematic representation of the Inner Detector in the longitudinal plane with the global coordinate system overlaid on top. The Pixel detector and IBL are shown in blue, the SCT in green, and the TRT in red. The local coordinates for each subdetector module are inset on the right. . . . .	19
247    4.4	The $d_0$ distributions with respect to the reconstructed primary vertex using the $\sqrt{s} = 13\text{TeV}$ collision data sample reconstructed using the June (black) and March (green) alignments. The data is compared to a MC simulation using a perfect detector geometry (red). The distributions are normalized to the same number of entries. . . . .	22
251    4.5	Local $x$ (left) and local $y$ (right) residual distributions of the IBL planar sensors using the $\sqrt{s} = 13\text{TeV}$ collision data sample reconstructed using the June (black) and March (green) alignments. The data is compared to a MC simulation using a perfect detector geometry (red). The distributions are normalized to the same number of entries. . . . .	23
255    4.6	The mean of the local $x$ (left) and local $y$ (right) residual distributions as a function of the global $z$ position of each IBL module using the $\sqrt{s} = 13\text{TeV}$ collision data sample reconstructed using the June (black) and March (green) alignments. The data is compared to a MC simulation using a perfect detector geometry (red). . . . .	24

259	4.7 Local $x$ (top) and local $y$ (bottom) residual distributions for the Pixel barrel (excluding 260 the IBL, left) and end-caps (right) using the $\sqrt{s} = 13\text{TeV}$ collision data sample recon- 261 structed using the June (black) and March (green) alignments. The data is compared to a 262 MC simulation using a perfect detector geometry (red). The distributions are normalized 263 to the same number of entries. . . . .	25
264	4.8 Local $x$ residual distributions for the SCT barrel (left) and end-caps (right) using the 265 $\sqrt{s} = 13\text{TeV}$ collision data sample reconstructed using the June (black) and March 266 (green) alignments. The data is compared to a MC simulation using a perfect detector 267 geometry (red). The distributions are normalized to the same number of entries. . . . .	26
268	4.9 Residual distributions for the TRT barrel (left) and end-caps (right) using the $\sqrt{s} =$ 269 $13\text{TeV}$ collision data sample reconstructed using the June (black) and March (green) 270 alignments. The data is compared to a MC simulation using a perfect detector geometry 271 (red). The distributions are normalized to the same number of entries. . . . .	26
272	4.10 Representation of splitting a single cosmic ray track passing through the entire detector 273 (left) into two separate tracks (right). . . . .	27
274	4.11 Distribution of the difference in the impact parameter $\Delta d_0$ (left) and charge over trans- 275 verse momentum $\Delta q/p_T$ (right) between the two cosmic ray split tracks. The June 276 (black) and March (green) alignments are compared. The distributions are normalized 277 to the same number of entries. . . . .	27
278	4.12 Pull distributions in local $x$ (left) and $y$ (right) for the IBL using the $\sqrt{s} = 13\text{TeV}$ collision 279 data sample after applying the error scaling. . . . .	28
280	4.13 Residual means by straw layer in two TRT $\phi$ -sectors affected by a tilt misalignment. The 281 tilts in each of the three modules are clearly visible in the red points representing the 282 reconstructed data prior to alignment. After four iterations of L2 alignment, the residual 283 means in the gray points are flat. . . . .	29
284	4.14 Two dimensional map of residuals in the first layer of the TRT barrel vs $z$ and $\phi$ . Each 285 bin represents the mean of a Gaussian fit to the TRT residuals in that bin. The map on 286 the left is after the L3 (wire-by-wire) alignment of the TRT performed in 2010, and the 287 map on the right is after the L2 alignment at the end of 2015. The $z$ -axis for both plots 288 use the same scale. . . . .	30
289	4.15 Representation of a curl distortion in the detector. The image shows a cutaway in the 290 transverse plane. The deformation is represented by the red arrows, and the impact on 291 the reconstructed positive (blue) and negative (green) tracks are shown. The dashed lines 292 represent the true particle trajectories, and the solid lines represent the reconstructed 293 trajectories. . . . .	31
294	4.16 Geometric definition of the sagitta $s$ in relation to the length of the chord $l$ and the radius 295 $r$ of a circular arc. . . . .	31
296	4.17 $E/p$ distributions of electrons and positrons in two different $\eta$ - $\phi$ bins of the detector. The 297 left hand plot is taken from a region with no momentum bias where $\langle E/p \rangle^+ = \langle E/p \rangle^-$ , 298 while the right hand plot shows an 8% disagreement in $\langle E/p \rangle$ between electrons and 299 positrons. . . . .	33
300	4.18 Sagitta bias in the $\sqrt{s} = 13\text{TeV}$ data collected by ATLAS in 2016 as a function of $\eta$ and 301 $\phi$ for the prompt (left) and reprocessed (right) alignments using the $E/p$ method. . . . .	35
302	4.19 Sagitta bias in the $\sqrt{s} = 13\text{TeV}$ data collected by ATLAS in 2016 projected along $\eta$ for 303 the prompt (gray) and reprocessed (blue) alignments using the $E/p$ method. . . . .	35
304	4.20 Sagitta bias in the $\sqrt{s} = 13\text{TeV}$ data collected by ATLAS in 2017 as a function of $\eta$ 305 and $\phi$ in reconstructed electrons (left) and after two iterations of momentum corrections 306 (right) from the $E/p$ method. . . . .	35

307	4.21 Sagitta bias in the $\sqrt{s} = 13\text{TeV}$ data collected by ATLAS in 2017 projected along $\eta$ in 308 reconstructed electrons (gray) and after one (red) and two (blue) iterations of momentum 309 corrections from the $E/p$ method. . . . .	36
310	5.1 Cross sections in nanobarns for five different scattering processes of longitudinally polarized 311 vector bosons as a function of center of mass energy $\sqrt{s}$ . Without a SM Higgs boson 312 (left), the cross sections grow unbounded with $\sqrt{s}$ ; however with a 120 GeV Higgs boson 313 (right), the cross sections no longer diverge. . . . .	38
314	5.2 Tree-level Feynman diagrams for VBS EWK $VVjj$ production including triple gauge 315 couplings involving $W$ and/or $Z$ bosons (top left and top middle), quartic gauge coupling 316 (top right), or the exchange of a Higgs boson ( $s$ -channel bottom left and $t$ -channel bottom 317 right). The labels are quarks ( $q$ ), fermions ( $f$ ), and gauge bosons ( $V = W, Z$ ). . . . .	39
318	5.3 Tree-level Feynman diagrams for non-VBS EWK $VVjj$ production. The labels are quarks 319 ( $q$ ), fermions ( $f$ ), and gauge bosons ( $V = W, Z$ ). . . . .	39
320	5.4 Tree-level Feynman diagrams for QCD $VVjj$ production. The labels are quarks ( $q$ ), 321 fermions ( $f$ ), and gauge bosons ( $V = W, Z$ ). . . . .	40
322	5.5 Feynman diagrams for VBS EWK production of $W^\pm W^\pm jj$ events. The leftmost diagram 323 contains a quartic gauge coupling vertex, and the rightmost diagram contains an exchange 324 of a Higgs boson. <b>TODO: Make diagrams consistent with others</b> . . . . .	41
325	5.6 $W^\pm W^\pm jj$ VBS event topology containing two leptons (1 and 2) with the same elec- 326 tric charge, two neutrinos, and two forward tagging jets (3 and 4) with large rapidity 327 separation $\Delta y$ . . . . .	41
328	5.7 Generator level comparisons at $\sqrt{s} = 8\text{TeV}$ of dijet invariant mass ( $m_{jj}$ , left) and dijet 329 rapidity ( $\Delta y_{jj}$ , right) in EWK (red) and QCD (blue) $W^\pm W^\pm jj$ events. Both data sets 330 have been normalized to the same area. . . . .	42
331	5.8 ATLAS event display of a $pp \rightarrow W^+ W^+ \rightarrow \mu^+ \nu_\mu \mu^+ \nu_\mu jj$ event. The muons are rep- 332 resented by the red lines travelling from the ID through the MS, and the forward jets 333 are represented by the blue cones with yellow energy deposits in the calorimeters. The 334 direction of the $E_T^{\text{miss}}$ in the transverse plane is indicated by the gray dashed line in the 335 inset image. . . . .	42
336	5.9 Leading lepton $p_T$ (left) and $\eta$ (right) distributions in the $WZ$ control region before 337 normalization. All lepton channels are combined. . . . .	53
338	5.10 Trilepton invariant mass $m_{lll}$ distribution in the $WZ$ control region before normalization. 339 All lepton channels are combined. . . . .	53
340	5.11 Charge misidentification rates for electrons as a function of $ \eta $ and $p_T$ . Rates are calcu- 341 lated from $Z \rightarrow e^+ e^-$ MC after applying scale factors to approximate the charge mis-ID 342 rates in data. . . . .	55
343	5.12 Dilepton invariant mass distribution $m_{ll}$ for the $ee$ channel in the same-sign inclusive VR.	57
344	5.13 $p_T$ distributions for the leading (left) and subleading (right) electron for the $ee$ channel 345 in the same-sign inclusive VR. In these plots, the cut requiring $m_{ee}$ to fall within the $Z$ 346 mass window has been inverted in order to test the modelling away from the $Z$ peak. .	58
347	5.14 $\Delta p_T$ distributions for nominal (blue) and loose (red) muons in simulated $t\bar{t}$ events. Each 348 muon has been matched to a truth-level jet. Both distributions are normalized to unit 349 area. . . . .	60
350	5.15 $\Delta p_T$ distributions for muons (top) and electrons (bottom) in simulated $t\bar{t}$ events. Each 351 lepton has been matched to a truth-level jet, and that truth jet has had its $p_T$ corrected 352 to include all truth muons within a cone of $\Delta R < 0.4$ . The nominal leptons are in black. 353 $\Delta p_T$ is calculated for the loose leptons using $p_T$ (red) and $p_T + p_T^{\text{cone}}$ (blue). . . . .	62
354	5.16 Distributions of $p_T^{\text{cone}}/p_T$ for nominal (black) and loose (red) muons in simulated $t\bar{t}$ events.	63

355	5.17	The measured fake factor as a function of muon $p_T + p_T^{\text{cone}}$ . The error bars represent the statistical uncertainty only. . . . .	64
356			
357	5.18	The measured fake factor as a function of electron $p_T + p_T^{\text{cone}}$ in the central ( $ \eta  < 1.37$ , blue) and forward ( $ \eta  > 1.37$ , red) regions of the detector. The error bars represent the statistical uncertainty only. . . . .	64
358			
359			
360	5.19	Graphical representation of the fake factor application using $p_T + p_T^{\text{cone}}$ . The value of $p_T + p_T^{\text{cone}}$ for the loose lepton is used to “look up” the fake factor weight which is then applied to the event. The loose lepton’s $p_T$ becomes $p_T + p_T^{\text{cone}}$ for the purpose of the fake background estimation. . . . .	65
361			
362			
363			
364	5.20	Systematic variations in the fake factor as a function of muon $p_T + p_T^{\text{cone}}$ . The individual fake factors obtained for each systematic variation are displayed with their statistical uncertainties. . . . .	68
365			
366			
367	5.21	Systematic variations in the fake factor as a function of electron $p_T + p_T^{\text{cone}}$ in the central ( $ \eta  < 1.37$ , top) and forward ( $ \eta  > 1.37$ , bottom) regions of the detector. The individual fake factors obtained for each systematic variation are displayed with their statistical uncertainties. . . . .	69
368			
369			
370			
371	5.22	Distributions of the subleading lepton $p_T$ in the same-sign top fakes VR for $\mu^\pm\mu^\pm$ events (top right), $e^\pm e^\pm$ events (top left), $\mu^\pm e^\pm$ events (bottom left), and all events combined (bottom right). All errors are statistical only. . . . .	70
372			
373			
374	5.23	Pseudorapidity ( $\eta$ ) distributions of truth muons (top) and electrons (bottom) for Sherpa $W^\pm W^\pm jj$ and $WZ$ MC samples. The blue vertical lines represent the allowed $\eta$ range for each lepton flavor. The numbers correspond to the number of raw MC events that fall within and outside of the allowed $\eta$ range for each MC sample. . . . .	72
375			
376			
377			
378	5.24	Distributions of $p_{T,\text{ratio}}(\mu, j)$ for EWK and QCD $W^\pm W^\pm jj$ signal (black) and $WZ$ background (teal) for truth-matched third muons in events that pass the trilepton veto. Both distributions are normalized to unit area. The associated efficiency curves are on the right where efficiency is defined as the percentage of total events that would pass a cut on $p_{T,\text{ratio}}(\mu, j)$ at a given value on the $x$ -axis. . . . .	72
379			
380			
381			
382			
383	5.25	Distributions of $\Delta R(\mu, j)$ for EWK and QCD $W^\pm W^\pm jj$ signal (black) and $WZ$ background (teal) for truth-matched third muons in events that pass the trilepton veto. Both distributions are normalized to unit area. The associated efficiency curves are on the right where efficiency is defined as the percentage of total events that would pass a cut on $\Delta R(\mu, j)$ at a given value on the $x$ -axis. . . . .	73
384			
385			
386			
387			
388	5.26	Distributions of $p_{T,\text{ratio}}(e, j)$ for EWK and QCD $W^\pm W^\pm jj$ signal (black) and $WZ$ background (teal) for truth-matched third electrons in events that pass the trilepton veto. Both distributions are normalized to unit area. The associated efficiency curves are on the right where efficiency is defined as the percentage of total events that would pass a cut on $p_{T,\text{ratio}}(e, j)$ at a given value on the $x$ -axis. . . . .	73
389			
390			
391			
392			
393	5.27	Two-dimensional plots of $p_{T,\text{ratio}}(\mu, j)$ vs $\Delta R(\mu, j)$ for truth-matched third muons in events that pass the trilepton veto for EWK and QCD $W^\pm W^\pm jj$ signal (left) and $WZ$ background (right). The blue overlay indicates the area in which the third leptons will pass the custom OR and result in the event failing the trilepton veto. . . . .	74
394			
395			
396			
397	5.28	Visual representation of the different kinematic regions relevant to the cross section measurement. The acceptance factor $\mathcal{A}$ converts from the truth level total phase space to the truth level fiducial region, and the efficiency correction $\mathcal{C}$ translates the fiducial region in to the reconstruction level signal region. . . . .	78
398			
399			
400			

401	5.29	The dijet invariant mass $m_{jj}$ distributions for data and predicted signal and background in the signal region after the fit. The shaded band represents the statistical and systematic uncertainties added in quadrature. Note that the bins have been scaled such that they represent the number of events per 100 GeV in $m_{jj}$ . The background estimations from the fake factor are included in the “Non-prompt” category, and backgrounds from $V\gamma$ production and electron charge misidentification are combined in the “ $e/\gamma$ conversions” category. Finally, $ZZ$ , $VVV$ , and $t\bar{t}V$ backgrounds are combined in the “Other prompt” category. . . . .	84
409	5.30	The event yields for data and predicted signal and background in the $WZ$ and low- $m_{jj}$ control regions after the fit. The shaded band represents the statistical and systematic uncertainties added in quadrature. The background estimations from the fake factor are included in the “Non-prompt” category, and backgrounds from $V\gamma$ production and electron charge misidentification are combined in the “ $e/\gamma$ conversions” category. Finally, $ZZ$ , $VVV$ , and $t\bar{t}V$ backgrounds are combined in the “Other prompt” category. . . . .	85
415	5.31	Comparison of the measured $W^\pm W^\pm jj$ EWK fiducial cross section with theoretical calculations from <b>SHERPA v2.2.2</b> and <b>POWHEG-BOX v2</b> . The light orange band represents the total experimental uncertainty on the measured value, and the dark orange hashed band is the statistical uncertainty. For the simulations, the light blue band represents the total theoretical uncertainty, and the dark blue hashed band are the scale uncertainties. The theory predictions do not include the interference between the EWK and QCD production. . . . .	86
422	6.1	Comparison of the leading (top) and subleading (bottom) lepton $p_T$ distributions for purely longitudinal (LL, black) and mixed polarization (LT+TT, cyan) $W^\pm W^\pm jj$ events. . . . .	90
424	6.2	Comparison of the azimuthal dijet separation ( $ \Delta\phi_{jj} $ ) for purely longitudinal (LL, black) and mixed polarization (LT+TT, cyan) $W^\pm W^\pm jj$ events. . . . .	91
426	6.3	A visual representation of a rectangular grid search algorithm. The signal events are the blue triangles, and the red circles are the background events. <b>TODO: replace with own figure</b> . . . . .	95
429	6.4	A visual representation of a random grid search algorithm. The signal events are the blue triangles, and the red circles are the background events. <b>TODO: replace with own figure</b> . . . . .	96
432	6.5	Leading lepton $p_T$ distribution. The default and optimized cuts are represented by the red and green dashed lines, respectively. The $W^\pm W^\pm jj$ EWK signal (black points) is normalized to the same area as the sum of the backgrounds (colored histogram). <b>TODO: Move to appendix or omit</b> . . . . .	99
436	6.6	Dilepton invariant mass distribution. The default and optimized cuts are represented by the red and green dashed lines, respectively. The $W^\pm W^\pm jj$ EWK signal (black points) is normalized to the same area as the sum of the backgrounds (colored histogram). <b>TODO: Move to appendix or omit</b> . . . . .	99
440	6.7	Leading (top) and subleading (bottom) jet $p_T$ distributions. The default and optimized cuts are represented by the red and green dashed lines, respectively. The $W^\pm W^\pm jj$ EWK signal (black points) is normalized to the same area as the sum of the backgrounds (colored histogram). . . . .	100
445	6.8	Dijet invariant mass distribution. The default and optimized cuts are represented by the red and green dashed lines, respectively. The $W^\pm W^\pm jj$ EWK signal (black points) is normalized to the same area as the sum of the backgrounds (colored histogram). <b>TODO: Move to appendix or omit</b> . . . . .	101

---

448	6.9	Lepton-jet centrality distribution. The default and optimized cuts are represented by the red and green dashed lines, respectively. The $W^\pm W^\pm jj$ EWK signal (black points) is normalized to the same area as the sum of the backgrounds (colored histogram). . . . .	101
450			
451	6.10	$p_T$ distributions for the leading jet using the default (left) and optimized (right) event selections for all channels combined. . . . .	103
452			
453	6.11	$p_T$ distributions for the subleading jet using the default (left) and optimized (right) event selections for all channels combined. . . . .	103
454			
455	6.12	$p_T$ distributions for lepton-jet centrality $\zeta$ using the default (left) and optimized (right) event selections for all channels combined. . . . .	103
456			
457	6.13	Projections of the statistical (black), theoretical (blue), systematic (yellow), and total (red) uncertainties on the measured cross section as a function of integrated luminosity using the optimized event selection. . . . .	105
458			
459			
460	6.14	Dijet azimuthal separation ( $ \Delta\phi_{jj} $ ) for the low $m_{jj}$ region ( $520 < m_{jj} < 1100$ GeV, top) and the high $m_{jj}$ region ( $m_{jj} > 1100$ GeV, bottom). The purely longitudinal (LL, gray) is plotted separately from the mixed and transverse (LT+TT, cyan) polarizations. . . . .	107
461			
462			
463	6.15	Projections of the expected longitudinal scattering significance as a function of integrated luminosity when considering all sources of uncertainties (black) or only statistical uncertainties (red). . . . .	108
464			
465			

---

## Preface

---

<sup>467</sup> This is the preface. It's optional, but it's nice to give some context for the reader and stuff.

Will K. DiClemente

Philadelphia, February 2019

469

## CHAPTER 1

---

470

# Introduction

---

471 The Standard Model (SM)<sup>1</sup> has been remarkably successful...

---

<sup>1</sup>Here's a footnote.

## CHAPTER 2

---

# Theoretical Framework

---

474 This chapter outlines the theoretical groundwork for the rest of the thesis. An overview of the Stan-  
 475 dard Model of particle physics (SM) is given in Section 2.1, followed by the electroweak symmetry  
 476 breaking mechanism involving the Higgs boson in Section 2.2. Finally, Section 2.3 will go into some  
 477 detail on the interests of diboson physics specifically.

478 **2.1 Introduction to the Standard Model**

479 The Standard Model of particle physics serves as a mathematical description of the fundamental  
 480 particles of the universe and their interactions. It has been developed over the course of the past  
 481 century, incorporating both predictions from theory and results from experiments. All in all, the SM  
 482 has proven remarkably successful in accurately describing particle interactions seen in experiments.

483 The SM is a quantum field theory (QFT) [1, 2] in which the fundamental particles are represented  
 484 as excited states of their corresponding fields. The spin- $\frac{1}{2}$  fermionic fields give rise to the quarks  
 485 and leptons comprising ordinary matter, the spin-1 fields correspond to the electroweak bosons and  
 486 the gluon which mediate the electroweak and strong forces, respectively, and finally the scalar Higgs  
 487 field is responsible for electroweak symmetry breaking. The excitations and interactions of the fields  
 488 are governed by the SM Lagrangian, which is invariant under local transformations of the group  
 489  $SU(3) \times SU(2) \times U(1)$ . **TODO: need more detail/refinement here**

490 The first quantum field theory to be developed is quantum electrodynamics (QED) [3], which  
 491 describes the electromagnetic interaction. The theory predicts the existence of a  $U(1)$  gauge field  
 492 that interacts with the electrically charged fermions. This field corresponds to the photon. A key  
 493 aspect of QED is that it is perturbative. The coupling constant  $\alpha = e^2/4\pi$  is small, where  $e$  is

494 electrical charge of the field, allowing for the use of perturbation theory in calculations. In this case,  
 495 calculations can be written as a power series in  $\alpha$ , where successive higher order terms contribute  
 496 less to the final result. **TODO: renormalizability here?**

497 The strong interaction—the theory of quarks and gluons—has also been described using QFT  
 498 as quantum chromodynamics (QCD). The symmetry group for QCD is  $SU(3)$ , and its eight gen-  
 499 erators correspond to the eight differently charged, massless gluons [4]. Unlike in QED, which has  
 500 positive and negative charges, the strong force has three “colors”. Color charge combined with the  
 501 non-Abelian nature of  $SU(3)$ , which allows the gluons to interact with each other, result in the  
 502 most well-known property of QCD: color confinement. In order to increase the separation between  
 503 two color-charged quarks, the amount of energy required increases until it becomes energetically  
 504 favorable to pair-produce a new quark-antiquark pair, which then bind to the original quarks. The  
 505 end result of this is that only color-neutral objects exist in isolation. What this means for the strong  
 506 coupling constant  $\alpha_s$  is that its value at the low energies where confinement occurs is large, on  
 507 the order of  $\alpha_s \sim 1$ . The consequence of this is that perturbation theory cannot be used to accu-  
 508 rately approximate interactions. While this appears at first to be a critical problem for predictions,  
 509 fortunately it turns out that  $\alpha_s$  “runs”, or decreases in magnitude at higher energy [5, 6]. This so-  
 510 called “asymptotic freedom” allows QCD to be calculated perturbatively [7] at energies accessible  
 511 by collider experiments including the LHC.

512 The last gauge field corresponds to the weak interaction. Ultimately, the weak  $SU(2)$  and the  
 513 electromagnetic  $U(1)$  mix to form the  $SU(2) \times U(1)$  *electroweak* (EWK) interaction [8, 9]. A more  
 514 detailed description of the mixing will be discussed in conjunction with electroweak symmetry break-  
 515 ing (EWSB) in Section 2.2; however, a summary of the resulting EWK interaction is presented here,  
 516 at the risk of some repeated information to follow. There are three weak isospin bosons arising from  
 517 the  $SU(2)$  group ( $W_\mu^1$ ,  $W_\mu^2$ , and  $W_\mu^3$ ) and one weak hypercharge boson from the  $U(1)$  group ( $B_\mu$ ).  
 518 The  $W_3$  and  $B$  bosons mix according to the weak mixing angle  $\theta_W$  to form the  $Z$  boson and the  
 519 photon according to:

$$\begin{pmatrix} \gamma \\ Z \end{pmatrix} = \begin{pmatrix} \cos \theta_W & \sin \theta_W \\ -\sin \theta_W & \cos \theta_W \end{pmatrix} \begin{pmatrix} B_\mu \\ W_\mu^3 \end{pmatrix} \quad (2.1)$$

520 The value of  $\theta_W$  is not predicted by the SM; it is one example of an experimental input to the  
 521 theory, measured to be  $\sin^2 \theta_W = 0.23153 \pm 0.00016$  [10]. The charged  $W^\pm$  bosons are a mixture of  
 522 the remaining  $W_\mu^1$  and  $W_\mu^2$  bosons:

$$W^\pm = \frac{1}{\sqrt{2}}(W_\mu^1 \mp iW_\mu^2) \quad (2.2)$$

523 Unlike the photon (and the gluon of QCD), the  $W^\pm$  and  $Z$  bosons are massive. This means that  
 524 even though SU(2) is non-Abelian, the range of interaction is short and confinement does not occur.  
 525 Lastly, the EWK interaction is chiral, only coupling to the left-handed component of the fermion  
 526 fields

527 One final field remains within the SM: the scalar Higgs field. It was originally proposed in the  
 528 1960's to explain the masses of the  $W^\pm$  and  $Z$  bosons [11, 12, 13] and is the mechanism for the  
 529 EWSB process. The particle associated with the field is a massive scalar boson, which was at last  
 530 discovered by ATLAS and CMS in 2012 [14, 15] with a mass of 125 GeV.

## 531 2.2 Electroweak symmetry breaking and the Higgs boson

532 The results of electroweak mixing and the implications of the Higgs field have been introduced  
 533 in the previous section. If the EWK theory were an unbroken symmetry, the associated  $W^\pm$  and  
 534  $Z$  bosons would be massless; however, when observed experimentally, they were found to be quite  
 535 heavy [16, 17], at around 80 GeV and 91 GeV, respectively [18]. Here, a more detailed explanation  
 536 of the Higgs mechanism and how it “spontaneously breaks” the EWK symmetry, resulting in the  
 537 three massive bosons ( $W^\pm$  and  $Z$ ) and one massless boson (photon), is presented.

538 To see how the Higgs mechanism results in the massive vector bosons and a massless photon,  
 539 consider the following. Beginning with a complex scalar doublet  $\phi$  defined as:

$$\phi = \begin{pmatrix} \phi^+ \\ \phi^0 \end{pmatrix} = \sqrt{\frac{1}{2}} \begin{pmatrix} \phi_1 + i\phi_2 \\ \phi_3 + i\phi_4 \end{pmatrix} \quad (2.3)$$

540 a Lagrangian  $\mathcal{L}$  can be written:

$$\mathcal{L} = (\mathcal{D}_\mu \phi)^\dagger (\mathcal{D}^\mu \phi) - \mu^2 \phi^\dagger \phi - \lambda(\phi^\dagger \phi)^2 \quad (2.4)$$

541 where  $\lambda > 0$  and  $\mathcal{D}_\mu$  is the covariant derivative.  $\mathcal{D}_\mu$  is defined such that  $\mathcal{L}$  is invariant under a local  
 542 SU(2)  $\times$  U(1) gauge transformation:

$$\mathcal{D}_\mu \phi = \left( \partial_\mu + \frac{ig}{2} \tau_a W_\mu^a + \frac{ig'}{2} B_\mu \right) \phi \quad (2.5)$$

543 where  $W_\mu^a$  ( $a = 1, 2, 3$ ) are the SU(2) fields with generators  $\tau_a$  and coupling constant  $g$ , and  $B_\mu$  is  
 544 the U(1) field with coupling constant  $g'$ .

545 Isolating the potential term:

$$V(\phi) = \mu^2 \phi^\dagger \phi + \lambda(\phi^\dagger \phi)^2 \quad (2.6)$$

546 a choice must be made on the sign of  $\mu^2$ , and the case of interest is for  $\mu^2 < 0$ . This results in  
 547 the famous “mexican hat potential” shown in Figure 2.1, which is minimized along the collection of  
 548 points:

$$\phi^\dagger \phi = \frac{1}{2} (\phi_1^2 + \phi_2^2 + \phi_3^2 + \phi_4^2) = -\frac{\mu^2}{2\lambda} \quad (2.7)$$

549 This means that the minimum of the potential is not at  $\phi = 0$  (as it would be in the case where  
 550  $\mu^2 > 0$ ), but rather at a value:

$$v \equiv \sqrt{-\frac{\mu^2}{\lambda}} \quad (2.8)$$

551 With no loss of generality due to the SU(2) symmetry,  $\phi_1 = \phi_2 = \phi_4 = 0$  can be set in Equation 2.7  
 552 leaving  $\phi_3^2 = v^2$ . Finally, the *vacuum expectation value* (VEV) of the field can be written as:

$$\langle \phi \rangle = \sqrt{\frac{1}{2}} \begin{pmatrix} 0 \\ v \end{pmatrix} \quad (2.9)$$

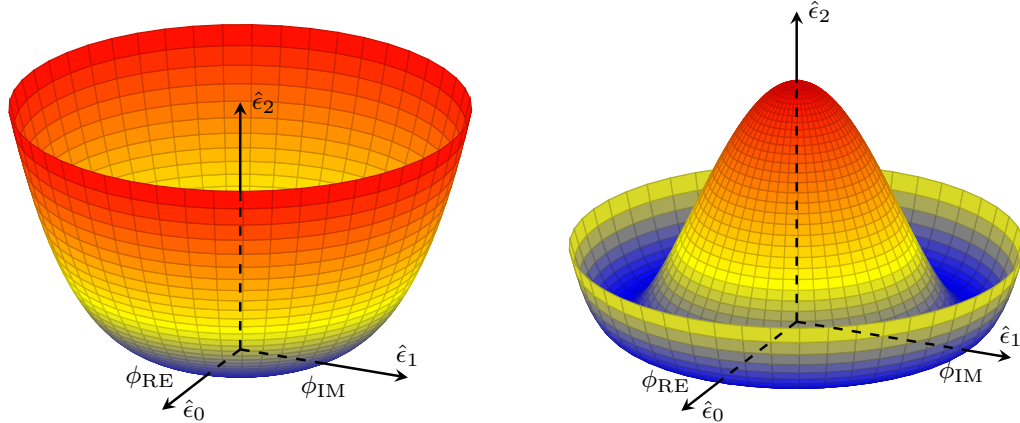


Figure 2.1: An illustration of the potential term  $V(\phi)$  in the cases where  $\mu^2 > 0$  (left) and  $\mu^2 < 0$  (right). The right-hand plot shows the Higgs potential, or “Mexican hat potential”, with the minimum at  $|\phi| = \sqrt{-\frac{\mu^2}{\lambda}}$  rather than at  $|\phi| = 0$  as in the left-hand plot.

553 The VEV can be substituted back into the original Lagrangian in Equation 2.4, and, following  
 554 quite a bit of math, a collection of mass terms can be identified:

$$\mathcal{L} \subset \mathcal{L}_M \equiv \frac{1}{8} v^2 g^2 \left[ (W_\mu^1)^2 + (W_\mu^2)^2 \right] + \frac{1}{8} v^2 \left[ g^2 (W_\mu^3)^2 - 2gg' W_\mu^3 B^\mu + g'^2 (B_\mu)^2 \right] \quad (2.10)$$

555 Focusing on the first term for the moment, substituting in Equation 2.2 for the physical  $W^\pm$  bosons,  
 556 the mass term can be seen clearly:

$$M_W^2 W^+ W^- = \left(\frac{1}{2}vg\right)^2 W^+ W^- \quad (2.11)$$

557

$$M_W = \frac{1}{2}vg \quad (2.12)$$

558 With a bit of clever forward-thinking, the second term of Equation 2.10 can be rewritten as:

$$\frac{1}{8}v^2 \left[ gW_\mu^3 - g'B_\mu \right]^2 + 0 \left[ g'W_\mu^3 - gB_\mu \right]^2 = \frac{1}{2}M_Z^2 Z_\mu^2 + \frac{1}{2}M_A^2 A_\mu^2 \quad (2.13)$$

559 where  $Z_\mu^2$  and  $A_\mu^2$  represent the physical  $Z$  boson and photon, respectively, and are defined as:

$$Z_\mu = \frac{gW_\mu^3 - g'B_\mu}{\sqrt{g^2 + g'^2}} \quad (2.14)$$

560

$$A_\mu = \frac{g'W_\mu^3 - gB_\mu}{\sqrt{g^2 + g'^2}} \quad (2.15)$$

561 From this, it can be seen that the photon is massless, and the mass of the  $Z$  boson is identified as:

$$M_Z = \frac{1}{2}v\sqrt{g^2 + g'^2} \quad (2.16)$$

562 Lastly, the Higgs field can couple directly to the fermions. Taking the electron as an example,  
 563 an additonal Lagrangian term can be written:

$$\mathcal{L}_e = -G_e [\bar{e}_L \phi e_R + \bar{e}_R \phi^\dagger e_L] \quad (2.17)$$

564 where  $e_L$  and  $e_R$  are the left-handed doublet and right-handed singlet, respectively, and  $\phi$  is as in  
 565 Equation 2.3. The symmetry can be spontaneously broken by a perturbation about the VEV:

$$\phi = \sqrt{\frac{1}{2}} \begin{pmatrix} 0 \\ v + h(x) \end{pmatrix} \quad (2.18)$$

566 which, when substituted into  $\mathcal{L}_e$  gives:

$$\begin{aligned} \mathcal{L}_e &= -\frac{G_e}{\sqrt{2}}v(\bar{e}_L e_R + \bar{e}_R e_L) - \frac{G_e}{\sqrt{2}}(\bar{e}_L e_R + \bar{e}_R e_L)h \\ &= -m_e \bar{e}e - \frac{m_e}{v} \bar{e}eh \end{aligned} \quad (2.19)$$

567 for electron mass  $m_e = \frac{G_e v}{\sqrt{2}}$ . From the second term, it can be seen that the strength of the Higgs  
 568 coupling to the electron is proportional to the mass of the electron. The rest of the fermion couplings  
 569 follow from this example.

570 What is accomplished here is quite remarkable. The weak and electromagnetic interactions have  
 571 been unified into a single  $SU(2) \times U(1)$  interaction, and the physical bosons observed in nature arise  
 572 as mixtures of the four gauge fields. Additionally, the non-zero VEV of the Higgs field results in  
 573 masses for the  $W^\pm$  and  $Z$  bosons while the photon remains massless. Additionally, it is shown that  
 574 the Higgs couples to fermions in proportion to their mass. From experimental measurements, the  
 575 value of the VEV has been determined to be  $v \approx 246$  GeV [18]. However, it should be noted that the  
 576 theory does not predict the mass of the Higgs boson or of the fermions; these must all be determined  
 577 from experiment.

### 578 2.3 Diboson physics

579 Processes involving two final state gauge bosons are of particular interest for testing the predictive  
 580 power of the SM. Due to the non-Abelian nature of the EWK interaction, the corresponding gauge  
 581 bosons are allowed to self-interact. This results in triple and quartic couplings of gauge bosons  
 582 (TGCs and QGCs, respectively). The SM allowed TGCs are the  $WW\gamma$  and  $WWZ$  vertices, and  
 583 the QGCs predicted by the model include  $WWZ\gamma$ ,  $WW\gamma\gamma$ ,  $WWZZ$ , and  $WWWW$ . These ver-  
 584 tices are accessible via a number of production modes at hadron colliders, including vector boson  
 585 fusion and scattering (VBF and VBS, as in Figure 2.2). The LHC in particular has provided the  
 586 first opportunity to observe some of these vertices, such as the  $WW\gamma\gamma$  QGC via the  $W\gamma\gamma$  final  
 587 state [19], or the  $WWWW$  QGC via same-sign  $W^\pm W^\pm$  production [20]. Precise measurements of  
 588 these processes can be compared to the theoretical predictions, and deviations can point to deficien-  
 589 cies in the prediction, such as needing an additional order in  $\alpha_s$  in the calculation, or even hints at  
 590 new physics, like anomalous gauge couplings<sup>2</sup> [21].

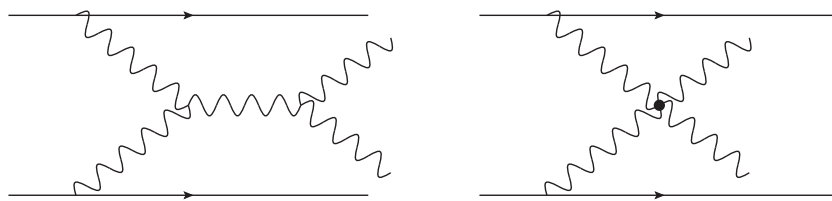


Figure 2.2: Vector boson fusion involving triple gauge couplings (left) and vector boson scattering involving a quartic gauge coupling (right).

591 Diboson interactions also make up one of the most sensitive tests of EWSB. Aside from the

---

<sup>2</sup>In the SM, the TGCs and QGCs are fixed by the electromagnetic coupling constant  $\alpha$  and the electroweak mixing angle  $\theta_W$ . In many Beyond the Standard Model scenarios, these couplings are modified by additional contributions.

592 top quark, the EWK bosons have the strongest coupling to the Higgs mechanism, as there are  
 593 several production diagrams involving the exchange of a Higgs boson, including those in Figure 2.3.  
 594 In this instance, VBS processes are particularly important as the Higgs unitarizes the scattering  
 595 amplitude [22] (this particular aspect will be explored in more detail in the context of same-sign  
 596  $W^\pm W^\pm$  scattering in Section 5.0.2). Since the Higgs boson has only recently been discovered, it has  
 597 not yet been extensively tested, and there could still be deviations in the EWSB mechanism that  
 598 may manifest in the VBF and VBS measurements [23].

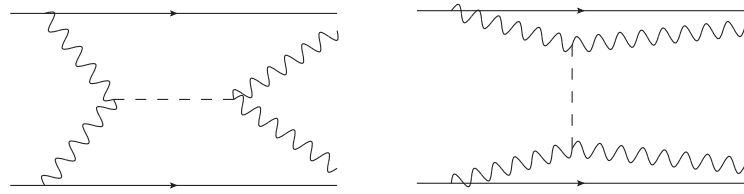


Figure 2.3: Diboson diagrams involving the  $s$ -channel (left) and  $t$ -channel (right) exchanges of a Higgs boson.

## CHAPTER 3

# LHC and the ATLAS Detector

### 601 **3.1 The Large Hadron Collider**

602 The Large Hadron Collider (LHC) [24] is...

### 603 **3.2 The ATLAS Detector**

604 ATLAS is a general-purpose particle detector...

#### 605 **3.2.1 The Inner Detector**

606 The Inner Detector serves the primary purpose of measuring the trajectories of charged particles...

##### 607 **3.2.1.1 Pixel Detector**

608 The Pixel detector consists of four cylindrical barrel layers and three disk-shaped endcap layers...

##### 609 **3.2.1.2 Semiconductor Tracker**

610 The Semiconductor Tracker uses the same basic technology as the Pixels, but the fundamental unit  
611 of silicon is a larger “strip”...

##### 612 **3.2.1.3 Transition Radiation Tracker**

613 The Transition Radiation Tracker is the outermost component of the ID...

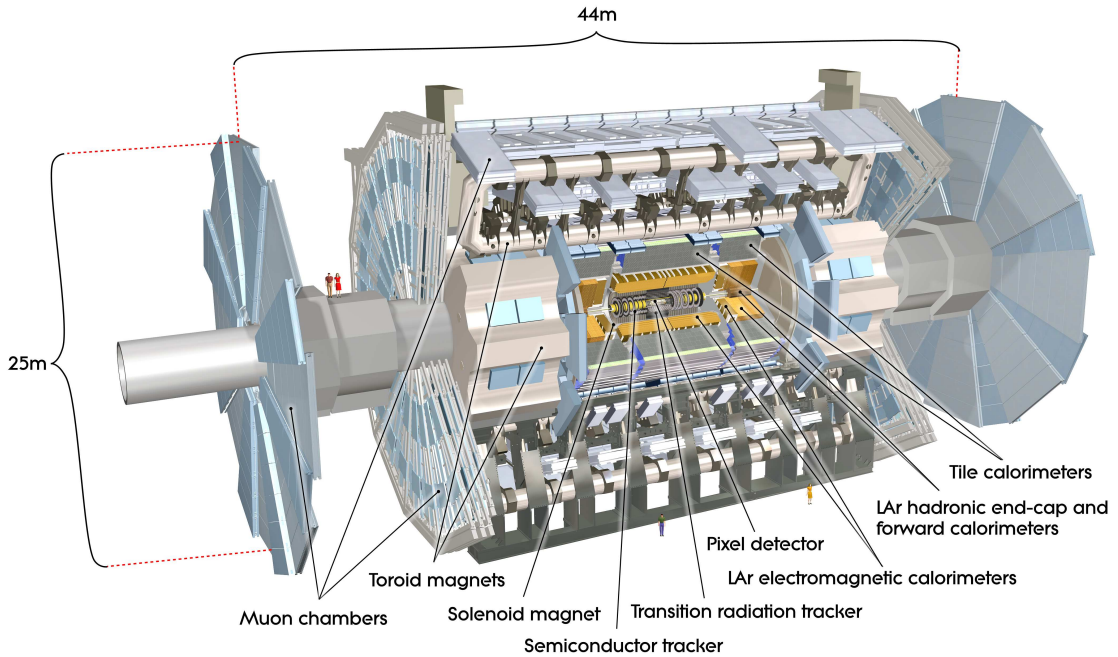


Figure 3.1: General cut-away view of the ATLAS detector [25].

### 614 3.2.2 The Calorimeters

615 ATLAS includes two types of calorimeter system for measuring electromagnetic and hadronic showers.  
 616 These are the Liquid Argon (LAr) calorimeters and the Tile calorimeters. Together, these cover  
 617 the region with  $|\eta| < 4.9\dots$

#### 618 3.2.2.1 Liquid Argon Calorimeters

619 The Liquid Argon system consists of...

#### 620 3.2.2.2 Tile Calorimeters

621 The Tile calorimeter provides coverage for hadronic showers...

### 622 3.2.3 The Muon Spectrometer

623 Muon spectrometer stuff.

624    **3.2.4 Particle reconstruction**

625    Particle reconstruction algorithms

626    **3.2.4.1 Track reconstruction**

627    **3.2.4.2 Muon reconstruction**

628    **3.2.4.3 Electron reconstruction**

629    **3.2.4.4 Jet reconstruction**

## CHAPTER 4

---

# 631 Alignment of the ATLAS Inner Detector

---

632 When a charged particle passes through the ATLAS ID, it leaves hits in the sensors along its path.  
633 In order to accurately measure the track of the particle, it is necessary to know where these hits  
634 occurred as precisely as possible, which in turn requires knowledge of the physical location of the  
635 element that registered the hit. If one of these elements is *misaligned*, or displaced relative to its  
636 position in the known detector geometry, the assumed location of the corresponding hit will not  
637 match its actual location, resulting in an incorrect track fit. These misalignments can occur for  
638 any number of reasons, including but not limited to elements shifting during maintenance periods  
639 or cycles in ATLAS’s magnetic field, or small movements during normal detector operations. The  
640 effect of a misaligned detector element on the track reconstruction is shown in Figure 4.1.

641 In order to correct the misalignments, the ID alignment procedure is applied to accurately  
642 determine the physical position and orientation of each detector element. The baseline accuracy of  
643 the alignment is required to be such that the track parameter resolutions are not degraded by more  
644 than 20% with respect to those derived from a perfect detector geometry<sup>3</sup>. This corresponds to a  
645 precision of better than  $10\mu\text{m}$  in the positioning of the elements of the silicon detectors [26].

646 This chapter outlines the ID alignment procedure, the alignment of the detector during the 2015  
647 data taking period, and the steps taken to measure momentum biases in the alignment.

---

<sup>3</sup>The so-called *perfect geometry* refers to the description of the ATLAS detector in which every sensor precisely matches its design specifications. The perfect geometry contains no misalignments, and the position of each sensor is known exactly.

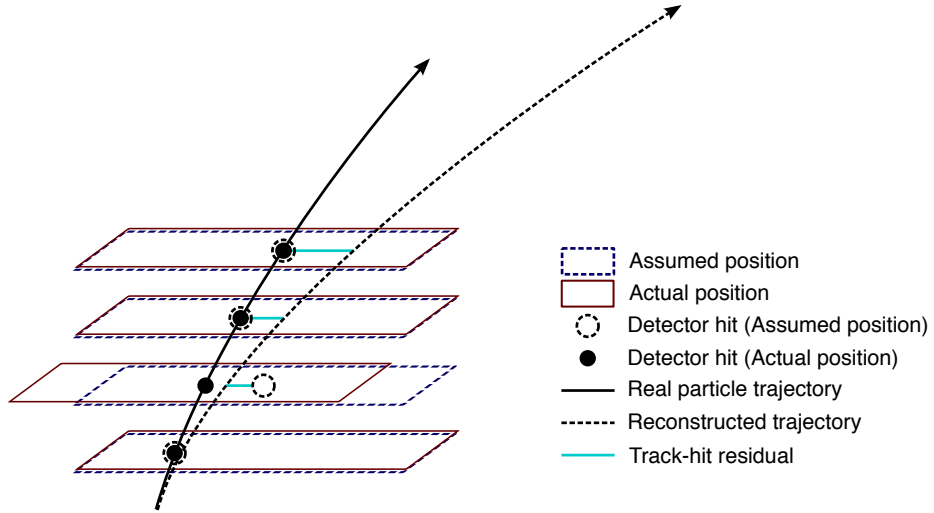


Figure 4.1: Graphical representation of the effect of a misaligned detector element. The reconstructed particle track (dashed arrow) differs from the actual trajectory of the particle (solid arrow) due to the shift in one of the detector elements. The cyan lines represent the track-to-hit residuals.

## 648 4.1 The alignment method

649 The alignment procedure uses track-based algorithm that updates the locations of detector elements  
 650 in order to minimize the set of track-hit *residuals*. These residuals are defined as the distance between  
 651 the fitted track position in a given detector element to the position of the hit recorded by the same  
 652 element, and are shown by the cyan lines in Figure 4.1. Tracks in ATLAS are parameterized as  
 653 five-dimensional vectors [27]:

$$\vec{\tau} = (d_0, z_0, \phi_0, \theta, q/p) \quad (4.1)$$

654 where  $d_0$  and  $z_0$  are the transverse and longitudinal impact parameters with respect to the origin,  
 655 respectively,  $\phi_0$  is the azimuthal angle of the track at the point of closest approach to the origin,  $\theta$   
 656 is the polar angle, and  $q/p$  is the charge of the track divided by its momentum. The residual for the  
 657  $i^{\text{th}}$  hit of a given track can then be written in terms of the track parameters  $\vec{\tau}$  and a set of alignment  
 658 parameters  $\vec{a}$  that describe the hit location [28]:

$$r_i(\vec{\tau}, \vec{a}) = (\vec{m}_i - \vec{e}_i(\vec{\tau}, \vec{a})) \cdot \hat{k} \quad (4.2)$$

659 where  $\vec{e}_i$  is the intersection point of the extrapolated track with the sensor,  $\vec{m}_i$  is the position of the  
 660 associated hit within the sensor, and  $\hat{k}$  is the unit vector defining the direction of the measurement  
 661 within the sensor.  $\vec{r}$  is then the vector of residuals for the given track.

662 A  $\chi^2$  function can be built from the residuals of all collected tracks:

$$\chi^2 = \sum_{\text{tracks}} \vec{r}^T V^{-1} \vec{r} \quad (4.3)$$

663 where  $V$  is the covariance matrix of the hit measurements. The  $\chi^2$  function is then minimized with  
664 respect to the alignment parameters  $\vec{a}$ , which contain all degrees of freedom being aligned. The  
665 minimization condition with respect to  $\vec{a}$  is:

$$\frac{d\chi^2}{d\vec{a}} = 0 \rightarrow 2 \sum_{\text{tracks}} \left( \frac{d\vec{r}}{d\vec{a}} \right)^T V^{-1} \vec{r} = 0 \quad (4.4)$$

666 This equation can be difficult to solve exactly, so the residual is rewritten as a first order Taylor  
667 expansion:

$$\vec{r} = \vec{r}_0 + \frac{d\vec{r}}{d\vec{a}} \delta\vec{a} \quad (4.5)$$

668 where  $\vec{r}_0$  is dependent on an initial set of track and alignment parameters  $\vec{r}_0$  and  $\vec{a}_0$ , respectively;  
669 the track parameter dependence has also been folded into the total derivative  $\frac{d\vec{r}}{d\vec{a}}$ . Equation 4.5 can  
670 then be inserted into the minimization condition from Equation 4.4 to give:

$$\left[ \sum_{\text{tracks}} \left( \frac{d\vec{r}}{d\vec{a}} \right)^T V^{-1} \left( \frac{d\vec{r}}{d\vec{a}} \right) \right] \delta\vec{a} + \sum_{\text{tracks}} \left( \frac{d\vec{r}}{d\vec{a}} \right)^T V^{-1} \vec{r}_0 = 0 \quad (4.6)$$

671 From this equation, the alignment matrix  $\mathcal{M}_a$  and alignment vector  $\vec{\nu}_a$  can be defined:

$$\mathcal{M}_a = \sum_{\text{tracks}} \left( \frac{d\vec{r}}{d\vec{a}} \right)^T V^{-1} \left( \frac{d\vec{r}}{d\vec{a}} \right) \quad (4.7)$$

672

$$\vec{\nu}_a = \sum_{\text{tracks}} \left( \frac{d\vec{r}}{d\vec{a}} \right)^T V^{-1} \vec{r}_0 \quad (4.8)$$

673 Finally, the alignment corrections  $\delta\vec{a}$  can be solved for by inverting the alignment matrix:

$$\delta\vec{a} = -\mathcal{M}_a^{-1} \vec{\nu}_a \quad (4.9)$$

674 which is a linear system of equations with a number of equations equal to the number of alignment  
675 degrees of freedom [29].

676 Inverting the matrix and solving this system of equations is referred to as *Global  $\chi^2$*  align-  
677 ment [28]. This can be useful, as  $\mathcal{M}_a$  contains all the correlations between the alignable structures.  
678 However, inverting the matrix becomes difficult when the number of degrees of freedom becomes  
679 large, and as the number of alignable structures increases, so too does the size of the matrix  $\mathcal{M}_a$ .  
680 Eventually inverting the matrix becomes too computationally intensive to be practical.

681 This problem is solved by the *Local*  $\chi^2$  algorithm [30]. In this case, the alignment matrix is  
 682 constructed to be block-diagonal, allowing for it to be inverted even for large numbers of degrees of  
 683 freedom. This is achieved by replacing the full derivative in Equation 4.6 with the partial derivative  
 684  $\frac{\partial \vec{r}}{\partial \vec{a}}$ . The new alignment matrix  $\mathcal{M}'_a$  and alignment vector  $\vec{\nu}'_a$  become:

$$\mathcal{M}_a = \sum_{\text{tracks}} \left( \frac{\partial \vec{r}}{\partial \vec{a}} \right)^T V^{-1} \left( \frac{\partial \vec{r}}{\partial \vec{a}} \right) \quad (4.10)$$

685

$$\vec{\nu}_a = \sum_{\text{tracks}} \left( \frac{\partial \vec{r}}{\partial \vec{a}} \right)^T V^{-1} \vec{r}_0 \quad (4.11)$$

686 Inverting  $\mathcal{M}'_a$  is considerably faster and less intensive even for large numbers of degrees of freedom;  
 687 however, the correlations between the alignable structures is lost.

688 Due to the Taylor expansion used in Equation 4.6, several iterations of the alignment algorithm  
 689 may be necessary to converge on a final set of alignment constants. The Local  $\chi^2$  alignment typically  
 690 requires more iterations due to the loss of the correlation information [31]. In practice, the ATLAS  
 691 reconstruction is run over a set of events, and the resulting tracks are fed to the alignment algorithm.  
 692 The residuals are calculated, the alignment matrix is built and inverted, and a new set of alignment  
 693 constants is obtained. The convergence of the alignment can be checked by:

694 1. Measure the  $\Delta\chi^2$  with the previous iteration. If it is near zero, then the  $\chi^2$  is approaching its  
 695 minimum.

696 2. Looking at the residual distributions for different alignable structures. A well aligned detector  
 697 will have a mean residual of zero with a width approximating the intrinsic resolution of the  
 698 detector.

699 If the above checks are satisfied, the process is finished and the final alignment constants are read  
 700 out; if not, another iteration is performed. A visual representation of the alignment chain is shown  
 701 in Figure 4.2.

702 Since a  $\chi^2$  minimization is used to align the detector, if there is a systematic misalignments in  
 703 the detector that does not adversely affect the  $\chi^2$ , the algorithm will be insensitive to it. These  
 704 misalignments are referred to as *weak modes*, and special care is taken to remove them [32]. One  
 705 potential impact of weak modes is a bias in the track momentum of reconstructed particles. This  
 706 particular effect is the subject of Section 4.4.

707 In practice, the detector is aligned both in “real-time” as data is collected, and during dedicated  
 708 offline alignment campaigns. The real-time alignment is run in ATLAS’s so-called *calibration loop*,

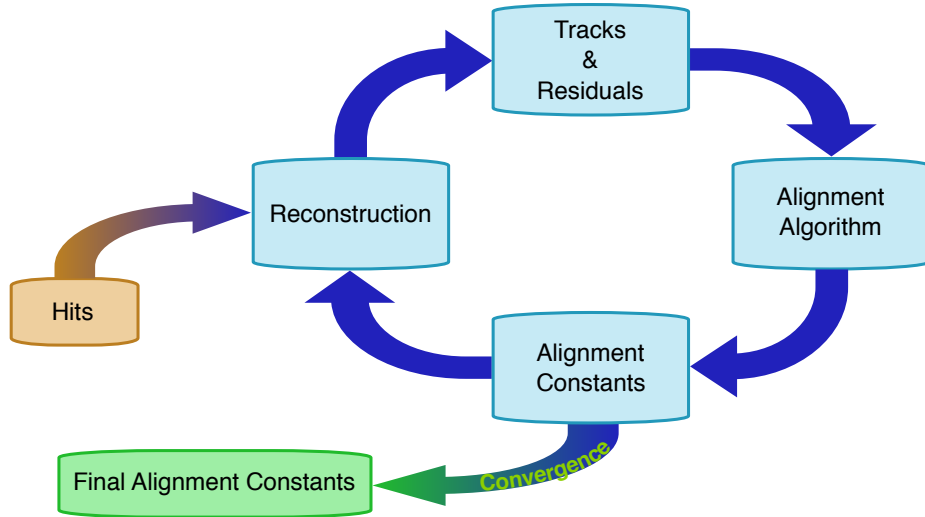


Figure 4.2: Graphical representation of the ID alignment chain.

which comprises the first stage in the preparation of data for physics analysis. The calibration loop requires the alignment as well as various other detector calibrations to be available within 48 hours for initial data processing. A fast, coarse-grained alignment<sup>4</sup> is run on a subset of the available data containing full tracking information, and the results are propagated to the reconstruction of that particular run [33]. Due to the time constraints of the calibration loop, a full sensor-by-sensor alignment is not possible.

The more thorough and finely tuned alignments are reserved for the dedicated alignment campaigns. These generally occur early in data taking campaigns, typically once a sufficient amount of data is collected after a detector shutdown, in order to obtain a good baseline alignment for use in the remainder of the data collection period. Once data taking is complete, another campaign determines an improved set of alignment constants (divided into several “blocks” to account for time-dependent misalignments), and the full data is reprocessed using the newly derived detector geometry. The initial offline alignment of the ATLAS detector at the beginning of Run 2 in 2015 is the subject of Section 4.2.

### 4.1.1 Alignment levels

The alignment of the detector is performed at several levels of increasing granularity. This adds flexibility in being able to align only as finely as needed, and it also allows for global, detector-level

<sup>4</sup>The calibration loop runs up to a Level 2 alignment in the silicon detectors, which involves treating each layer of sensors as a single object, defined in greater detail in Table 4.1.

726 misalignments to be corrected first before dealing with finer adjustments.

- 727     • Level 1 (L1) alignment involves moving entire subdetector components as a single unit, such  
728         as the entire Pixel detector, or the SCT barrel. These often have the largest misalignments,  
729         but they are easily corrected and do not require large volumes of data to do so.
- 730     • Level 2 (L2) alignment treats individual layers in the silicon detectors (modules in the TRT)  
731         and end cap disks as individual alignable objects.
- 732     • Level 2.7 (L27) alignment was introduced with the addition of the IBL to the ID in Run 2. It  
733         involves the stave-by-stave alignment of the IBL and Pixel barrel<sup>5</sup>.
- 734     • Level 3 (L3) alignment treats each sensor in the silicon detectors and each straw in the TRT  
735         as an individual alignable object. It is the finest grained alignment available but also the most  
736         computationally intensive due to the large number of degrees of freedom. The large number  
737         of individual detector sensors being aligned also requires the largest amount of statistics.

738 The different alignment levels are listed in more detail in Table 4.1, including the number of alignable  
739 structures and associated degrees of freedom for each detector component.

740 The implementation of the alignment algorithm in the software is flexible enough to allow each  
741 subsystem to be aligned individually at a specified level. Each alignable structure has six degrees of  
742 freedom: 3 translations ( $T_x, T_y, T_z$ ) and 3 rotations ( $R_x, R_y, R_z$ )<sup>6</sup>; however individual degrees of  
743 freedom may be turned on and off as required. In a typical alignment job, L1 and L2 contain few  
744 enough degrees of freedom that the Global  $\chi^2$  algorithm can be used, but L3 alignments (which can  
745 contain over 36,000 degrees of freedom in the silicon detectors alone) require the Local  $\chi^2$  algorithm.

#### 746 4.1.2 Alignment coordinate systems

747 The global coordinate system ( $x, y, z$ ) used by the ID alignment matches that of the ATLAS  
748 detector in general, as detailed in Section 3.2 TODO: update with actual location of figure when  
749 it's in.... The positions and orientations of individual detector modules of the ID are defined by  
750 a right-handed local coordinate system ( $x', y', z'$ ) where the origin is defined as the geometrical  
751 center of the module. The  $x'$ -axis for each silicon module is defined to point along the most sensitive

---

<sup>5</sup>For the purposes of this Chapter, the term “Pixel” will refer to the original three layers of the Pixel detector, and the IBL will be referenced separately.

<sup>6</sup>The TRT is an exception, as the subdetector does not have any resolution along the length of the straw. Therefore, for the barrel,  $T_z$  is omitted. Similarly for the straws themselves, only two parameters are defined: translation with respect to the radial direction ( $T_\phi$ ) and rotation with respect to the radial axis ( $R_r$  for the barrel and  $R_z$  for the end-caps) [34].

Level	Description of alignable structure	Structures	DoF
1	IBL detector	1	6
	Whole Pixel detector	1	6
	SCT barrel and 2 end-caps	3	18
	TRT barrel and 2 end-caps ( $T_z$ fixed)	3	17
Total:		8	47
2	IBL detector	1	6
	Pixel barrel layers	3	18
	Pixel end-cap disks	$2 \times 3$	36
	SCT barrel layers	4	24
	SCT end-cap disks	$2 \times 9$	108
	TRT barrel 32 modules ( $T_z$ fixed)	$3 \times 32$	480
	TRT end-cap wheels	$2 \times 40$	480
Total:		208	792
2.7	IBL staves	14	84
	Pixel barrel staves	$22+38+52$	672
	Pixel end-cap disks	$2 \times 3$	18
	Total:		132
3	IBL modules	280	1,680
	Pixel modules	1,744	10,464
	SCT modules	4,088	24,528
	TRT barrel wires ( $T_\phi, R_r$ only)	105,088	210,176
	TRT end-cap wires ( $T_\phi, R_Z$ only)	245,760	491,520
	Total silicon sensors:		6,112
	Total TRT wires:		350,848
Total:		36,672	701,696

Table 4.1: The four alignment levels for each of the detector subsystems. The total number of alignable structures and degrees of freedom (DoF) to be aligned are given for each level.

752 direction of the module, the  $y'$ -axis is oriented along the long side of the module, and the  $z'$ -axis is  
 753 orthogonal to the  $(x', y')$  plane. For the TRT straws, the  $x'$ -axis is perpendicular to both the wire  
 754 and the radial direction, defined from the origin of the global frame to the straw center, the  $y'$ -axis  
 755 points along the straw, and once again the  $z'$ -axis is orthogonal to the  $(x', y')$  plane. A depiction of  
 756 the global and local coordinate systems for the ID is shown in Figure 4.3.

757 When considering the alignment degrees of freedom listed earlier in Section 4.1.1, grouped collec-  
 758 tions of modules, layers, or entire subdetectors use the global coordinate system; individual modules  
 759 use their respective local coordinate systems. The translations  $T_i$  are with respect to the origin of  
 760 the given reference frame, and the rotations  $R_i$  are taken about the Cartesian axes.

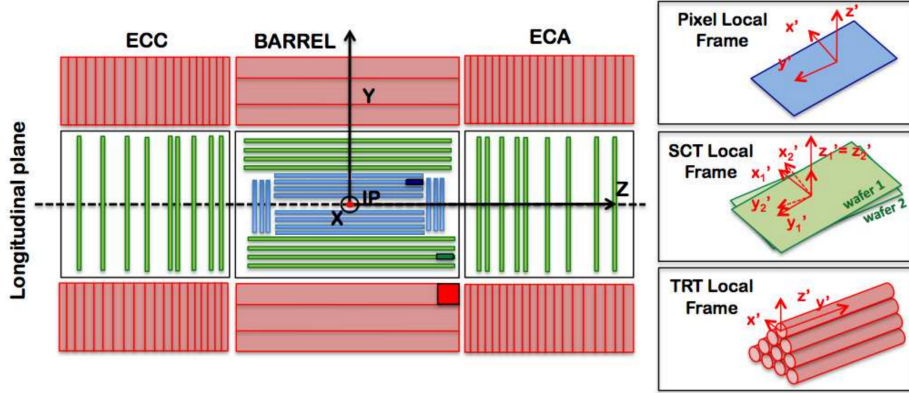


Figure 4.3: A schematic representation of the Inner Detector in the longitudinal plane with the global coordinate system overlaid on top. The Pixel detector and IBL are shown in blue, the SCT in green, and the TRT in red. The local coordinates for each subdetector module are inset on the right. Image taken from [35].

## 761 4.2 Early 2015 alignment of the ATLAS detector

762 At the end of Run 1, the LHC was shut down for upgrades and maintenance. During this time,  
 763 a number of upgrades were performed on the ATLAS detector, including the installation of a new  
 764 innermost layer of the Pixel detector, the Insertable B-Layer (IBL) [36]. **TODO: This will certainly**  
 765 **be defined in the detector description, so maybe the citation and abbreviation are not needed** These  
 766 changes to the ID required some detector components to be removed temporarily, and many elements  
 767 shifted relative to each other over the course of the maintenance process. In order to correct for these  
 768 large detector movements prior to  $\sqrt{s} = 13$  TeV collision data taking, an alignment was performed  
 769 using cosmic ray data collected in early 2015 [35]. This alignment was able to correct for the majority  
 770 of the large detector-wide misalignments as well as determine the global position of the IBL at the  
 771 micron level.

772 In June of 2015, shortly after the data taking period began, the first track-based alignment  
 773 of the refurbished ID was performed using  $\mathcal{L} = 7.9 \text{ pb}^{-1}$  of  $\sqrt{s} = 13$  TeV  $pp$  collision data [37].  
 774 Starting from the initial geometry determined by the cosmic ray alignment, referred to hereafter  
 775 as the *March alignment*, an improved set of alignment constants, called the *June alignment*, was  
 776 derived from a data set of approximately 1.4 million selected tracks. For comparison, a MC sample  
 777 containing approximately 2.7 million tracks was constructed from dijet events simulated using a  
 778 perfect detector geometry; the MC events are reweighted to match the  $\eta$  and  $p_T$  distributions found  
 779 in the data. Additional validation of the alignment results uses a set of cosmic ray data collected

780 by the detector during the LHC collisions. **TODO:** find some way of saying that this section follows  
781 the alignment note [37]? or is it ok not to...

782 **4.2.1 June alignment procedure**

783 The data set used as the input for the alignment contains a subset of physics events used for prompt  
784 reconstruction recorded at a rate of 10 Hz. To ensure that only high quality tracks are used for the  
785 alignment, each track is required to have transverse momentum  $p_T > 3$  GeV, contain at least one  
786 hit in the Pixel detector, at least seven hits in the combined silicon detectors, and at least 25 hits  
787 in the TRT.

788 A full L3 alignment of the IBL was included in the March alignment; however, a realignment  
789 was necessary. Since the cosmic rays pass through the detector top-down, the staves on the sides of  
790 the IBL could not be aligned as precisely as those on the top and bottom due to lower statistics.  
791 Additionally, the IBL was operating at a temperature of  $-20^\circ\text{C}$  during the cosmic data taking  
792 and at  $-10^\circ\text{C}$  for collision data taking. This proved to be significant, as it was observed that  
793 the IBL staves experience a temperature-dependent, parabolic bowing in the local  $x'$ -direction of  
794 approximately  $-10\mu\text{m}/\text{K}$  [38]. As a result, a full L3 alignment of the IBL was essential in order to  
795 correct for the bowing. Due to it being a brand new element of the detector as well as its importance  
796 in vertexing and  $b$  jet tagging, aligning the IBL sensors with a high degree of precision was of great  
797 importance.

798 The June alignment was performed in two stages, with the first pass focusing on relative move-  
799 ments of the big structures and correcting for the bowing of the IBL. The March alignment corrected  
800 for these larger movements as well; however, it was observed during Run 1 that these sort of mis-  
801 alignments are introduced by changing conditions in the detector [32], such as in the cooling system  
802 or magnet power cycling, which may have occurred between the early cosmic data taking and the  
803 first  $\sqrt{s} = 13$  TeV collisions. The silicon detectors were aligned at several different levels and the  
804 IBL was aligned at the module level; the TRT detector was kept fixed to act as a global reference  
805 frame. The full alignment chain for the first pass consisted of the following steps:

- 806 1. The IBL, Pixel, and SCT detectors were aligned at L1. The SCT barrel was not aligned in  
807  $T_z$  in order to constrain global displacements along the  $z$ -axis, as the TRT is not sensitive to  
808 that degree of freedom.
- 809 2. The IBL, and Pixel barrel and end-caps, and SCT barrel were aligned at L2. The SCT end-caps  
810 were aligned at L1.

811     3. The IBL and pixel barrel were aligned at L27, using all six degrees of freedom. The Pixel  
 812       end-cap disks were only aligned in the plane ( $T_x$ ,  $T_y$ , and  $R_z$ ). The SCT was treated the same  
 813       as in the previous step.

814     4. The IBL was aligned at L3 using all six degrees of freedom for each module.

815       The primary goal for the second pass was to remove a bias in the transverse impact parameter  
 816        $d_0$  present in the March alignment. The resolution of  $d_0$  was also poorer than expected. In order  
 817       to correct for this, an additional constraint was passed to the alignment by adding an impact  
 818       parameter with respect to the beam spot as a pseudo-measurement [39]. When the alignment  
 819       algorithm minimizes the  $\chi^2$ , it will take care of the impact parameter minimization as well. Only  
 820       the IBL and Pixel detectors were aligned in this step. The stages of the second pass are listed below,  
 821       and the beam spot constraint was used in each:

822       1. The IBL and Pixel detectors were aligned at L2 with the SCT fixed.

823       2. The IBL was aligned at L27

824       3. The IBL and Pixel barrel and end-caps were aligned at L3.

825       The set of alignment constants obtained at the end of the second pass represents the June alignment.  
 826       The highest level of alignment over the course of the two passes for each subdetector is listed in  
 827       Table 4.2.

Detector	Highest level of alignment	
IBL	L3	
Pixel	Barrel	L3
	End-caps	L3 ( $T_x$ , $T_y$ , and $R_z$ only)
SCT	Barrel	L2 (except $T_z$ )
	End-caps	L1
TRT	None	

Table 4.2: Summary of the highest level of alignment applied to each ID subsystem when deriving the June alignment.

### 828 4.2.2 Alignment results

829       The primary measure of alignment quality is assessed by looking at the track-hit residual distributions. If the detector is well aligned, the residuals will be Gaussian-distributed with a mean

of zero and a width approximating the detector's resolution. The residual distributions are constructed from the same selection of tracks that were used to perform the alignment, and are the focus of Section 4.2.2.1. A second check on the alignment involves observables sensitive to the track parameter resolution. In this case, cosmic rays are used, making use of a “split track” technique that takes advantage of the top-to-bottom cosmic ray trajectory (compared to the center-out trajectory of collision tracks). This method and the corresponding tests of the alignment are detailed in Section 4.2.2.2

Additionally, the effect of the beam spot constrained alignment on the impact parameter  $d_0$  needs to be checked. The  $d_0$  distributions for both the March and June alignments are compared to the MC simulation using a perfect geometry in Figure 4.4. In the March alignment, there is a bias of 18  $\mu\text{m}$  in the mean of the distribution and the width is nearly twice that of the perfect geometry. After the second pass of the June alignment, the mean has shifted to 1  $\mu\text{m}$  and the distribution has narrowed considerably. From this, it appears that the constrained alignment successfully removed the  $d_0$  bias.

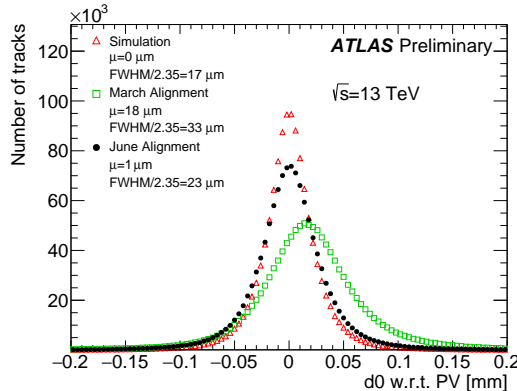


Figure 4.4: The  $d_0$  distributions with respect to the reconstructed primary vertex using the  $\sqrt{s} = 13$  TeV collision data sample reconstructed using the June (black) and March (green) alignments. The data is compared to a MC simulation using a perfect detector geometry (red). The distributions are normalized to the same number of entries.

#### 4.2.2.1 Residual distributions from collisions

As mentioned previously, the primary focus of the June alignment campaign was on the IBL and the Pixel detectors. The detectors are the closest to the beam line and have the finest resolutions of the

848 ID subdetectors. The residual distributions in local  $x$  and  $y$  of the IBL planar sensors<sup>7</sup> are shown  
 849 in Figure 4.5. These and subsequent figures in this section compare the June and March alignments  
 850 to the perfectly-aligned MC simulation. Noticeable improvement in the distribution widths can be  
 851 seen in both the local  $x$ - and  $y$ -directions, nearly matching the simulation in local  $x$ , which is the  
 852 most sensitive direction.

853 Due to the temperature-dependent bowing of the IBL, it is also interesting to look at the means of  
 854 the residual distributions for each ring of IBL sensors along the beam line, as shown in Figure 4.6. A  
 855 deformation is clearly visible in the March alignment in both measurement directions, and the shape  
 856 in the local  $x$ -direction is consistent with an average stave bowing due to the different operating  
 857 temperature of the IBL during the March alignment and the 13 TeV collisions. This feature was  
 858 nearly eliminated in both directions through the L3 alignment of the IBL sensors.

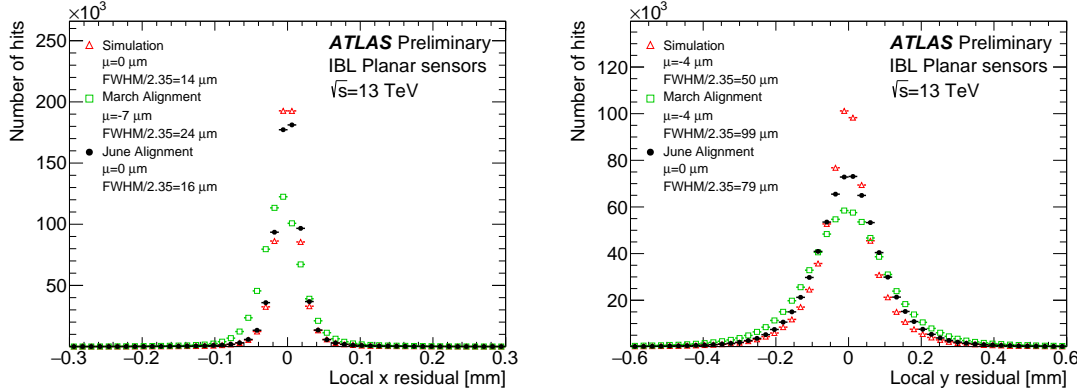


Figure 4.5: Local  $x$  (left) and local  $y$  (right) residual distributions of the IBL planar sensors using the  $\sqrt{s} = 13$  TeV collision data sample reconstructed using the June (black) and March (green) alignments. The data is compared to a MC simulation using a perfect detector geometry (red). The distributions are normalized to the same number of entries.

859 The local  $x$  and  $y$  residual distributions for the Pixel detector barrel and end-caps are shown in  
 860 Figure 4.7. Even though the IBL is not included in the plots of the barrel, some of the noticeable  
 861 improvement in the more sensitive local  $x$  direction is an effect of the improved IBL alignment.  
 862 Similarly, the relatively broad local  $y$  residual distribution in the barrel likely indicates that further  
 863 refinement of the IBL alignment was needed along that direction. Even so, the June alignment  
 864 outperforms the March alignment and rivals the simulation in most of the plots.

<sup>7</sup>The IBL contains 12 planar sensors in the center of a stave, with four 3D sensors on either end. Only the planar sensors are shown here due to low statistics in the 3D sensors as well as poor MC modeling of these sensors.

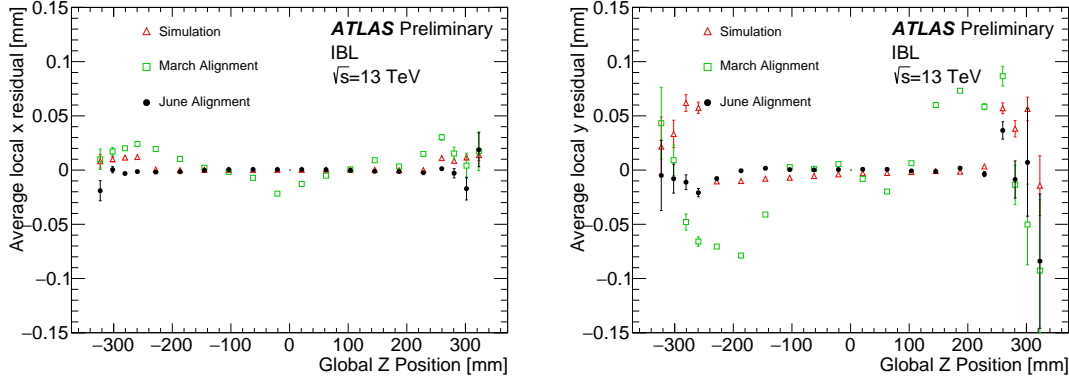


Figure 4.6: The mean of the local  $x$  (left) and local  $y$  (right) residual distributions as a function of the global  $z$  position of each IBL module using the  $\sqrt{s} = 13$  TeV collision data sample reconstructed using the June (black) and March (green) alignments. The data is compared to a MC simulation using a perfect detector geometry (red).

865     Similar distributions for the SCT and TRT barrel and end-caps are shown in Figures 4.8 and  
 866     4.9, respectively. Much like with the Pixel residuals, there is a reduction in the width of the TRT  
 867     residuals between the March and June alignments due to the alignment of the other subdetectors  
 868     improving the quality of the track fit. Even though neither subdetector was aligned at module-  
 869     level, the residuals indicate that the previous L3 alignment performed in Run 1 has not degraded  
 870     significantly during the upgrade and maintenance period.

#### 871     4.2.2.2 Track parameter resolution from cosmic rays

872     Cosmic ray data is very useful as an independent check on the alignment in the barrel of the  
 873     detector. While tracks from  $pp$  collisions originate within the detector and travel outwards, a cosmic  
 874     ray that passes through the center of the detector leaves a track in both halves of the detector.  
 875     If the cosmic ray is split in half, as in Figure 4.10, then it can be treated as two separate tracks  
 876     each with nearly identical track parameters (some differences arise due to energy loss as the particle  
 877     passes through the detector). The distribution of the difference in a given track parameter  $\Delta\tau$  is  
 878     approximately Gaussian with a variance  $\sigma^2(\Delta\tau)$ . Since both tracks come from the same particle,  
 879     each track individually has a variance equal to  $\sigma^2(\Delta\tau)/2$ . The resolution of the track parameter is  
 880     then given by the root mean square of the distribution divided by  $\sqrt{2}$ .

881     Cosmic rays whose split tracks each had transverse momentum  $p_T > 2$  GeV and at least one,  
 882     eight, and 25 hits in the barrels of the Pixel, SCT, and TRT detectors, respectively, were selected to

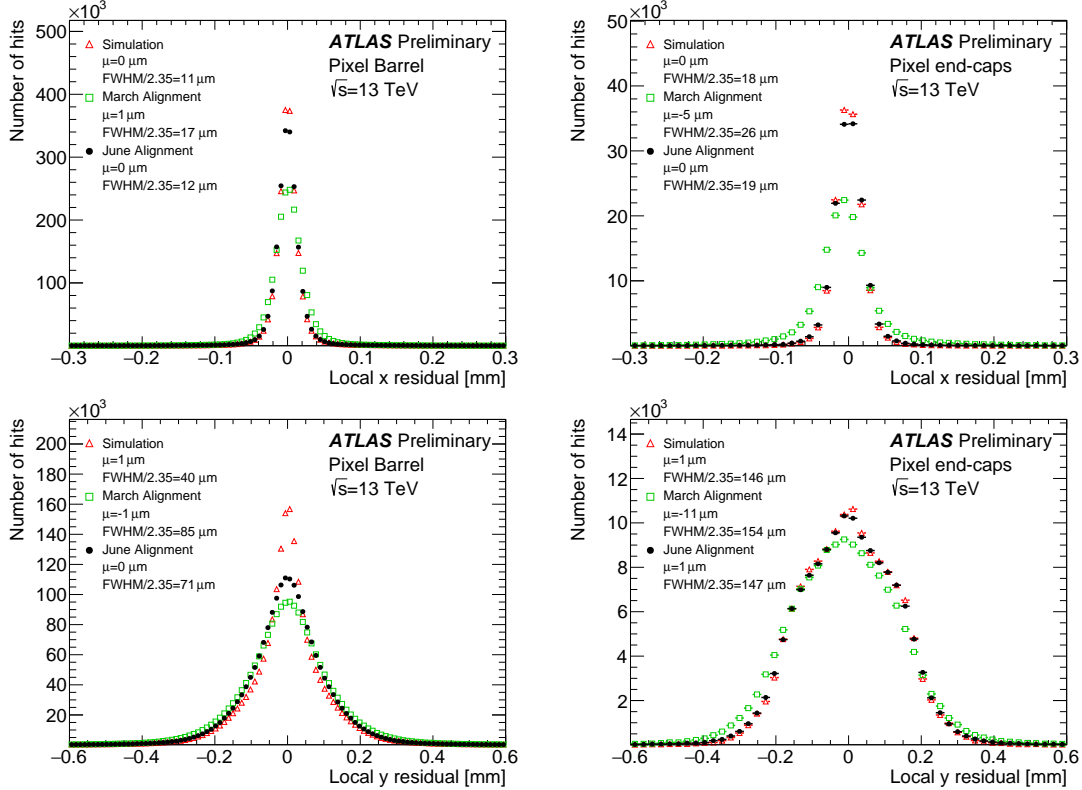


Figure 4.7: Local  $x$  (top) and local  $y$  (bottom) residual distributions for the Pixel barrel (excluding the IBL, left) and end-caps (right) using the  $\sqrt{s} = 13$  TeV collision data sample reconstructed using the June (black) and March (green) alignments. The data is compared to a MC simulation using a perfect detector geometry (red). The distributions are normalized to the same number of entries.

883 measure a collection of track parameters. Figure 4.11 shows the difference in the impact parameter  
 884  $\Delta d_0$  and the charge divided by the transverse momentum  $\Delta q/p_T$  of the selected split-track cosmic  
 885 rays for both the March and June alignments. Both distributions show a reduction in width in the  
 886 June alignment, corresponding to an improvement in the resolution of each track parameter. The  
 887  $\Delta d_0$  plot shows a significant improvement in the June alignment, further validating the removal of  
 888 the bias in the impact parameter.

### 889 4.2.3 Error scaling

890 The final step in preparing the new set of June alignment constants deals with the adjustment of  
 891 the hit errors, or *error scaling*. Knowledge of the exact position of a hit measurement on a track  
 892 is limited by the accuracy with which the sensors' positions are known. Let  $\sigma$  represent the hit

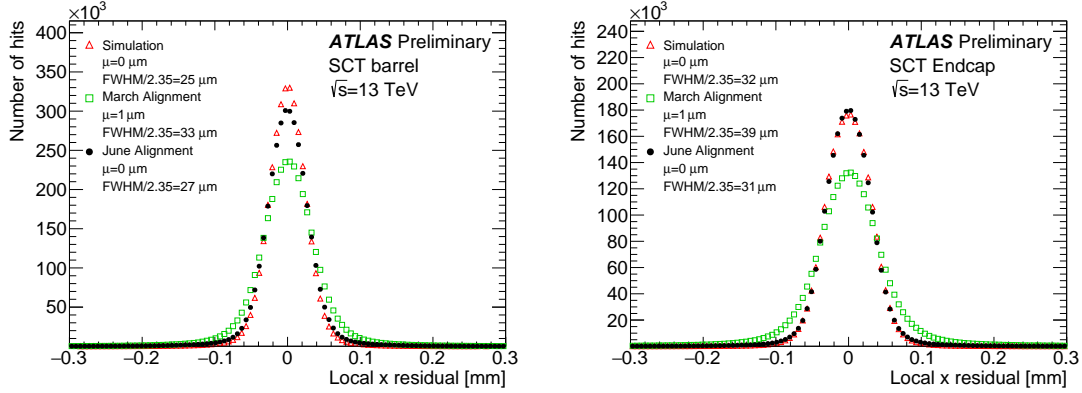


Figure 4.8: Local  $x$  residual distributions for the SCT barrel (left) and end-caps (right) using the  $\sqrt{s} = 13 \text{ TeV}$  collision data sample reconstructed using the June (black) and March (green) alignments. The data is compared to a MC simulation using a perfect detector geometry (red). The distributions are normalized to the same number of entries.

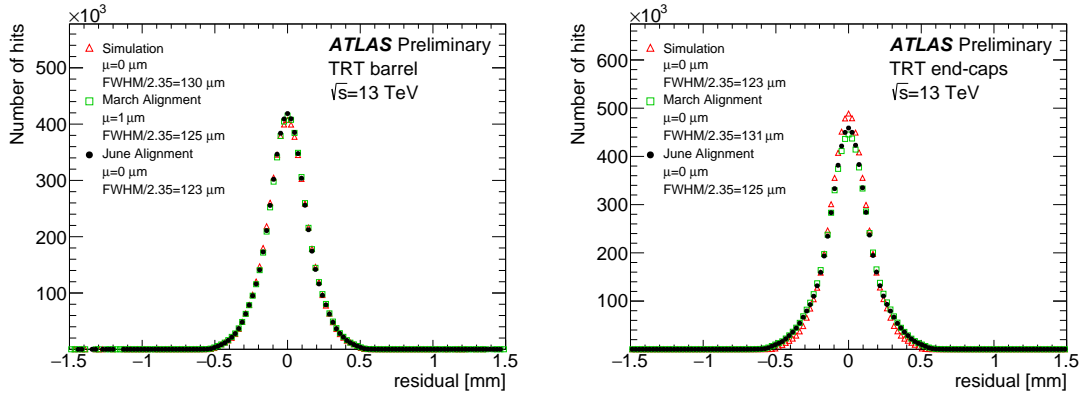


Figure 4.9: Residual distributions for the TRT barrel (left) and end-caps (right) using the  $\sqrt{s} = 13 \text{ TeV}$  collision data sample reconstructed using the June (black) and March (green) alignments. The data is compared to a MC simulation using a perfect detector geometry (red). The distributions are normalized to the same number of entries.

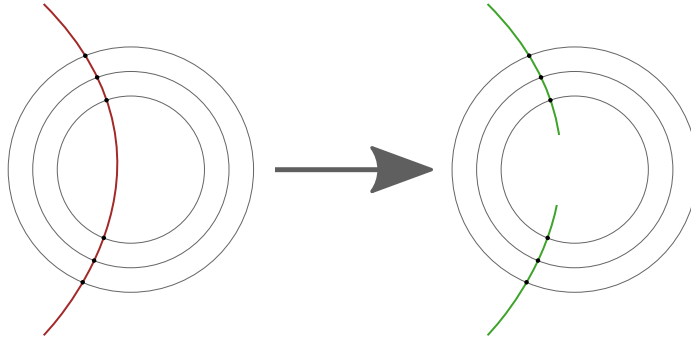


Figure 4.10: Representation of splitting a single cosmic ray track passing through the entire detector (left) into two separate tracks (right).

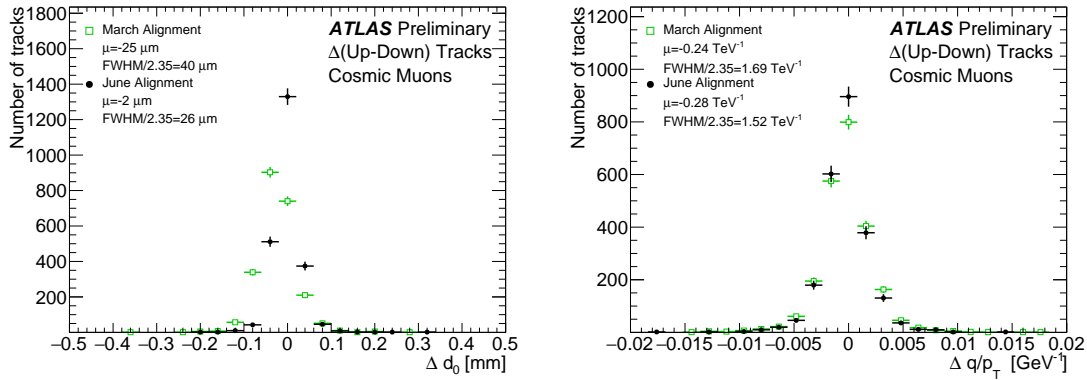


Figure 4.11: Distribution of the difference in the impact parameter  $\Delta d_0$  (left) and charge over transverse momentum  $\Delta q/p_T$  (right) between the two cosmic ray split tracks. The June (black) and March (green) alignments are compared. The distributions are normalized to the same number of entries.

893 uncertainty used in track fitting, and  $\sigma_0$  be the detector's intrinsic uncertainty. If  $\sigma = \sigma_0$ , the pull  
 894 of the track-hit residual distributions should form a Gaussian distribution centered at zero with a  
 895 standard deviation  $\sigma = 1$  [29]. In the case of residual misalignment, the pull distributions' standard  
 896 deviations will stray from unity. The hit uncertainty can be written as:

$$\sigma = a \cdot \sigma_0 \oplus b \quad (4.12)$$

897 where  $a$  is a scaling factor, and  $b$  is a constant term which can be interpreted as a measure of any  
 898 remaining misalignment of the detector elements. In this alignment campaign, the value of  $a$  is fixed  
 899 at  $a = 1$  and  $b$  is evaluated from the residual pull distributions for each subdetector in its sensitive  
 900 directions.

Once the value of  $b$  is determined, pull distributions derived from the new value of  $\sigma$  should have unit width. The error scaling values for each subdetector are listed in Table 4.3, and the pull distributions for the IBL after error scaling are shown in Figure 4.12.

Detector	Coordinate	$b(\mu\text{m})$
IBL	$x$	6.4
	$y$	43.6
Pixel	$x$	5.2
	$y$	28.6
SCT	$x$	7.5
	$y$	0
TRT	$x$	10.8
	$r\phi$	0
End-caps	$x$	8.6
	$r\phi$	0

Table 4.3: Estimated value of the error scaling term  $b$  for each subdetector component with the June alignment.

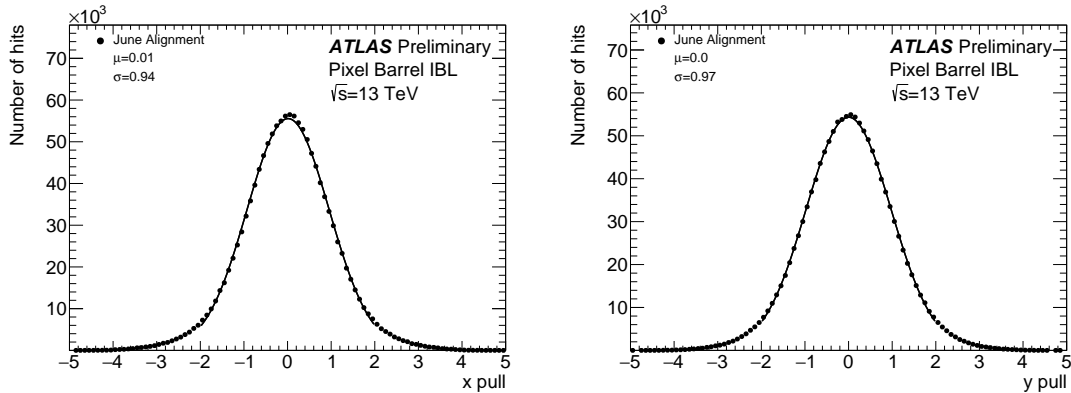


Figure 4.12: Pull distributions in local  $x$  (left) and  $y$  (right) for the IBL using the  $\sqrt{s} = 13$  TeV collision data sample after applying the error scaling.

### 4.3 Level 2 alignment of the TRT

During validation of the final end-of-year reprocessing of the 2015 data, a misalignment was found in the barrel of the TRT detector, as several modules (triangular clusters of straws) showed rotations in the local  $y$  coordinate. The then-best available constants included a full L3 alignment of the silicon detectors and a separate L2 alignment of the TRT. However, not all degrees of freedom were enabled when the TRT was aligned. To correct for these tilts, an additional four iterations of L2 alignment

910 TRT was performed on the TRT enabling all available degrees of freedom ( $T_x$ ,  $T_y$ ,  $R_x$ ,  $R_y$ , and  $R_z$   
 911 in the barrel, and  $T_x$ ,  $T_y$ , and  $R_z$  for the endcaps). Plots of the residual means from barrel  $\phi$  sectors  
 912 containing modules affected by the tilt misalignment are shown in Figure 4.13 before and after the  
 913 L2 alignment.

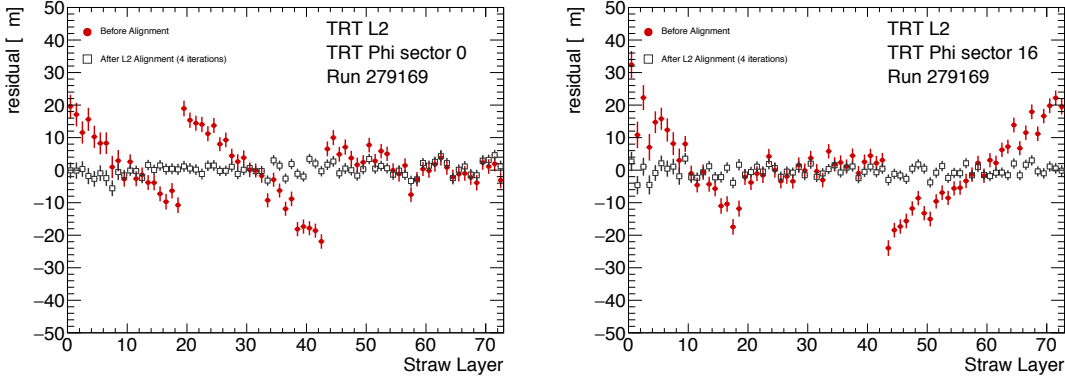


Figure 4.13: Residual means by straw layer in two TRT  $\phi$ -sectors affected by a tilt misalignment. The tilts in each of the three modules are clearly visible in the red points representing the reconstructed data prior to alignment. After four iterations of L2 alignment, the residual means in the gray points are flat.

914 Following the L2 alignment, some additional time was taken to determine if a full wire-by-wire  
 915 L3 alignment of the TRT was necessary. The TRT was last aligned at L3 during Run 1, but initial  
 916 alignment campaigns in Run 2 did not show signs of misalignment, as can be seen from the residual  
 917 distributions in Figure 4.9. In order to assess the alignment more carefully, two dimensional residual  
 918 maps in  $\phi$  and  $z$  were constructed for each layer in the TRT barrel and endcaps using the current  
 919 alignment. These maps were compared to a similar set using the L3 alignment from 2010, from which  
 920 it was determined that the straw-level alignment indeed hadn't degraded and a new L3 alignment  
 921 was not needed. The maps for the first layer of the TRT barrel are shown in Figure 4.14 for both  
 922 sets of alignment constants.

#### 923 4.4 Momentum bias from sagitta deformations

924 A variety of weak mode deformations can exist in the detector even after alignment. As mentioned  
 925 previously, these weak modes consist of misalignments which don't affect the  $\chi^2$  of the residuals  
 926 and thus are not handled by the basic alignment algorithm. In the presence of a weak mode, the  
 927 description of the detector geometry can still provide efficient and high quality track fits, but there

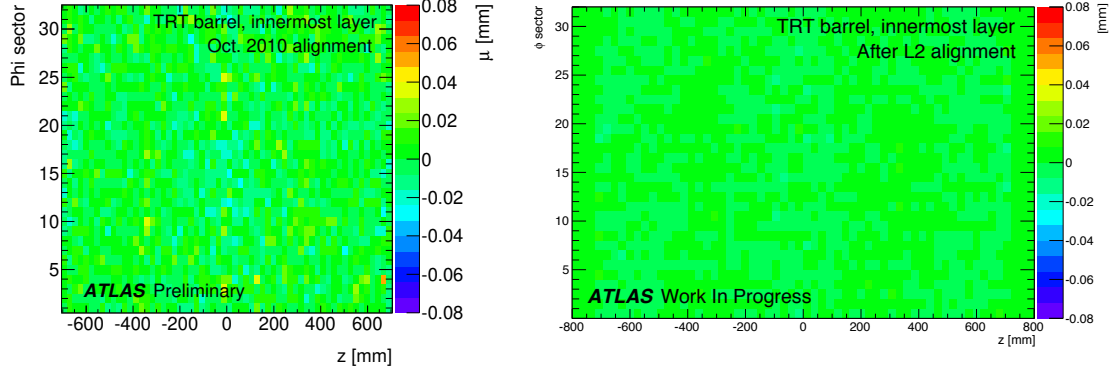


Figure 4.14: Two dimensional map of residuals in the first layer of the TRT barrel vs  $z$  and  $\phi$ . Each bin represents the mean of a Gaussian fit to the TRT residuals in that bin. The map on the left is after the L3 (wire-by-wire) alignment of the TRT performed in 2010, and the map on the right is after the L2 alignment at the end of 2015. The  $z$ -axis for both plots use the same scale. Left figure taken from [29].

may also be systematic biases in one or more track parameters. Several weak modes, their impacts on the reconstruction, and the steps taken to eliminate them are detailed in [32, 40]. This section focuses specifically on sagitta distortions that result in a bias in the reconstructed track momentum.

These *sagitta* distortions consist of detector movements orthogonal to the trajectory of the outgoing particle. The effect on the reconstructed track curvature is different for positively and negatively charged particles, resulting in a charge-antisymmetric bias. This effect is illustrated in the curl deformation shown in Figure 4.15.

In the plane transverse to ATLAS’s magnetic field, outgoing particle tracks form circular arcs. The sagitta is defined as the distance from the center of this arc to the center of its base, as shown in Figure 4.16, and it represents the “amount of bending” in the track. In the case where the sagitta  $s$  is considerably smaller than the detector radius  $R_0$ , which is a valid assumption when working with high momentum tracks, the transverse momentum of a particle of charge  $q$  can be written as [41]:

$$p_T \propto qB \frac{R_0^2}{8s} \quad (4.13)$$

where  $B$  is the strength of the detector’s magnetic field. If a sagitta bias is present, the track’s transverse momentum shifts by [40]:

$$q/p_T \rightarrow q/p_T + \delta_s \quad \text{or} \quad p_T \rightarrow p_T \cdot (1 + qp_T\delta_s)^{-1} \quad (4.14)$$

where  $\delta_s$  is a universal bias parameter that uniquely defines the deformation. Finally, since the reconstructed polar angle does not change under a sagitta deformation, the longitudinal component

944 of the momentum scales along with the transverse component, and an equivalent equation can be  
 945 written for the total momentum:

$$p \rightarrow p \cdot (1 + qp_T \delta_s)^{-1} \quad (4.15)$$

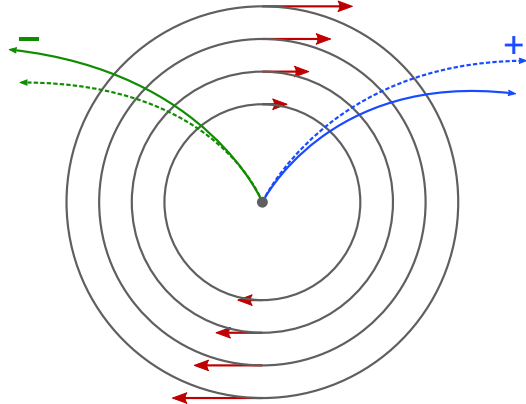


Figure 4.15: Representation of a curl distortion in the detector. The image shows a cutaway in the transverse plane. The deformation is represented by the red arrows, and the impact on the reconstructed positive (blue) and negative (green) tracks are shown. The dashed lines represent the true particle trajectories, and the solid lines represent the reconstructed trajectories.

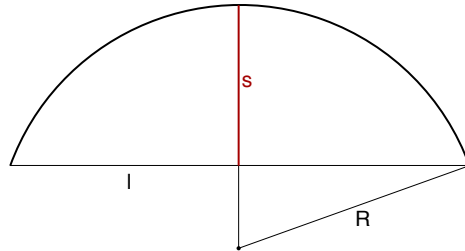


Figure 4.16: Geometric definition of the sagitta  $s$  in relation to the length of the chord  $l$  and the radius  $r$  of a circular arc.

#### 946 4.4.1 Sagitta bias monitoring with electron $E/p$

947 Since a sagitta bias results in changes in the momentum of particles' tracks as measured by the ID,  
 948 they can be identified using independent measurements from other systems in the detector. One  
 949 such method involves using the energy-momentum ratio of electrons ( $E/p$ ). Since the electron's  
 950 energy is measured in ATLAS's calorimeter systems, it is not sensitive to any sagitta bias that may  
 951 exist in the ID and the corresponding track momentum. Under the assumption that the calorimeter

952 response is independent of the charge of incoming particles, a charge-dependent momentum bias in  
 953 the ID will manifest as a difference in the  $E/p$  ratio for electrons and positrons.

954 In the presence of a sagitta bias, the momentum will change according to Equation 4.15 and the  
 955 average measured  $\langle E/p \rangle$  can be written as:

$$\langle E/p \rangle^\pm \rightarrow \langle E/p \rangle^\pm \pm \langle E_T \rangle \delta_s \quad (4.16)$$

956 where the approximation  $p_T \approx E_T$  is used. Assuming that  $\langle E/p \rangle^+ = \langle E/p \rangle^-$  in the absense of a  
 957 bias, the sagitta bias parameter can be written as:

$$\delta_s = \frac{\langle E/p \rangle^+ - \langle E/p \rangle^-}{2\langle E_T \rangle} \quad (4.17)$$

958 If the kinematic selections for electrons and positrons are identical, the energy scale of the calorimeter  
 959 will not factor into the  $\langle E/p \rangle$  difference; however, it will affect  $\langle E_T \rangle$  which would scale the measured  
 960  $\delta_s$ . This is expected to be a small effect, as the energy scale for electrons has been measured at  
 961  $\sqrt{s} = 13$  TeV with uncertainties on the per-mil level across the entire detector [42].

#### 962 4.4.1.1 Measuring $\langle E/p \rangle$

963 The  $E/p$  ratio is measured using electrons and positrons from  $Z \rightarrow e^\pm e^\mp$  events in order to obtain  
 964 a high purity sample of electron candidates. They are required to pass a basic selection criteria to  
 965 ensure they are well measured by both the ID and the calorimeters:

- 966 •  $E_T > 25$  GeV
- 967 •  $|\eta| < 2.47$ , excluding the calorimeter's barrel-to-endcap transition region in  $1.37 < |\eta| < 1.52$
- 968 • Pass MediumLH identification working point detailed in Section 3.2.4.3
- 969 • Pass a selection of quality cuts, including a requirement that the electron be identified using  
   970 cluster information in the calorimeter
- 971 • The associated track must have at least one hit in the IBL, three in the Pixel detector, and  
   972 five in the SCT detector.

973 Events with exactly two opposite-charge electrons passing this selection with a dielectron invariant  
 974 mass within 30 GeV of the  $Z$  boson mass are then used for the  $E/p$  calculation.

975 Since the size of the sagitta bias  $\delta_s$  is not expected to be constant across the entire detector,  
 976 a two-dimensional rectangular grid binned in detector  $\eta$  and  $\phi$  is constructed. From the selected

events, separate distributions of  $E/p$  are made for electrons and positrons lying in each bin. Each distribution is fit with Crystal Ball function<sup>8</sup>, and the peak of the distribution is taken as the value of  $\langle E/p \rangle$ . If there is no bias on the track momentum in the bin, the peaks for electrons and positrons should match. Example  $E/p$  distributions including the Crystal Ball fits are shown in Figure 4.17.

It is important to emphasize that deviations from one in the *ratio* of  $\langle E/p \rangle$  for electrons and positrons indicates that a momentum bias may be present. The value of  $\langle E/p \rangle$  itself is not expected to equal one exactly, as the track momentum on average tends to be slightly lower than the energy measurement in the calorimeter. This is due to the fact that if the electron were to radiate a photon, its momentum would change slightly, while it is likely that both the electron and the emitted photon would leave energy deposits near each other in the calorimeter and be reconstructed into the same object.

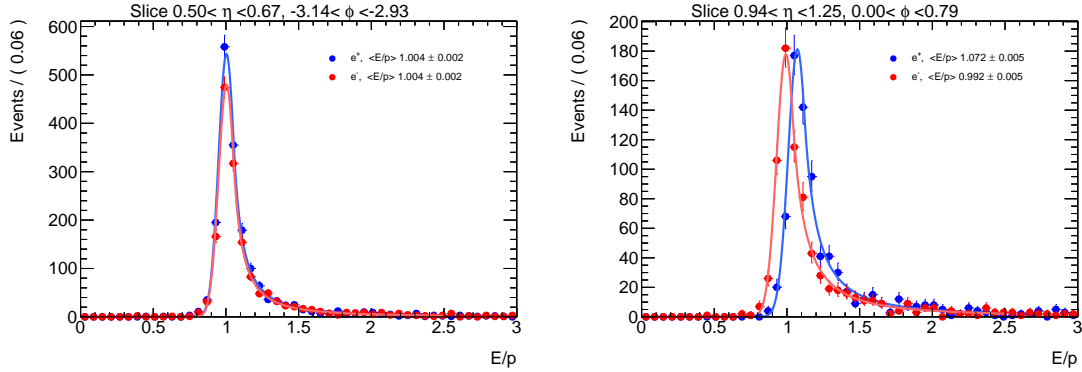


Figure 4.17:  $E/p$  distributions of electrons and positrons in two different  $\eta\text{-}\phi$  bins of the detector. The left hand plot is taken from a region with no momentum bias where  $\langle E/p \rangle^+ = \langle E/p \rangle^-$ , while the right hand plot shows an 8% disagreement in  $\langle E/p \rangle$  between electrons and positrons.

Once the  $\langle E/p \rangle^\pm$  distributions in each  $\eta\text{-}\phi$  bin have been extracted from the fits, a two dimensional map of  $\delta_s$  can be constructed using Equation 4.17. The map gives an overview of sagitta biases that may be present in the detector, and can be used by the alignment algorithm to reduce the bias in the next iteration. In this case, the tracks fed to the alignment have their momenta corrected according to [40]:

$$q/p_{\text{corr}} = q/p_{\text{reco}}(1 - qp_T\delta_s) \quad (4.18)$$

where  $p_{\text{reco}}$  is the reconstructed momentum of the track. The corrected momentum is then constrained in the alignment.

<sup>8</sup>The Crystal Ball function is a probability density function consisting of a Gaussian core and a power-law tail.

995    **4.4.1.2 Results in 13 TeV data**

996    The  $E/p$  method has been used to monitor sagitta biases in the detector several times over the  
997    course of Run 2. During this time, it has primarily served as an independent cross-check to a  
998    second method using  $Z \rightarrow \mu^\pm \mu^\mp$  events [40]. The  $Z \rightarrow \mu^\pm \mu^\mp$  method identifies individual track  
999    momentum biases through shifts in the reconstructed  $Z$  mass, which leaves it relatively insensitive  
1000   to global sagitta biases. For this reason, the sagitta bias maps produced using this technique are  
1001   normalized to those from the  $E/p$  method before being used to constrain the alignment.

1002    The results of two implementations of the  $E/p$  method are presented here.

1003    1. The first follows the end-of-year reprocessing of the entire ATLAS 2016 data set at  $\sqrt{s} =$   
1004       13 TeV. Two sets of alignment constants are compared: the *prompt* alignment, which was  
1005       derived shortly after each run was recorded, and the *reprocessed* alignment. The maps of the  
1006       sagitta bias comparing the two alignments calculated using the  $E/p$  method are shown in  
1007       Figure 4.18, and the comparison of the  $\eta$  projection of each map is shown in Figure 4.19.

1008    2. The second uses the 2017 data after reprocessing, and compares the effects of multiple it-  
1009       erations of the method. In each iteration, the momenta of the electrons and positrons are  
1010       corrected based on Equation 4.15 using the value of  $\delta_s$  computed in the previous iteration,  
1011       and a new sagitta bias map is calculated. If the method is indeed characterizing the sagitta  
1012       biases correctly, the corrections should converge quickly. The initial sagitta bias map is com-  
1013       pared to the map after two such iterations in Figure 4.20, and the sagitta bias projected along  
1014        $\eta$  for each iteration is shown in Figure 4.21. Indeed, after just two iterations,  $\delta_s$  is consistent  
1015       with zero in nearly all bins.

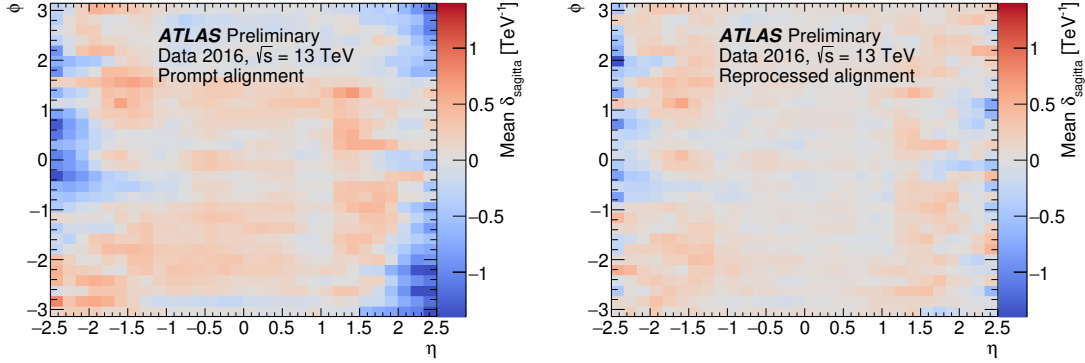


Figure 4.18: Sagitta bias in the  $\sqrt{s} = 13$  TeV data collected by ATLAS in 2016 as a function of  $\eta$  and  $\phi$  for the prompt (left) and reprocessed (right) alignments using the  $E/p$  method.

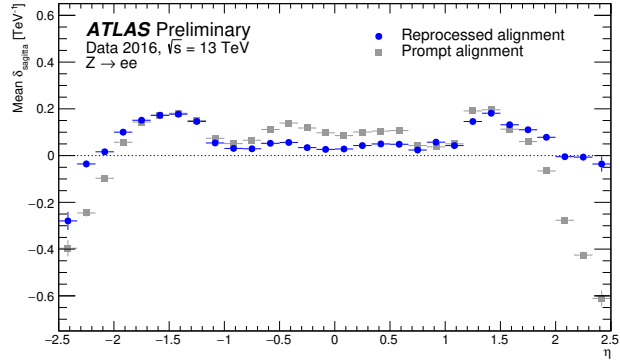


Figure 4.19: Sagitta bias in the  $\sqrt{s} = 13$  TeV data collected by ATLAS in 2016 projected along  $\eta$  for the prompt (gray) and reprocessed (blue) alignments using the  $E/p$  method.

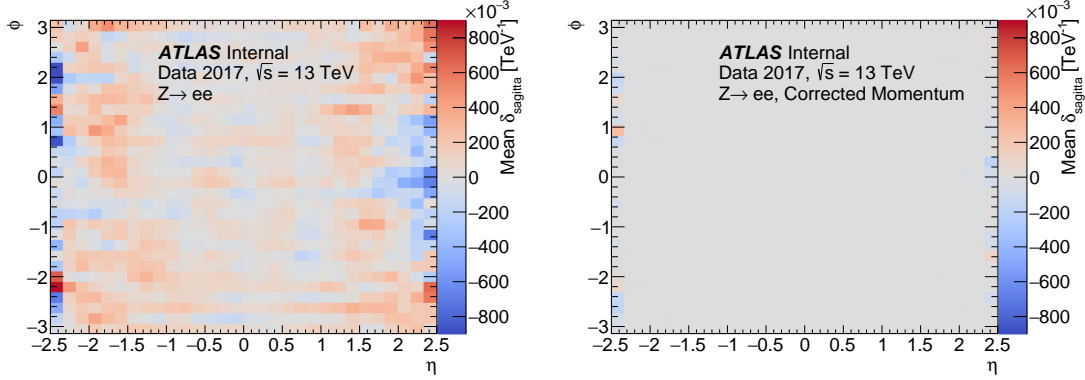


Figure 4.20: Sagitta bias in the  $\sqrt{s} = 13$  TeV data collected by ATLAS in 2017 as a function of  $\eta$  and  $\phi$  in reconstructed electrons (left) and after two iterations of momentum corrections (right) from the  $E/p$  method.

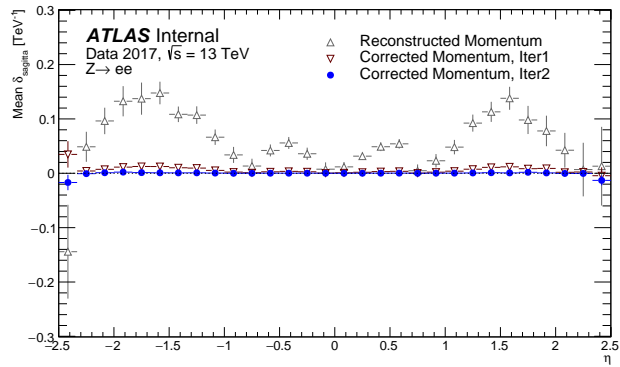


Figure 4.21: Sagitta bias in the  $\sqrt{s} = 13$  TeV data collected by ATLAS in 2017 projected along  $\eta$  in reconstructed electrons (gray) and after one (red) and two (blue) iterations of momentum corrections from the  $E/p$  method.

1016

## CHAPTER 5

1017

1018

# Measurement of same-sign $WW$ production at $\sqrt{s} = 13$ TeV with ATLAS

1019 Production of same-sign  $W$  boson pairs is a particularly interesting SM process. When produced  
1020 via vector boson scattering (VBS),  $W^\pm W^\pm jj$  is particularly sensitive to the electroweak symmetry  
1021 breaking (EWSB) mechanism as well as potential “beyond the Standard Model” (BSM) physics.  
1022  $W^\pm W^\pm jj$  events can be produced via electroweak-mediated (EWK) diagrams, of which VBS is a  
1023 subset, or QCD-mediated diagrams. The biggest advantage of same-sign  $W^\pm W^\pm jj$  lies in its ratio  
1024 of electroweak (EWK) to QCD production cross sections. Despite the opposite-sign  $W^\pm W^\mp$  having  
1025 a considerably larger total cross section, its EWK-mediated diagrams are considerably smaller than  
1026 its QCD-mediated diagrams, while for same-sign  $W^\pm W^\pm$  the ratio is approximately one to one.  
1027 This makes  $W^\pm W^\pm jj$  one of the best channels for studying VBS at the LHC.

1028 The first evidence of electroweak (EWK)  $W^\pm W^\pm jj$  production was seen by the ATLAS and  
1029 CMS experiments at  $\sqrt{s} = 8$  TeV with excesses of  $3.6\sigma$  [20] and  $2.0\sigma$  [43] over backgrounds, respec-  
1030 tively. More recently, ATLAS and CMS have both observed the EWK process at  $\sqrt{s} = 13$  TeV  
1031 with significances of  $6.9\sigma$  [44] and  $5.5\sigma$  [45], respectively. The analysis presented in this chap-  
1032 ter is based off of the ATLAS  $\sqrt{s} = 13$  TeV observation and cross section measurement of EWK  
1033  $W^\pm W^\pm jj$  production [44, 46].

### 1034 5.0.2 Theoretical overview of vector boson scattering

1035 VBS processes are very important to understand due to their sensitivity to the EWSB mechanism.  
1036 The scattering amplitude of longitudinally polarized vector bosons grows with center-of-mass energy  
1037 and ultimately violates unitarity above  $\sqrt{s} = 1$  TeV in the absence of a light SM Higgs boson [47, 48].

1038 However, once the Higgs is introduced, the divergences cancel and the cross section no longer grows  
 1039 unbounded, as can be seen in Figure 5.1, which consists of plots from [49].

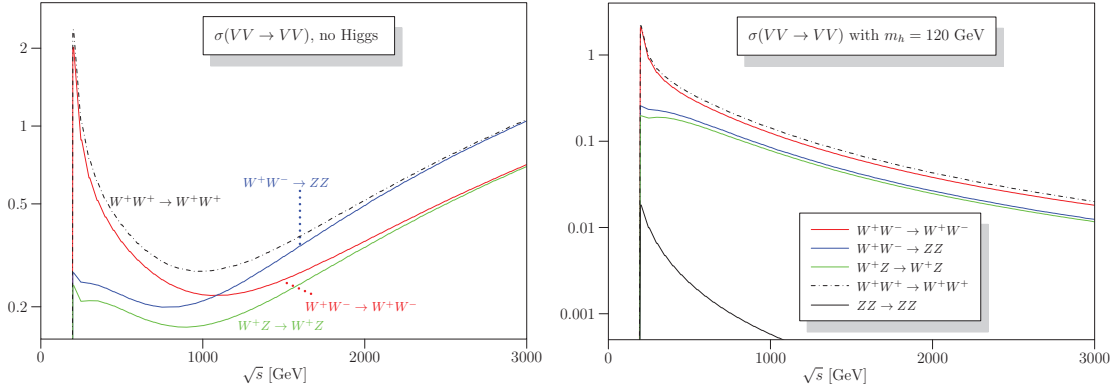


Figure 5.1: Cross sections in nanobarns for five different scattering processes of longitudinally polarized vector bosons as a function of center of mass energy  $\sqrt{s}$ . Without a SM Higgs boson (left), the cross sections grow unbounded with  $\sqrt{s}$ ; however with a 120 GeV Higgs boson (right), the cross sections no longer diverge. Plots taken from [49].

1040 With the discovery of the Higgs boson in 2012 [14, 15], the EWSB mechanism can now be directly  
 1041 studied. Due to the exchange of a Higgs in the  $s$ - and  $t$ -channel VBS diagrams ( $W^\pm W^\pm jj$  itself only  
 1042 contains the  $t$ -channel diagram), VBS processes are directly sensitive to properties of the Higgs. For  
 1043 example, the high-mass tail in the  $VV$  scattering system allows an approximation of the effective  
 1044 coupling strength of the Higgs to vector bosons that is independent of any assumptions on the Higgs  
 1045 width [50]. Additionally, the center of mass energy dependence of the  $VV$  scattering can reveal  
 1046 whether the Higgs boson unitarizes the longitudinal scattering amplitude fully or only partially [51].

1047 VBS events are characterized by two quarks from the colliding protons each radiating a massive  
 1048 vector boson which then scatter and decay in the detector. The incoming quarks carry a large  
 1049 amount of momentum and only deflect a small amount upon radiating the vector boson; as a result,  
 1050 they often travel very close to the beam line. Ignoring the decay products of the bosons, these VBS  
 1051 events result in a final state of two vector bosons ( $V$ ) and two jets ( $j$ ) at high pseudorapidities  
 1052 (called *forward jets*) from the outgoing quarks. The shorthand  $VVjj$  is used to represent this final  
 1053 state.

1054  $VVjj$  events can be produced via two different physical processes. The first involves purely  
 1055 electroweak interactions in the tree-level diagrams, with  $\mathcal{O}(\alpha_{EWK}) = 6$  and will be referred to as  
 1056 *EWK production*. This can be further broken down into VBS and non-VBS production. In the  
 1057 VBS EWK production, the scattering occurs via triple or quartic gauge couplings, as well as the

1058  $s$ - or  $t$ -channel exchange of a Higgs boson. The non-VBS EWK production contains the same final  
 1059 state of two vector bosons and two outgoing quarks, but the bosons do not scatter. Due to gauge  
 1060 invariance, it is not possible to separate the VBS from the non-VBS productions [52]; therefore,  
 1061 both are included in the signal generation and are indistinguishable from one another. The second  
 1062 process involves a mix of the EWK and strong interactions, of order  $\mathcal{O}(\alpha_s) = 2 \otimes \mathcal{O}(\alpha_{\text{EWK}}) = 4$  and  
 1063 will be referred to as *QCD production*. The tree-level Feynman diagrams for VBS EWK, non-VBS  
 1064 EWK, and QCD  $VVjj$  production are found in Figures 5.2, 5.3, and 5.4, respectively.

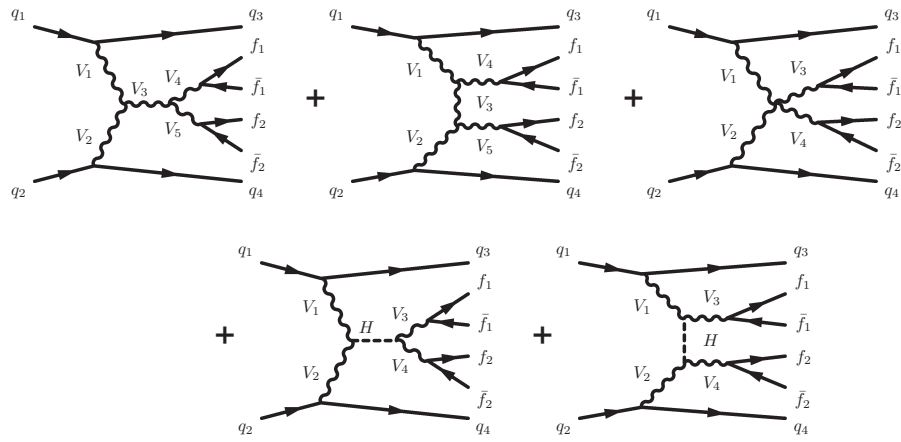


Figure 5.2: Tree-level Feynman diagrams for VBS EWK  $VVjj$  production including triple gauge couplings involving  $W$  and/or  $Z$  bosons (top left and top middle), quartic gauge coupling (top right), or the exchange of a Higgs boson ( $s$ -channel bottom left and  $t$ -channel bottom right). The labels are quarks ( $q$ ), fermions ( $f$ ), and gauge bosons ( $V = W, Z$ ).

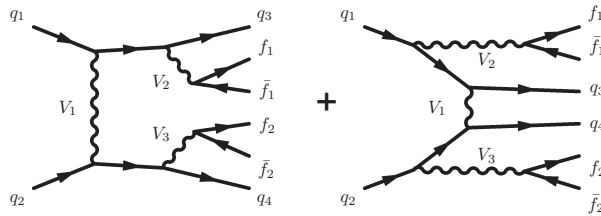


Figure 5.3: Tree-level Feynman diagrams for non-VBS EWK  $VVjj$  production. The labels are quarks ( $q$ ), fermions ( $f$ ), and gauge bosons ( $V = W, Z$ ).

### 1065 5.0.3 Same-sign $W^\pm W^\pm$ scattering

1066 Same-sign  $W^\pm W^\pm jj$  scattering is considered to be one of the best channels for studying VBS at the  
 1067 LHC [50]. This is due primarily to the ratio of the EWK to the QCD production, which matters

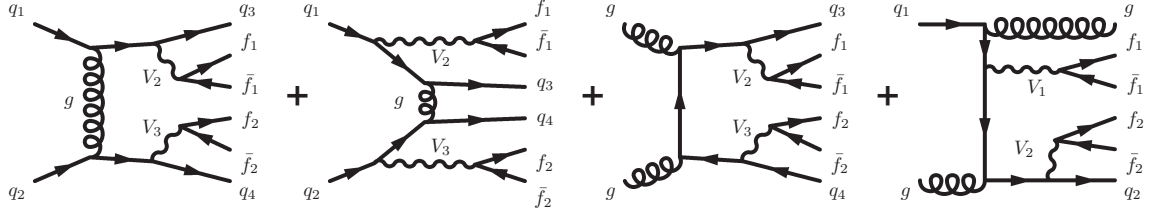


Figure 5.4: Tree-level Feynman diagrams for QCD  $VVjj$  production. The labels are quarks ( $q$ ), fermions ( $f$ ), and gauge bosons ( $V = W, Z$ ).

1068 a great deal due to the VBS events being a subset of the total EWK production. In an analysis  
 1069 the EWK production would be considered the signal and the QCD production a background, so a  
 1070 favorable ratio of the two helps greatly when comparing the size of the signal to the backgrounds.  
 1071 A study at  $\sqrt{s} = 8$  TeV [53] was done using the **SHERPA** Monte Carlo (MC) generator to calculate  
 1072 EWK and QCD production cross sections at leading order for a variety of  $VVjj$  processes decaying  
 1073 to leptons and can be found in Table 5.1. Despite its lower cross section compared to other  $VVjj$   
 1074 processes, the EWK to QCD ratio for  $W^\pm W^\pm jj$  is approximately one-to-one, whereas for opposite-  
 1075 sign  $W^\pm W^\mp jj$  the ratio is closer to 3%.

Process	Final state	$\sigma_{\text{EWK}}$	$\sigma_{\text{QCD}}$
$W^\pm W^\pm$	$l^\pm l^\pm \nu\nu jj$	19.5 fb	18.8 fb
$W^\pm W^\mp$	$l^\pm l^\mp \nu\nu jj$	91.3 fb	3030 fb
$W^\pm Z$	$l^\pm l^\pm l^\mp \nu jj$	30.2 fb	687 fb
$ZZ$	$l^+ l^- \nu\nu jj$	2.4 fb	162 fb
$ZZ$	$l^+ l^- l^+ l^- jj$	1.5 fb	106 fb

Table 5.1: Predicted cross sections for EQK and QCD production of diboson processes relevant to VBS at  $\sqrt{s} = 8$  TeV using the **SHERPA** MC generator. Loose generator level cuts are applied on lepton  $p_T > 5$  GeV, dilepton invariant mass  $m_{ll} > 4$  GeV, and at least two jets with  $m_{jj} > 10$  GeV. Numbers taken from [53].

1076 This analysis studies  $W^\pm W^\pm jj$  scattering where both  $W$  bosons decay leptonically to  $e\nu$  or  $\mu\nu$ <sup>9</sup>.  
 1077 The  $W^\pm W^\pm jj$  VBS final state consists of two leptons with the same electric charge, two neutrinos,  
 1078 and two high energy forward jets with a large invariant mass. Tree-level Feynman diagrams of VBS  
 1079  $W^\pm W^\pm jj$  production can be found in Figure 5.5 and a visual representation of the VBS topology  
 1080 can be found in Figure 5.6. The two forward jets also serve as a powerful tool to suppress the  
 1081 QCD production mode. In EWK events, the two jets tend to have much higher separation and a  
 1082 larger combined invariant mass than the two leading jets in a QCD event. The two plots shown in

<sup>9</sup>Throughout the rest of this chapter,  $l$  denotes either electrons ( $e$ ) or muons ( $\mu$ ) unless stated otherwise. Additionally,  $e$ ,  $\mu$ , and  $\nu$  (neutrino) with no charge or anti-particle designation refer interchangeably to either the particle or anti-particle.

1083 Figure 5.7 highlight the differences in these dijet quantities between the two production modes. An  
 1084 ATLAS event display of a real  $W^\pm W^\pm jj$  candidate event is shown in Figure 5.8.

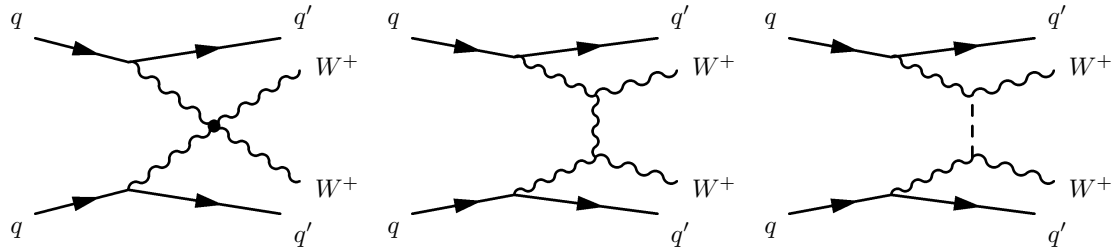


Figure 5.5: Feynman diagrams for VBS EWK production of  $W^\pm W^\pm jj$  events. The leftmost diagram contains a quartic gauge coupling vertex, and the rightmost diagram contains an exchange of a Higgs boson. **TODO: Make diagrams consistent with others**

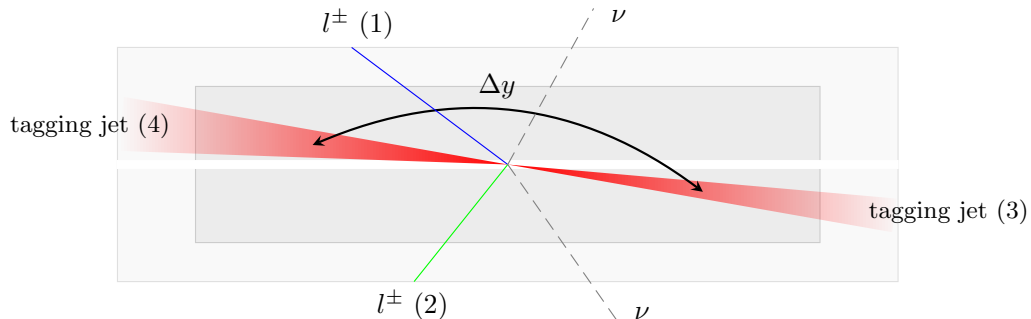


Figure 5.6:  $W^\pm W^\pm jj$  VBS event topology containing two leptons (1 and 2) with the same electric charge, two neutrinos, and two forward tagging jets (3 and 4) with large rapidity separation  $\Delta y$ .

#### 1085 5.0.4 Overview of backgrounds

1086 In addition to QCD production of  $W^\pm W^\pm jj$  events, there are several other processes that can end  
 1087 up with a final state of two same-sign leptons, two neutrinos, and two jets. However, due to the  $\pm 2$   
 1088 final state charge, there is a considerable reduction in SM backgrounds (such as  $Z$  boson events)  
 1089 when compared to an analysis like opposite-sign  $W^\pm W^\mp jj$ .

1090 One of the largest sources of background involves processes with prompt leptons<sup>10</sup>. These are  
 1091 events that contain two leptons with the same electric charge and one or more additional leptons

<sup>10</sup>Prompt leptons are those that are produced in the primary collision and are a direct decay product of the process of interest. Non-prompt leptons originate from some secondary process, such as a  $b$ -hadron decay, or are jets that get mis-reconstructed as a lepton.

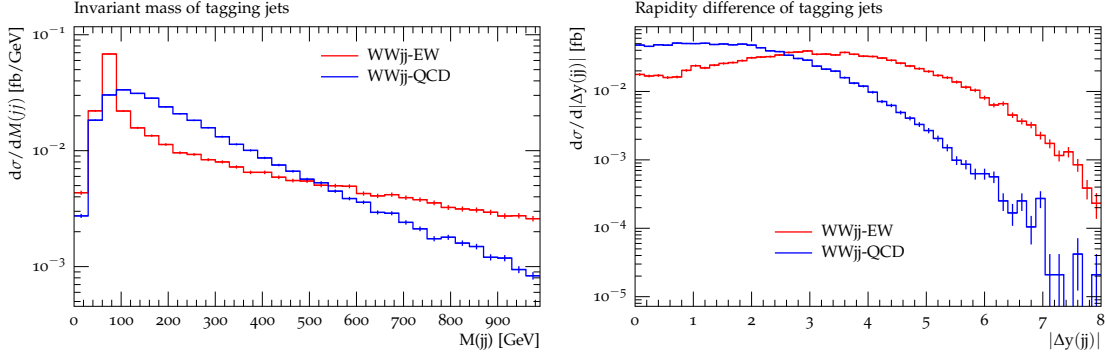


Figure 5.7: Generator level comparisons at  $\sqrt{s} = 8$  TeV of dijet invariant mass ( $m_{jj}$ , left) and dijet rapidity ( $\Delta y_{jj}$ , right) in EWK (red) and QCD (blue)  $W^\pm W^\pm jj$  events. Both data sets have been normalized to the same area. Plots taken from [53].

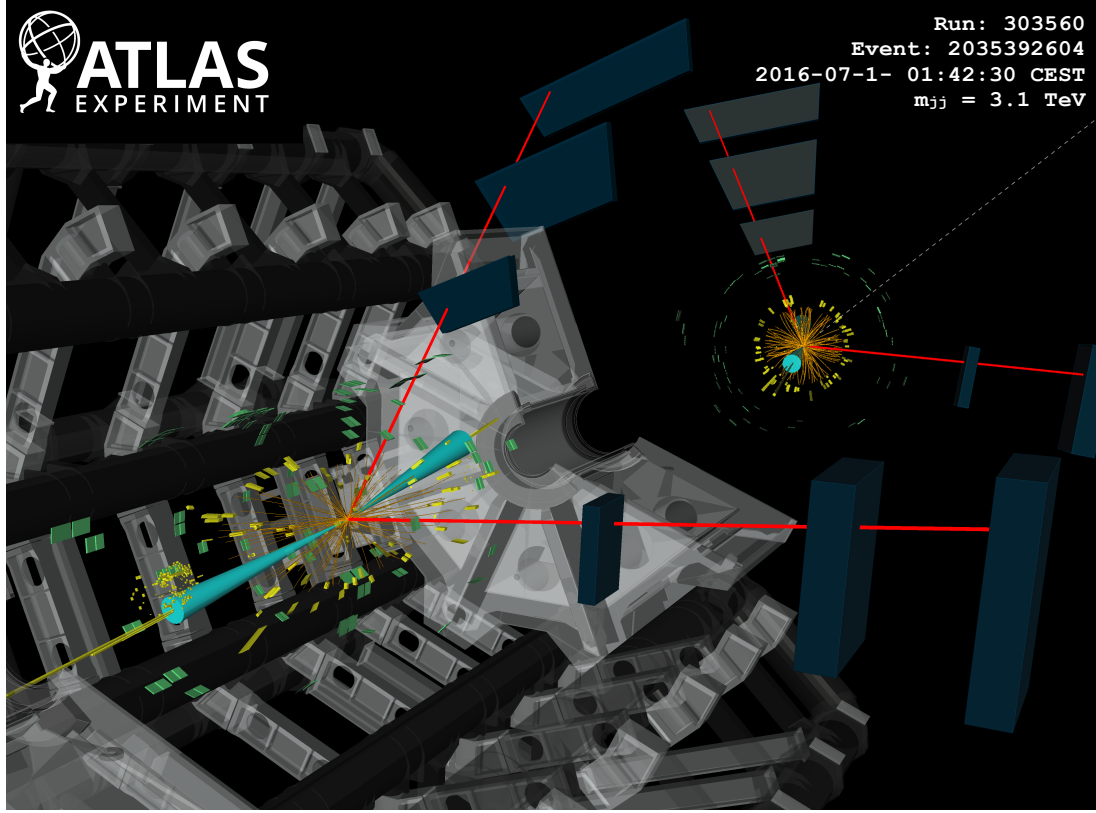


Figure 5.8: ATLAS event display of a  $pp \rightarrow W^\pm W^\pm \rightarrow \mu^\pm \nu_\mu \mu^\pm \nu_\mu jj$  event. The muons are represented by the red lines travelling from the ID through the MS, and the forward jets are represented by the blue cones with yellow energy deposits in the calorimeters. The direction of the  $E_T^{\text{miss}}$  in the transverse plane is indicated by the gray dashed line in the inset image. Event display taken from [44].

that are “lost”, either by failing the selection criteria or falling outside of the detector’s acceptance. The number of processes that can contribute is limited by the requirement of same-sign leptons, and as a result this background is dominated by processes involving two or more vector bosons, with the largest contribution coming from  $WZ$  events and smaller contributions from  $ZZ$  and  $t\bar{t}V$  events. Triboson events where one boson decays hadronically also contribute to this background; however, the jets are generally softer and more central than in a typical VBS event, and the cuts applied on the forward jets suppress these contributions.

The other dominant background comes from non-prompt, or “fake”, leptons. Here one or more leptons originate from the decay of another particle unrelated to the signal process, such as a heavy-flavor decay or photon conversion, or come from a jet that is misidentified as a lepton. This background is mostly made up of events from  $t\bar{t}$  and  $W+\text{jets}$  processes, with a much smaller contribution from  $V\gamma$  events. **TODO: check whether  $V\gamma$  really qualifies as non-prompt, we lump  $Z\gamma$  in with the charge flip background in the paper...**

Finally, opposite-sign lepton pairs can enter the signal region if one of the leptons is reconstructed with the wrong charge (called *charge misidentification*<sup>11</sup>). In practice, this only affects events with electrons, as the charge misidentification rate for muons is negligible [54]. This is a major background in events with two electrons, but is a much smaller contribution for events with one electron and one muon.

## 5.1 Data and Monte Carlo samples

This analysis uses  $36.1 \text{ fb}^{-1}$  of  $\sqrt{s} = 13$  TeV proton-proton collision data recorded by ATLAS during 2015 and 2016. The uncertainty in the combined integrated luminosity is 2.1%. It is derived following a methodology similar to that detailed in [55] and using the LUCID-2 detector for the baseline luminosity measurements [56] from calibration of the luminosity scale using  $x$ - $y$  beam-separation scans.

### 5.1.1 Monte Carlo samples

A number of Monte Carlo (MC) simulations are employed to model signal and background processes. In order to model the real collision data as closely as possible, each MC has been run through a full simulation of the ATLAS detector [57] in GEANT4 [58], and events have been reconstructed

---

<sup>11</sup>Charge misidentification is also referred to interchangeably as *charge mis-ID* and *charge flip*.

1120 using the same algorithms as the data. The simulation reproduces as closely as possible the momentum  
 1121 resolutions and calorimeter responses of the detector, and also includes the effects of pileup by  
 1122 including soft QCD interactions using PYTHIA v8.1 [59]. The MC samples used in this analysis are  
 1123 detailed in this section and summarized in Table 5.2.

1124 The  $W^\pm W^\pm jj$  samples are modeled using SHERPA v2.2.2 [60, 61, 62] with the NNPDF3.0 PDF  
 1125 set [63]. The EWK signal samples are generated by fixing the electroweak coupling constant to  
 1126  $\mathcal{O}(\alpha_W) = 6$ , and a QCD background sample was also generated with  $\mathcal{O}(\alpha_W) = 4$ . SHERPA includes  
 1127 up to one parton at next-to-leading order (NLO) and up to three at leading order (LO) in the  
 1128 strong coupling constant  $\alpha_s$ . A second  $W^\pm W^\pm jj$  EWK sample is generated using POWHEG-BOX  
 1129 v2 [64] with the NNPDF3.0 PDF set and at NLO accuracy. This sample is only used for systematic  
 1130 studies, as POWHEG-BOX does not include resonant triboson contributions in its matrix element, which  
 1131 are non-negligible at NLO [65].

1132 Diboson processes ( $VV$  where  $V = W, Z$ ) are simulated with SHERPA v2.2.2 for mixed hadronic  
 1133 and leptonic decays and SHERPA v2.2.1 for fully leptonic decays of the bosons. Similarly, triboson  
 1134 ( $VVV$ ) and  $V\gamma$  processes are simulated using SHERPA v2.1.1 with up to one parton at NLO and up  
 1135 to three at LO.  $W+jets$  processes are simulated with SHERPA2.2.1 with up to two partons at NLO  
 1136 and four at LO. All the above SHERPA samples use the NNPDF3.0 PDF set and SHERPA's own parton  
 1137 showering. The  $Z+jets$  events are generated with Madgraph5\_aMC@NLO [66] at LO and interfaced  
 1138 with PYTHIA v8.1 for parton showering.

1139  $t\bar{t}$  events are generated using POWHEG-BOX v2 with the CT10 PDF set [67].  $t\bar{t}V$  samples are  
 1140 generated at NLO with Madgraph5\_aMC@NLO and the NNPDF3.0 PDF set interfaced with PYTHIA v8  
 1141 for parton showering. Finally, single top events are generated with POWHEG-BOX v1 and the CT10f4  
 1142 PDF set interfaced with PYTHIA v6 [68] for parton showering.

## 1143 5.2 Object and event selection

1144 This section details the selection criteria for objects used in the analysis as well as the selection for  
 1145 signal events.

### 1146 5.2.1 Object selection

1147 Muons, electrons, and jets all must pass strict selection requirements to ensure that only high quality,  
 1148 well measured objects are used. For leptons, a baseline selection is defined (called the *preselection*),  
 1149 which all leptons must pass in order to be considered for the analysis. This preselection is an

Process	Generator	Comments
$W^\pm W^\pm jj$ (EWK)	SHERPA v2.2.2	Signal sample
$W^\pm W^\pm jj$ (EWK)	POWHEG-BOX v2	Systematics sample
$W^\pm W^\pm jj$ (QCD)	SHERPA v2.2.2	
Diboson	SHERPA v2.2.2	Both bosons decay leptonically ( $llll$ , $lll\nu$ , $ll\nu\nu$ )
Triboson	SHERPA v2.2.1	One boson decays leptonically, the other hadronically
$W + \text{jets}$	SHERPA v2.2.1	
$Z + \text{jets}$	Madgraph5_aMC@NLO	
$V\gamma$	SHERPA v2.1.1	
$V\gamma jj$ (EWK)	SHERPA v2.2.4	
$t\bar{t}V$	Madgraph5_aMC@NLO	
$t\bar{t}$	POWHEG-BOX v2	
Single top	POWHEG-BOX v1	EWK $t$ -, $s$ -, & $Wt$ -channels

Table 5.2: Summary of MC samples used in the analysis.

intentionally loose set of criteria in order to have high acceptance for rejecting backgrounds with additional leptons (i.e.  $WZ \rightarrow 3l\nu jj$ ). Signal leptons are then required to satisfy a much tighter *signal selection* aimed at suppressing backgrounds from non-prompt or fake leptons. A third set of lepton selection criteria, the *loose selection*, defines a sample enriched in non-prompt leptons, and it is used in the fake factor method for estimating the non-prompt background, discussed in detail in Section 5.3.4. Jets are only required to pass one set of selection criteria. These selections are detailed in the following sections and summarized in Table 5.3 for muons, Table 5.4 for electrons, and Table 5.5 for jets.

### 5.2.1.1 Muon candidate selection

Cuts on muon  $p_T$  serve to reject low momentum leptons from background processes and additional collisions from pileup events. Preselected muons must have  $p_T > 6$  GeV and signal muons  $p_T > 27$  GeV. The  $p_T$  requirement for loose muons is lower than for signal muons,  $p_T > 15$  GeV, for reasons that are discussed in Section 5.3.4. **TODO:** reference proper subsection when it's done

Muons are required to fall within the detector's  $\eta$  acceptance:  $|\eta| < 2.7$  for preselected muons, which is tightened to  $|\eta| < 2.5$  for the signal muons.

Cuts on the transverse and longitudinal impact parameters are applied to ensure that the candidate muon originated from the primary particle interaction and not some other source, such as a heavy flavor decay. The preselection and the loose selection both have looser requirements on the transverse impact parameter significance ( $d_0/\sigma_{d_0}$ ) than the signal selection; all three have the same requirement on the transverse impact parameter ( $|z_0 \times \sin \theta|$ ).

Finally, the muon candidates are required to pass a particle identification and an isolation criteria as defined in [69]. The methods used in constructing the identification and isolation workingpoints are described in more detail in Section 3.2.4.2. The muon identification serves to select prompt muons with high efficiency and well measured momenta. This analysis uses two different workingpoints, **Loose** for preselected muons and **Medium** for loose and signal muons, where **Medium** muons are a tighter subset of those that pass the **Loose** requirement. Muon isolation is a measurement of detector activity around the muon candidate, and it is measured with both track-based and calorimeter-based variables. The isolation workingpoint used for the signal muons, **Gradient**, is defined such that there is 90% or better background rejection efficiency for 25 GeV muons, and 99% efficiency at 60 GeV. There is no minimum isolation requirement for preselected or loose muons. Loose muons are additionally required to fail one or both of the signal transverse impact parameter cut and signal isolation requirement.

Muon preselection	
Momentum cut	$p_T > 6$ GeV
Angular acceptance	$ \eta  < 2.7$
Longitudinal impact parameter	$ z_0 \times \sin \theta  < 0.5$ mm
Transverse impact parameter	$d_0/\sigma_{d_0} < 10$
Particle identification	<b>Loose</b>

Muon signal selection	
Momentum cut	$p_T > 27$ GeV
Angular acceptance	$ \eta  < 2.5$
Longitudinal impact parameter	$ z_0 \times \sin \theta  < 0.5$ mm
Transverse impact parameter	$d_0/\sigma_{d_0} < 3$
Particle identification	<b>Medium</b>
Particle isolation	<b>Gradient</b>

Muon loose selection	
Momentum cut	$p_T > 15$ GeV
Angular acceptance	$ \eta  < 2.5$
Longitudinal impact parameter	$ z_0 \times \sin \theta  < 0.5$ mm
Transverse impact parameter	$d_0/\sigma_{d_0} < 10$
Particle identification	<b>Medium</b>
Fail signal transverse impact parameter and/or isolation cuts	

Table 5.3: Muon selection criteria. All muons are required to pass the preselection (top), and then either the signal (middle) or loose (bottom) criteria is applied to the preselected electrons.

---

1182    **5.2.1.2 Electron candidate selection**

1183    The electron candidate selections are very similar to those for muons. The  $p_T$  cut starts at  $p_T >$   
 1184    6 GeV for the preselection, increases to  $p_T > 20$  GeV for loose electrons, and finally to  $p_T > 27$  GeV  
 1185    for signal electrons. The  $|\eta|$  cut for electrons requires  $|\eta| < 2.47$  for all electrons, with the region  
 1186     $1.37 \leq |\eta| \leq 1.52$  removed from loose and signal electrons. This region is where the electromagnetic  
 1187    calorimeter transitions from the barrel to the endcaps and is not fully instrumented. Both the  
 1188    transverse and longitudinal impact parameter cuts are the same for all electron selections.

1189    The electron particle identification uses a multivariate likelihood technique (LH) [70] detailed  
 1190    in Section 3.2.4.3. Preselected electrons must pass the loosest LH workingpoint `LooseLH` with  
 1191    an additional requirement that there be a reconstructed track hit in the first layer of the pixel  
 1192    detector (a so-called *B*-layer hit). The LH requirement for the loose and signal electrons the tightness  
 1193    of the identification using `MediumLH` and `TightLH`, respectively. As for isolation, the `Gradient`  
 1194    workingpoint is required for signal electrons only. The loose electrons must fail one or both of the  
 1195    signal identification and isolation requirements.

1196    **5.2.1.3 Jet candidate selection**

1197    The final objects that need to pass selection are jets. Jets are clustered using the anti- $k_t$  algo-  
 1198    rithm [71] within a radius of  $\Delta R = 0.4$ . The jets are then calibrated using  $E_T$ - and  $\eta$ -dependent  
 1199    correction factors that are trained using MC simulations [72]. These calibrated jets are then re-  
 1200    quired to have  $p_T > 30$  GeV if they lie in the forward regions of the detector ( $2.4 < |\eta| < 4.5$ ) and  
 1201     $p_T > 25$  GeV in the central region ( $|\eta| \leq 2.4$ ). In order to suppress pileup jets, the so-called jet-  
 1202    vertex-tagger (JVT) discriminant associates a jet with the primary interaction vertex [73]; central  
 1203    jets with  $p_T > 60$  GeV are required to pass the `Medium` JVT workingpoint, which corresponds to  
 1204    an average efficiency of over 92%. Finally, the jets are required to be separated by selected prompt  
 1205    leptons by at least  $\Delta R(j, l) > 0.3$ .

1206    **5.2.1.4 Treatment of overlapping objects**

1207    In the event that one or more objects are reconstructed very close to each other, there is the  
 1208    possibility for double-counting if both originated from the same object. The procedure by which  
 1209    this ambiguity is resolved is called *overlap removal* (OR). The standard ATLAS recommendation  
 1210    for OR is implemented in this analysis [74, 75] and is summarized in Table 5.6.

Electron preselection	
Momentum cut	$p_T > 6$ GeV
Angular acceptance	$ \eta  < 2.47$
Longitudinal impact parameter	$ z_0 \times \sin \theta  < 0.5$ mm
Transverse impact parameter	$d_0/\sigma_{d_0} < 5$
Particle identification	<b>LooseLH + <math>B</math>-layer hit</b>

Electron signal selection	
Momentum cut	$p_T > 27$ GeV
Angular acceptance	$ \eta  < 2.47$ , excluding $1.37 \leq  \eta  \leq 1.52$
Longitudinal impact parameter	$ z_0 \times \sin \theta  < 0.5$ mm
Transverse impact parameter	$d_0/\sigma_{d_0} < 5$
Particle identification	<b>TightLH</b>
Particle isolation	<b>Gradient</b>

Electron loose selection	
Momentum cut	$p_T > 20$ GeV
Angular acceptance	$ \eta  < 2.47$ , excluding $1.37 \leq  \eta  \leq 1.52$
Longitudinal impact parameter	$ z_0 \times \sin \theta  < 0.5$ mm
Transverse impact parameter	$d_0/\sigma_{d_0} < 5$
Particle identification	<b>MediumLH</b>
Fail signal identification and/or isolation cuts	

Table 5.4: Electron selection criteria. All electrons are required to pass the preselection (top), and then either the signal (middle) or loose (bottom) criteria is applied to the preselected electrons.

Jet selection	
Momentum cut	$p_T > 30$ GeV for $2.4 <  \eta  < 4.5$ $p_T > 60$ GeV for $ \eta  < 2.4$
JVT cut	<b>Medium</b>
Jet-lepton separation	$\Delta R(j, l) > 0.3$

Table 5.5: Jet selection criteria. All jets are required to pass the above selection in order to be used in the analysis.

1211 Since electrons leave a shower in the EM calorimeter, every electron has a jet associated with  
 1212 it. Therefore, any jets close to an electron (within  $\Delta R(e, j) < 0.2$ ) are rejected due to the high  
 1213 probability that they are the same object. On the other hand, when jets and electrons overlap  
 1214 within a large radius of  $0.2 < \Delta R(e, j) < 0.4$ , it is likely that the electron and jet both are part of  
 1215 a heavy-flavor decay, and the electron is rejected.

1216 High energy muons can produce photons via bremsstrahlung radiation or collinear final state  
 1217 radiation which results in a nearby energy deposit in the calorimeters. Non-prompt muons from  
 1218 hadronic decays produce a similar signature; however, in this case the jet has a higher track multiplicity  
 1219 in the ID. It is possible to address both cases by rejecting the jet when the ID track multiplicity  
 1220 is less than three and otherwise rejecting the muon for jets and muons within  $\Delta R(\mu, j) < 0.4$ .

1221 In addition to the case above where muon bremsstrahlung results in a nearby reconstructed jet,  
 1222 the ID track from the muon and the calorimeter energy deposit can lead to it being reconstructed  
 1223 as an electron. In this case, if both a muon and an electron share a track in the ID, the muon is  
 1224 kept and the electron is rejected, unless the muon is calorimeter-tagged<sup>12</sup>, in which case the muon  
 1225 is removed in favor of the electron.

Overlap	Check	Result (remove → keep)
Electron & Jet	$\Delta R(e, j) < 0.2$	Jet → electron
	$0.2 < \Delta R(e, j) < 0.4$	Electron → jet
Muon & Jet	$\Delta R(\mu, j) < 0.4$ and Jet $N_{ID}$ tracks $< 3$	Jet → muon
	$\Delta R(\mu, j) < 0.4$ and Jet $N_{ID}$ tracks $\geq 3$	Muon → jet
Electron & Muon	Shared ID track	Electron → muon
	Shared ID track & muon is calo-tagged	Muon → electron

Table 5.6: Summary of the overlap removal procedure used in the analysis. If the criteria in the “check” column is met, in the “result” column, the object on the left of the arrow is removed in favor of the object on the right.

### 1226 5.2.2 Signal event selection

1227 After the objects have been selected, cuts are applied on a per-event level to select  $W^\pm W^\pm jj$  signal  
 1228 events. The event selection is summarized in Table 5.8 and is detailed in this section. It includes  
 1229 the results of an optimization performed using a multidimensional grid scan.

1230 The initial event selection begins by choosing events that pass one or more of the trigger re-  
 1231 quirements listed in Table 5.7. At least one signal lepton is “matched” to a passed trigger in order

<sup>12</sup>A calorimeter-tagged (CT) muon is a muon that is identified by matching an ID track to a calorimeter energy deposit. CT muons have relatively low reconstruction efficiency compared to those measured by the MS, but can be used to recover acceptance in regions of the detector where the MS does not have full coverage [69].

to ensure that it was indeed a signal lepton that fired the trigger. A collection of *event cleaning* cuts must also be passed in order to remove events collected during periods in which one or more components of the detector was not operating optimally. Finally, the events are required to contain at least one interaction vertex. An event can have multiple reconstructed vertices from additional proton-proton collisions that occurred in the same bunch crossing. In this case, the *primary vertex* is determined by choosing the vertex with the largest sum of the  $p_T^2$  of its associated tracks.

	2015 data	2016 data
Electrons	$p_T > 24$ GeV and Medium ID	$p_T > 26$ GeV and Tight ID and Loose isolation
	$p_T > 60$ GeV and Medium ID	$p_T > 60$ GeV and Medium ID
	$p_T > 120$ GeV and Loose ID	$p_T > 140$ GeV and Loose ID
Muons	$p_T > 20$ GeV and Loose isolation $p_T > 50$ GeV	$p_T > 26$ GeV and Medium isolation $p_T > 50$ GeV

Table 5.7: Summary of trigger requirements for electrons and muons for  $\sqrt{s} = 13$  TeV data collected in 2015 and 2016. At least one of the triggers must be satisfied.

Events are then required to contain exactly two signal leptons with the same electric charge. The dilepton pair must have a combined invariant mass of  $m_{ll} \geq 20$  GeV in order to suppress low mass Drell-Yan backgrounds. Two additional selections are applied to events in the  $ee$ -channel: both electrons are required to have  $|\eta| < 1.37$  with an invariant mass at least 15 GeV away from the  $Z$ -boson mass to reduce events where one electron is reconstructed with the wrong charge (this background will be discussed in more detail in Section 5.3 TODO: Replace with proper subsection once it's written). To suppress backgrounds from events with more than two leptons, events with more than two leptons passing the preselection are vetoed.

Missing transverse energy ( $E_T^{\text{miss}}$ ) represents any particles that escape the detector without being measured, such as neutrinos, and is defined as the magnitude of the vector sum of transverse momenta of all reconstructed objects. It can be difficult to calculate accurately, as it involves measurements from all subsystems within the detector, and it is sensitive to any corrections that may be applied to the reconstructed physics objects [76]. These corrections, including the momentum smearing for muons, energy scale and smearing for electrons, and jet calibrations, are propagated to the  $E_T^{\text{miss}}$  calculation. Events are required to contain  $E_T^{\text{miss}} > 30$  GeV in order to account for the two neutrinos from the  $W$  boson decays.

At least two jets are required. The leading and subleading jets must have  $p_T > 65$  GeV and  $p_T > 35$  GeV, respectively, and are referred to as the *tagging jets*. Events are vetoed if they contain one or more jets that have been tagged as a  $b$ -jet to suppress backgrounds from heavy flavor decays

(especially top quark events). The  $b$ -tagging algorithm used by ATLAS is a boosted decision tree (BDT) called MV2c10, and this analysis uses a workingpoint with 85% efficiency [77].

Finally, cuts are applied on the VBS signature outlined in Section 5.0.3. The tagging jets are required to have a dijet invariant mass  $m_{jj} > 200$  GeV and be separated in rapidity by  $|\Delta y_{jj}| > 2.0$ . This preferentially selects the VBS EWK events over the QCD-produced  $W^\pm W^\pm jj$  events.

Event selection	
Event preselection	Pass at least one trigger with a matched lepton Pass event cleaning At least one reconstructed vertex
Lepton selection	Exactly two leptons passing signal selection Both signal leptons with the same electric charge $ \eta  < 1.37$ and $ M_{ee} - M_Z  > 15$ GeV ( $ee$ -channel only) Veto events with more than two preselected leptons
Missing transverse energy	$E_T^{\text{miss}} \geq 30$ GeV
Jet selection	At least two jets Leading jet $p_T > 65$ GeV Subleading jet $p_T > 35$ GeV $m_{jj} > 200$ GeV $N_{b\text{-jet}} = 0$ $ \Delta y_{jj}  > 2.0$

Table 5.8: The signal event selection.

### 5.3 Background estimations

The major sources of background events are summarized in Section 5.0.4, and the methods used to estimate them are detailed in this section. Prompt backgrounds from  $ZZ$  and  $t\bar{t}V$  are estimated directly from MC simulations. The shape of the  $WZ$  and  $V\gamma$  backgrounds are taken from MC, and the predicted yeilds are normalized to the data predictions in dedicated control regions, as outlined in Sections 5.3.1 and 5.3.2, respectively. Opposite sign events with a charge misidentified electron are estimated by a data-driven background method which is summarized in Section 5.3.3. Finally, a *fake factor* method is used to estimate the contributions from non-prompt backgrounds and is the subject of Section 5.3.4.

#### 5.3.1 Estimation of the $WZ$ background

The dominant background involving prompt leptons comes from  $WZ + \text{jets}$  events. The contribution is estimated from MC simulation and normalized to data in a control region enriched in  $WZ$  events

defined by the same event selection as Table 5.8 for the signal region, with the following changes applied to increase the purity of the  $WZ$  process:

- The third lepton veto is inverted, requiring a third lepton with  $p_T > 15$  GeV
- Two of the leptons must make a same-flavor opposite-sign pair. If more than one pair exists, the one with  $m_{ll}$  closest to the  $Z$  boson mass is chosen.
- The trilepton invariant mass is required to be  $m_{lll} > 106$  GeV to reduce contributions from  $Z\gamma$  and  $Z+jets$

Once the event yields in the control region are calculated, they are propagated to the final signal region fit, detailed in Section 5.4.1, in a single bin combining all the lepton channels. The systematic uncertainties of the  $WZ$  background are also calculated at this time. The event yields for the  $WZ$  control region are listed in Table 5.9, and distributions of the leading lepton  $p_T$  and  $\eta$  as well as trilepton invariant mass  $m_{lll}$  are found in Figures 5.10 and 5.9, respectively.

Event yields in the $WZ$ control region	
$WZ$	$197.9 \pm 1.4$
$ZZ$	$14.1 \pm 0.3$
Triboson	$1.26 \pm 0.1$
top	$10.8 \pm 1.1$
$Z\gamma$	$3.1 \pm 1.1$
$Z+jets$	$2.5 \pm 1.4$
Total prediction	$229.7 \pm 2.5$
Data	$201 \pm 14.2$

Table 5.9: Event yields in the  $WZ$  control region before normalization. All lepton flavor channels are combined.

### 5.3.2 Estimation of the $V\gamma$ background

Events from  $V\gamma$  processes can pass selection if the photon converts into an  $e^+e^-$  pair and one of the electrons passes the selection criteria. The background is estimated from MC simulations which are then scaled by a normalization factor calculated from a control region enriched in  $Z(\mu^+\mu^-)\gamma$  events. This control region selects two opposite-sign muons and an additional electron that is assumed to come from the photon conversion. The full event selection is detailed in Table 5.10.

The  $Z\gamma$  MC samples available do not cover the full range of  $p_T^\gamma$  and  $\Delta R(\gamma, l)$ ; thus, additional Drell-Yan samples ( $Z+jets$ ) are used to fill out the phase space. Overlap between the two samples

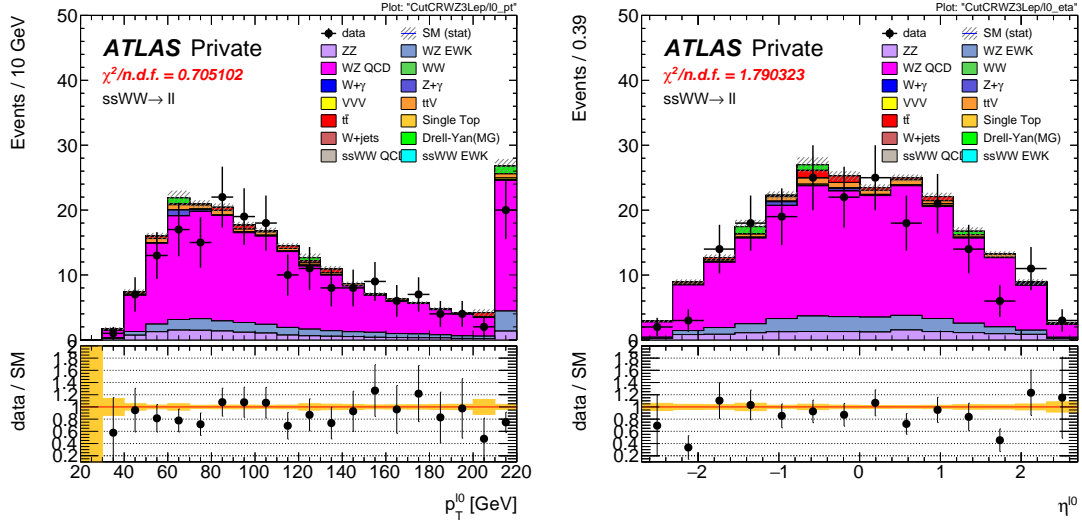


Figure 5.9: Leading lepton  $p_T$  (left) and  $\eta$  (right) distributions in the  $WZ$  control region before normalization. All lepton channels are combined.

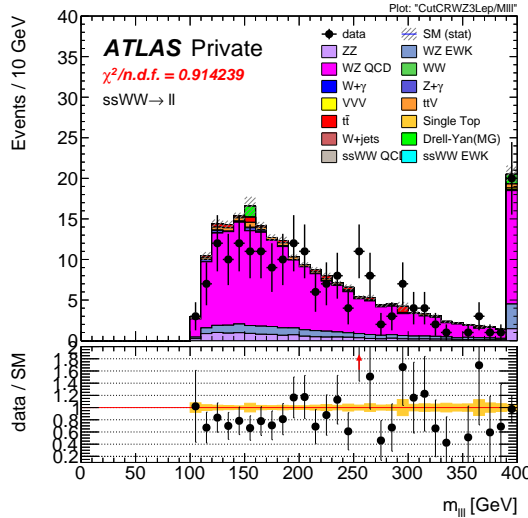


Figure 5.10: Trilepton invariant mass  $m_{lll}$  distribution in the  $WZ$  control region before normalization. All lepton channels are combined.

$V\gamma$ control region
Exactly two muons with $p_T > 27$ GeV and $p_T > 20$ GeV
Exactly one additional electron with $p_T > 15$ GeV
Remove overlap between $Z+jets$ and $Z\gamma$
Di-muon + photon invariant mass $75 < M_{\mu\mu\gamma} < 100$ GeV
$E_T^{\text{miss}} < 30$ GeV

Table 5.10: Selection criteria for the  $V\gamma$  control region.

are removed based to avoid double counting. Events with final state photons at truth level are checked to ensure that the photon did not originate from a hadronic decay. Cuts on  $p_T^\gamma > 10$  GeV and  $\Delta R(\gamma, l) > 0.1$  are then applied at generator level, and  $Z\gamma$  events that fail and  $Z+jets$  events that pass this additional selection are removed.

The normalization factor is calculated directly from the event yields in the  $V\gamma$  control region rather than in the signal fit, as is done for the  $WZ$  background. The event yields are listed in Table 5.11, and the normalization factor is determined to be 1.77. No MC events from  $Z\gamma$  processes survive the full event selection; thus, the scaling is only applied to the  $W\gamma$  background in the signal region. A systematic uncertainty of 44% is assigned to the background based off of the uncertainties in the calculation of the normalization factor.

Event yields in the $V\gamma$ control region	
$Z\gamma$	$24.6 \pm 3.3$
$Z+jets$	$3.0 \pm 1.5$
diboson + triboson	$6.7 \pm 0.3$
top	$1.5 \pm 0.5$
Total prediction	$35.8 \pm 3.7$
Data	$57 \pm 7.6$

Table 5.11: Event yields in the  $V\gamma$  control region. The  $V\gamma$  scale factor of 1.77 is calculated by scaling up the  $Z\gamma$  and  $Z+jets$  backgrounds to account for the difference between the data and predicted total background.

### 5.3.3 Estimation of backgrounds from charge misidentification

If an electron's charge is mis-reconstructed, it can lead to a real, opposite-sign lepton pair passing the same-sign requirement in the event selection. There are two primary reasons this can occur:

1. An electron emits a photon via bremsstrahlung which then converts into an electron-positron pair, and the conversion track with the wrong electric charge is matched to the original electron. This is the dominant process leading to charge flip, and it is highly dependent on the electron  $\eta$  due to the different amount of detector material the electron passes through.
2. The curvature of the electron's track is mismeasured, resulting in the wrong charge being assigned. This process is dependent on the momentum of the electron, as its track becomes more straight as the momentum of the electron increases.

In order to estimate this background, the rate at which an electron's charge is misidentified is calculated from  $Z \rightarrow e^+e^-$  MC simulation. It is known that the MC does not perfectly model

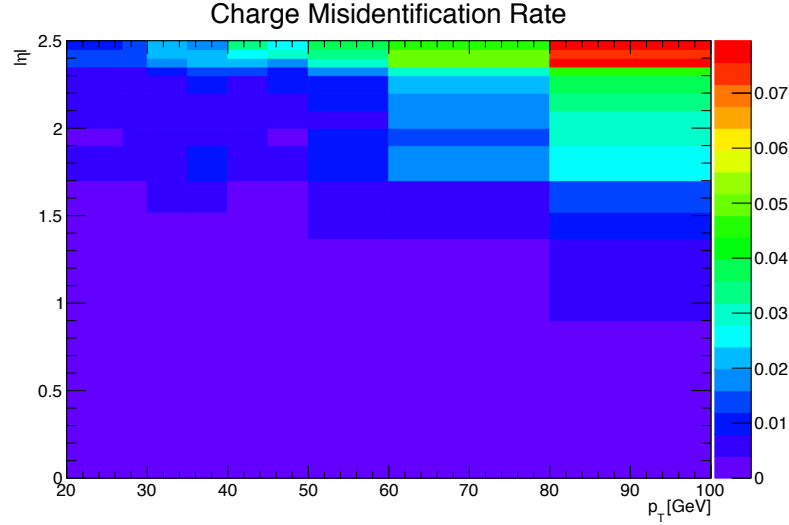


Figure 5.11: Charge misidentification rates for electrons as a function of  $|\eta|$  and  $p_T$ . Rates are calculated from  $Z \rightarrow e^+e^-$  MC after applying scale factors to approximate the charge mis-ID rates in data.

the material effects leading to charge flip; as a result, scale factors are applied to the MC in order for it to better reflect the real performance. These scale factors are obtained from the ratio of charge mis-ID rates in data and uncorrected MC in [46] following the method outlined in [78]. Once the scale factors are applied, the charge misidentification rate  $\varepsilon$  can be extracted by comparing the electron’s reconstructed charge with the charge of its truth particle:

$$\varepsilon(\eta, p_T) = \frac{N_{\text{wrong charge}}}{N_{\text{prompt electrons}}} \quad (5.1)$$

The charge mis-ID rate is calculated in bins of electron  $|\eta|$  and  $p_T$  and varies from below 0.1% in the

central region of the detector up to 8% in the forward regions for high  $p_T$  (above 90 GeV) electrons.

A two-dimensional plot of  $\varepsilon$  can be found in Figure 5.11.

Given the charge flip rate  $\varepsilon(\eta, p_T)$ , the rate at which an electron has its charge correctly reconstructed is  $(1 - \varepsilon)$ . Thus there are three possible combinations of charge identification, assuming a two-electron event:

- 1327 1. Both electrons are reconstructed correctly:  $(1 - \varepsilon)^2$
- 1328 2. Both electrons are mis-reconstructed:  $\varepsilon^2$
- 1329 3. Only one electron is mis-reconstructed:  $2\varepsilon(1 - \varepsilon)$

1330 In order to estimate the size of the background from charge misidentification, opposite-sign events  
 1331 are selected using the default event selection for a given signal or control region with the same-sign  
 1332 requirement inverted. These events are then weighted by the probability for one of the electrons to  
 1333 be reconstructed with the wrong charge:

$$\omega = \frac{\varepsilon_1(1 - \varepsilon_2) + \varepsilon_2(1 - \varepsilon_1)}{(1 - \varepsilon_1)(1 - \varepsilon_2) + \varepsilon_1\varepsilon_2} \quad (5.2)$$

1334 where the subscripts 1 and 2 refer to the leading and subleading electrons, respectively, and  $\varepsilon_i$  is a  
 1335 function of the  $\eta$  and  $p_T$  of the  $i^{\text{th}}$  electron. In the case of an event with only one electron and one  
 1336 muon, Equation 5.2 simplifies:

$$\omega = \frac{\varepsilon}{1 - \varepsilon} \quad (5.3)$$

1337 This method assumes that there is little contamination from fake electrons in the opposite-sign  
 1338 sample, and this has been verified with MC simulation.

1339 Additionally, charge-flipped electrons tend to be reconstructed with lower energy when compared  
 1340 to electrons with the correct charge. This is due to energy loss from the material interactions that  
 1341 can cause the charge to be misidentified. A correction factor is calculated from MC simulations,  
 1342 comparing the  $p_T$  of the truth electron to its reconstructed counterpart:

$$\alpha = \frac{\left(\frac{p_T^{\text{reco}}}{p_T^{\text{truth}}} - 1\right)_{\text{correct charge}}}{\left(\frac{p_T^{\text{reco}}}{p_T^{\text{truth}}} - 1\right)_{\text{wrong charge}}} \quad (5.4)$$

1343 The correction is then applied to the  $p_T$  of the charge-flipped electron via

$$p_T = p_T^0 / (1 + \alpha) + dE \quad (5.5)$$

1344 where  $p_T^0$  is the uncorrected  $p_T$  of the electron and  $dE$  is a gaussian smearing factor centered at  
 1345 zero with a width related to the energy resolution. Since which electron is misreconstructed is never  
 1346 determined in this method, in the case of a two-electron event, the energy correction is applied  
 1347 randomly to one of the two electrons based on the probabilities for them to be charge-flipped. This  
 1348 also determines the overall sign of the event; the charge of the electron that does not receive the  
 1349 correction is taken to be the charge for both.

1350 Systematic uncertainties on the charge mis-ID rates are calculated by generating two additional  
 1351 sets of rates with the uncertainties on the scale factors varied up and down. The size of the esti-  
 1352 mated charge flip background without the energy correction applied is also taken as a systematic  
 1353 uncertainty. These systematic uncertainties are estimated to be approximately  $\pm 15\%$ .

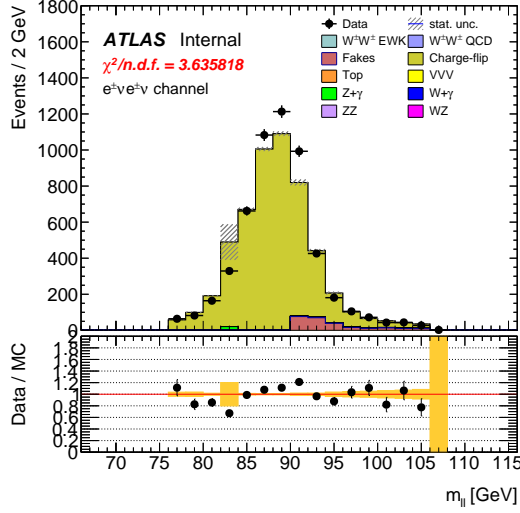


Figure 5.12: Dilepton invariant mass distribution  $m_{ll}$  for the  $ee$  channel in the same-sign inclusive VR.

### 1354 5.3.3.1 Validation of the charge misidentification estimate

1355 The performance of the charge misidentification estimation is tested in the same-sign inclusive  
 1356 validation region (VR), defined in Table 5.12. For  $ee$  events, the mass of the dilepton pair is required  
 1357 to lie within 15 GeV of the  $Z$  boson mass to increase the purity of the charge flip background.  
 1358  $t\bar{t}$  production, which can contribute to both the charge mis-ID and fake lepton backgrounds, is  
 1359 suppressed by the  $b$ -jet veto. The di-electron invariant mass is shown in Figure 5.12, and distributions  
 1360 of the leading and subleading electron  $p_T$  in the  $ee$ -channel are shown in Figure 5.13 with the  $Z$   
 1361 mass cut inverted. Agreement between data and prediction is seen within the total statistical and  
 1362 systematic uncertainties in the VR.

Same-sign inclusive VR
Exactly 2 same-sign signal leptons
$p_T > 27$ GeV for both leptons
$m_{ll} > 20$ GeV
$ m_{ee} - m_Z  > 15$ GeV ( $e^\pm e^\pm$ -channel only)
$N_{b\text{-jet}} = 0$

Table 5.12: Selection criteria for the same-sign inclusive validation region.

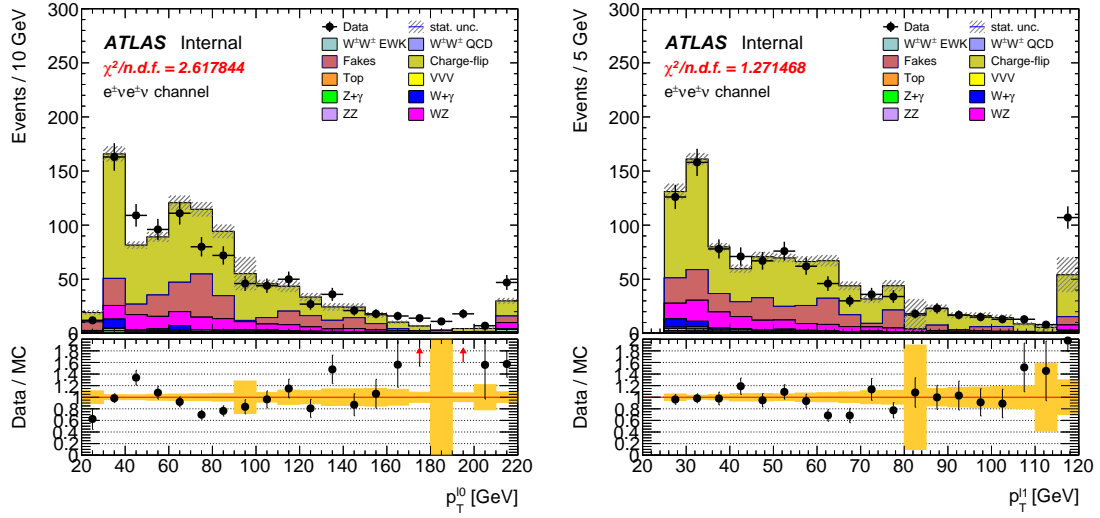


Figure 5.13:  $p_T$  distributions for the leading (left) and subleading (right) electron for the  $ee$  channel in the same-sign inclusive VR. In these plots, the cut requiring  $m_{ee}$  to fall within the  $Z$  mass window has been inverted in order to test the modelling away from the  $Z$  peak.

### 1363 5.3.4 Estimation of non-prompt backgrounds with the fake factor method

1364 Events with one prompt lepton produced in association with hadronic jets can pass the event selection  
 1365 if a jet is misidentified as a charged lepton or if a non-prompt lepton from the decay of a heavy  
 1366 flavor particle (such as  $b$ - and  $c$ -hadrons) passes the signal lepton criteria. These misidentified jets  
 1367 and non-prompt leptons are collectively referred to as *fake leptons*, or simply *fakes*. The rate at  
 1368 which a fake lepton is misidentified is generally not modelled well enough by the MC to accurately  
 1369 estimate their contributions directly from simulation. Therefore, a data-driven technique called the  
 1370 *fake factor* is used to estimate the size and shape of background processes from fake leptons. In this  
 1371 analysis, a new modification to the fake factor is used involving the particle isolation variables; the  
 1372 method is outlined in the context of the *default* fake factor in Section 5.3.4.1, and the modified fake  
 1373 factor is outlined in Section 5.3.4.2.

#### 1374 5.3.4.1 Overview of the default fake factor method

1375 The goal of the fake factor method is to measure the fake rate from real collision events in a region  
 1376 enriched in fake leptons and use it to estimate the size of the fake lepton background in a chosen  
 1377 signal or control region. This is done by creating two samples using different lepton definitions:

- 1378 1. The *nominal* sample is made up of leptons passing the signal selection.

1379     2. The *loose* sample is made up of leptons that fail the signal selection while still passing a  
 1380        loosened set of criteria. This sample is enriched in fake leptons and is orthogonal to the set of  
 1381        signal leptons.

1382     Using the sets of nominal and loose leptons, a fake factor  $f$  can be calculated in a region enriched  
 1383        in processes that are prone to producing fake leptons:

$$f = \frac{N_{\text{nominal}}}{N_{\text{loose}}} \quad (5.6)$$

1384     Since the fake rate is not expected to be constant over the entire phase space, the fake factor can  
 1385        be divided into bins:

$$f(b) = \frac{N_{\text{nominal}}(b)}{N_{\text{loose}}(b)} \quad (5.7)$$

1386     where  $b$  represents the bin number. In this analysis, the fake factor is binned in lepton  $p_T$ .

1387     In order to estimate the fake background contribution in a given signal or control region, the  
 1388        fake factor is applied to a second control region with a selection identical to the region of interest  
 1389        with one of the leptons required to satisfy the loose criteria. The region for which the background  
 1390        is estimated contains two nominal leptons and is referred to as *nominal+nominal* ( $NN$ ), and the  
 1391        associated control region where the fake factor is applied contains one nominal and one loose lepton  
 1392        and is referred to as *nominal+loose* ( $NL$ ). The fake background in a  $NN$  region can then be  
 1393        calculated as:

$$N_{NN}^{\text{fake bkg.}} = \sum_b f(b) N_{NL}(b) \quad (5.8)$$

1394     Backgrounds containing two prompt leptons can also enter the  $NL$  region if one of the leptons  
 1395        passes the nominal selection and the other passes the loose selection. Since the fake factor method  
 1396        estimates the fake background by scaling the amount of non-prompt events in the  $NL$  region, if these  
 1397        prompt contributions are not removed, they will be included in the scaling and the background  
 1398        will be overpredicted. The final estimate of the fake background becomes:

$$N_{NN}^{\text{fake bkg.}} = \sum_b f(b) (N_{NL}(b) - N_{NL}^{\text{prompt}}(b)) \quad (5.9)$$

1399     **5.3.4.2 The fake factor with  $p_T^{\text{cone}}$**

1400     When a jet produces a non-prompt lepton, that lepton only carries a fraction of the underlying jet's  
 1401        total momentum. Due to the isolation cut applied to the nominal leptons, they typically carry a

1402 much larger percentage of the underlying jet momentum<sup>13</sup> than the loose leptons (which are allowed  
1403 to fail this criteria).

1404 This discrepancy in the underlying jet momentum fraction can cause problems in the calculation  
1405 of the fake factor  $f$ . Consider the case where two separate events have jets of identical momentum,  
1406 but one produces a non-prompt lepton that passes the nominal selection, and the other produces a  
1407 non-prompt lepton that passes the loose selection. The loose lepton on average will have lower  $p_T$   
1408 than the nominal lepton despite both originating from jets with the same momentum. This can be  
1409 seen explicitly when comparing the  $p_T$  of a muon to its associated truth jet:

$$\Delta p_T(\mu, j) = \frac{p_T(j) - p_T(\mu)}{p_T(j) + p_T(\mu)} \quad (5.10)$$

1410 Since muons are not included in the jet reconstruction algorithm,  $\Delta p_T$  approximates the momentum  
1411 of the muon compared to the rest of the jet. For muons that carry more than 50% of the jet's  
1412 momentum,  $\Delta p_T$  will be negative and vice-versa. The  $\Delta p_T$  distributions for nominal and loose  
1413 muons in  $t\bar{t}$  MC events is shown Figure 5.14, where a 50 GeV jet on average corresponds to a  
1414 35 GeV nominal muon and a 20 GeV loose muon<sup>14</sup>.

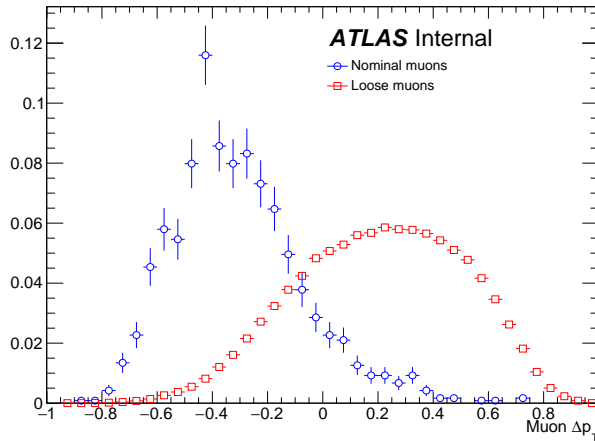


Figure 5.14:  $\Delta p_T$  distributions for nominal (blue) and loose (red) muons in simulated  $t\bar{t}$  events. Each muon has been matched to a truth-level jet. Both distributions are normalized to unit area.

1415 Since the default fake factor defined in Equation 5.7 is binned in lepton  $p_T$ , within a given bin,

<sup>13</sup>Since the isolation variables are a measure of detector activity around the lepton, if other nearby particles carried a significant portion of the jet's momentum, the lepton would likely fail this cut.

<sup>14</sup>To better illustrate the point, here the muon is added back into the jet  $p_T$ , and the corresponding muon  $p_T$  is obtained via  $\Delta p_T(\mu, j) = \frac{(p_T(j) - p_T\mu) - p_T(\mu)}{(p_T(j) - p_T\mu) + p_T(\mu)} = \frac{p_T(j) - 2p_T(\mu)}{p_T(j)}$ .

the underlying jet  $p_T$  spectrum can differ substantially between the numerator and the denominator. Additionally, these differences can vary depending on the process producing the non-prompt leptons or on the specific kinematic selections of the signal or control regions where the fake factor is applied.

Fortunately, the majority of the jet momentum not carried by the non-prompt lepton (excluding neutrinos) can be recovered using isolation variables. A track-based isolation is chosen, referred to as  $p_T^{\text{cone}}$ , and it contains the sum of the  $p_T$  of all particle tracks originating from the primary vertex within a cone of  $\Delta R < 0.3$  around the lepton. Thus, the sample of loose leptons in the denominator of the fake factor calculation is binned in  $p_T + p_T^{\text{cone}}$  rather than simply lepton  $p_T$ . Adding the isolation cone greatly reduces the difference in the fraction of the underlying jet momentum carried by the nominal and loose leptons. To check this, a new  $\Delta p_T$  is calculated between a lepton and its matched truth jet, where the truth jet  $p_T$  has been corrected to include all muons within a cone of  $\Delta R < 0.4$ :

$$p_T(j) = p_T(j_{\text{truth}}) + \sum_{\Delta R < 0.4} p_T(\mu_{\text{truth}}) \quad (5.11)$$

The  $\Delta p_T$  distributions comparing  $p_T$  and  $p_T + p_T^{\text{cone}}$  for nominal and loose leptons using the corrected jet  $p_T$  are found in Figure 5.15, and better agreement is seen between the numerator (nominal) and denominator (loose with  $p_T + p_T^{\text{cone}}$ ) distributions.

The numerator remains binned in lepton  $p_T$ , due to the fact that it is meant to mirror the signal region as closely as possible, and the signal lepton selection does not use  $p_T + p_T^{\text{cone}}$ . The impact of this is expected to be negligible due to the  $p_T^{\text{cone}}$  isolation being small for signal leptons, as shown for muons in Figure 5.16. Finally, the fake factor  $f$  becomes:

$$f(b) = \frac{N_{\text{nominal}}(b(p_T))}{N_{\text{loose}}(b(p_T + p_T^{\text{cone}}))} \quad (5.12)$$

#### 5.3.4.3 Application of the fake factor

The fake factor itself is measured from a sample data events passing a dijet selection requiring exactly one lepton (either passing the nominal or loose selections) and at least one jet. The leading jet must also be  $b$ -tagged and approximately back-to-back with the lepton in order to enhance non-prompt lepton contributions while reducing contributions from processes involving  $W$  and  $Z$  bosons.  $W$  boson events are further suppressed by requiring the sum of the  $E_T^{\text{miss}}$  and the transverse mass of the lepton and  $E_T^{\text{miss}}$  to be less than 50 GeV. The full event selection for the dijet region is summarized in Table 5.13.

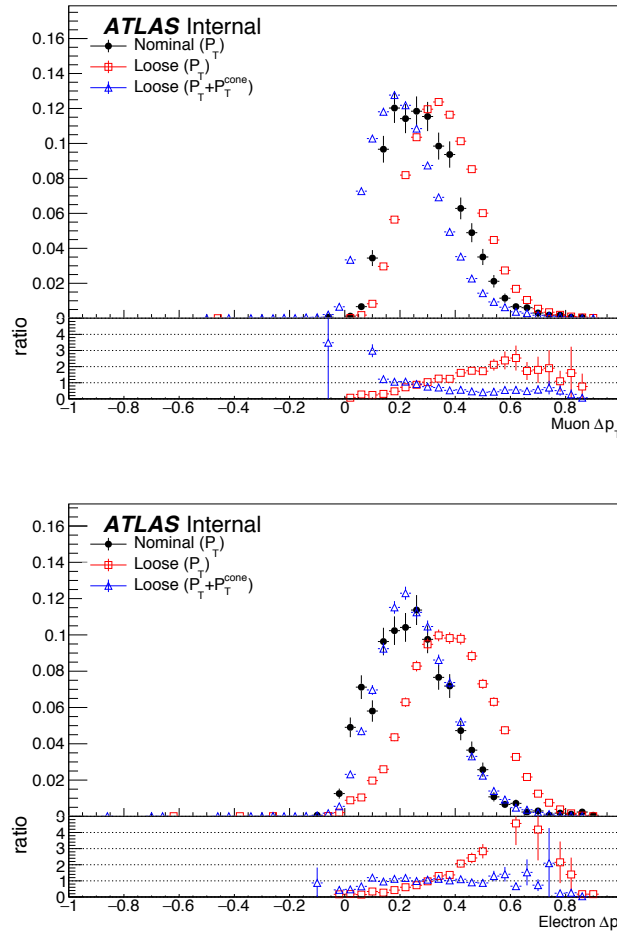


Figure 5.15:  $\Delta p_T$  distributions for muons (top) and electrons (bottom) in simulated  $t\bar{t}$  events. Each lepton has been matched to a truth-level jet, and that truth jet has had its  $p_T$  corrected to include all truth muons within a cone of  $\Delta R < 0.4$ . The nominal leptons are in black.  $\Delta p_T$  is calculated for the loose leptons using  $p_T$  (red) and  $p_T + p_T^{\text{cone}}$  (blue).

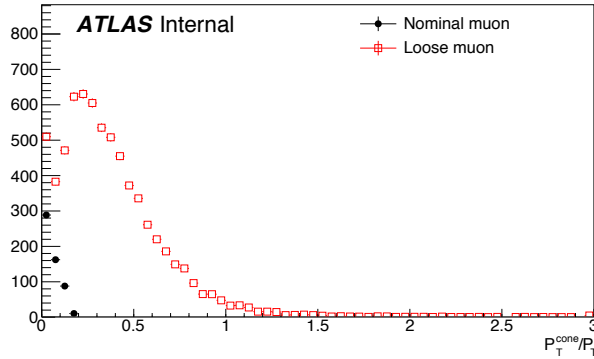


Figure 5.16: Distributions of  $p_T^{\text{cone}}/p_T$  for nominal (black) and loose (red) muons in simulated  $t\bar{t}$  events.

Dijet event selection	
Event preselection	
Exactly one lepton with $p_T > 15$ GeV	
$N_{\text{jet}} > 0$	
Leading jet is $b$ -tagged	
$p_T^{\text{lead. jet}} > 25$ GeV	
$p_T^{\text{lead. jet}} > 30$ GeV if $ \eta_j  > 2.5$	
$ \Delta\phi(l, \text{lead. jet})  > 2.8$	
$m_T(l, E_T^{\text{miss}}) + E_T^{\text{miss}} < 50$ GeV	

Table 5.13: Event selection for the dijet region used for calculating the fake factor. The selected lepton can pass either the nominal (signal) or loose selections. In the case of the nominal leptons, the  $p_T > 27$  GeV requirement is replaced with  $p_T > 15$  GeV.

1443     The numerator sample is constructed from dijet events in which the lepton passes the nominal  
 1444     (signal) selection and is binned in the lepton  $p_T$ . Similarly, the denominator sample is made up of  
 1445     the remaining dijet events where the lepton passes the loose selection and is binned in the lepton  
 1446      $p_T + p_T^{\text{cone}}$ . The nominal and loose leptons pass the signal selection<sup>15</sup> and loose selection, respectively,  
 1447     defined earlier in Table 5.3 for muons and Table 5.4 for electrons. Backgrounds from  $W + \text{jets}$ ,  $Z + \text{jets}$ ,  
 1448      $t\bar{t}$ , and single top processes are estimated from MC simulations requiring one lepton to be prompt  
 1449     using the truth information; these contributions are subtracted from the dijet data. The fake factor  
 1450     is then calculated using Equation 5.12 for muons and for central and forward electrons separately.  
 1451     The muon fake factor is shown in Figure 5.17, and the two electron fake factors are shown in  
 1452     Figure 5.18. The numerical values of the fake factors, including their systematic uncertainties which

<sup>15</sup>The  $p_T > 27$  GeV cut in the signal lepton selection is dropped in favor of the  $p_T > 15$  GeV requirement in the dijet selection.

<sup>1453</sup> will be discussed in Section 5.3.4.4, are listed in Table 5.14.

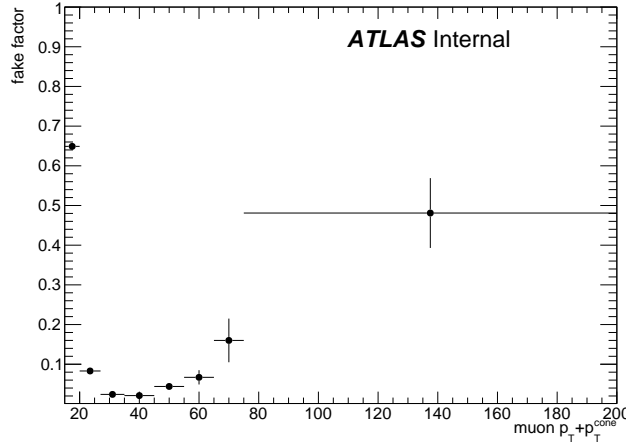


Figure 5.17: The measured fake factor as a function of muon  $p_T + p_T^{\text{cone}}$ . The error bars represent the statistical uncertainty only.

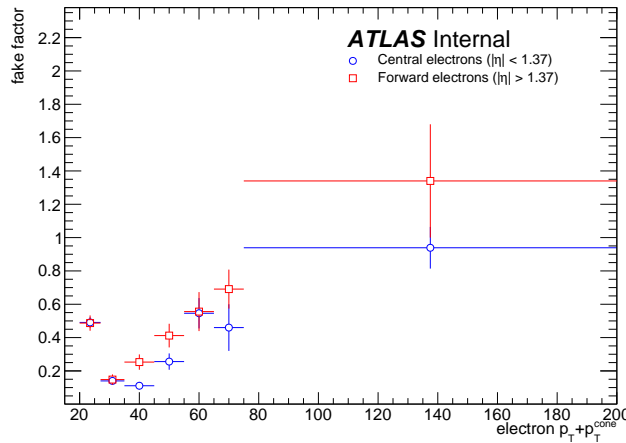


Figure 5.18: The measured fake factor as a function of electron  $p_T + p_T^{\text{cone}}$  in the central ( $|\eta| < 1.37$ , blue) and forward ( $|\eta| > 1.37$ , red) regions of the detector. The error bars represent the statistical uncertainty only.

<sup>1454</sup> In order to properly account for the denominator being binned in  $p_T + p_T^{\text{cone}}$ , special care needs  
<sup>1455</sup> to be taken when estimating the fake background from the  $NL$  regions. For the purposes of the  
<sup>1456</sup> fake factor calculation, it is perhaps more intuitive to consider a loose *object* with  $p_T = p_T + p_T^{\text{cone}}$   
<sup>1457</sup> instead of simply a loose *lepton*, as the lepton and the underlying jet are treated as a whole with this

method. When the lepton  $p_T$  cuts required by a particular signal or control region are applied to nominal and loose leptons, the cut is applied to the  $p_T$  of the nominal lepton and to the  $p_T + p_T^{\text{cone}}$  of the loose object. Similarly, when looking up the fake factor weight for a given  $NL$  event, the value taken from the bin corresponding to the  $p_T + p_T^{\text{cone}}$  of the loose object. Finally, when applying the weight to the event,  $p_T + p_T^{\text{cone}}$  is assigned as the  $p_T$  of the loose object. Figure 5.19 contains a graphical representation of this procedure.

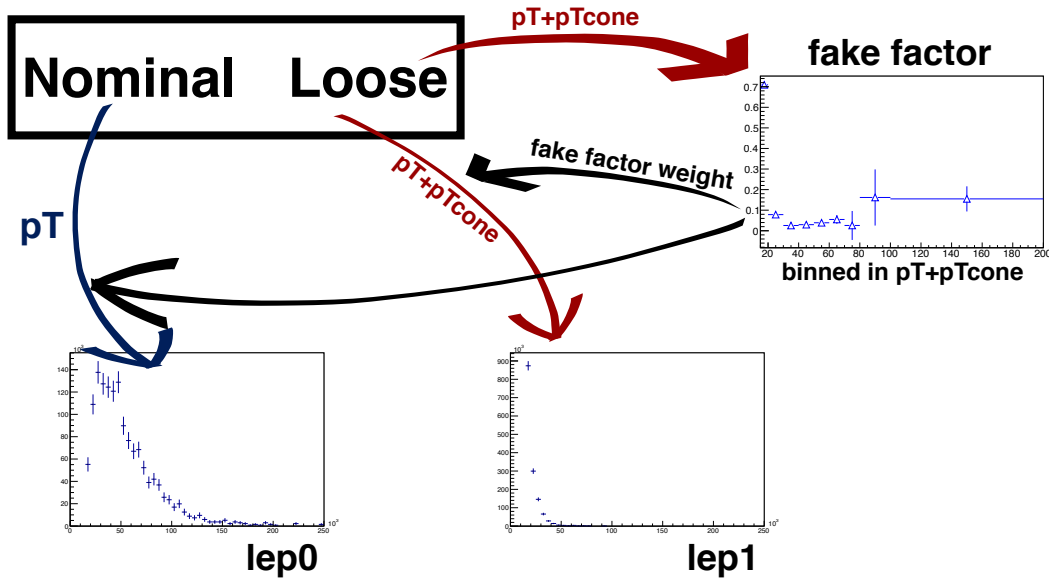


Figure 5.19: Graphical representation of the fake factor application using  $p_T + p_T^{\text{cone}}$ . The value of  $p_T + p_T^{\text{cone}}$  for the loose lepton is used to “look up” the fake factor weight which is then applied to the event. The loose lepton’s  $p_T$  becomes  $p_T + p_T^{\text{cone}}$  for the purpose of the fake background estimation.

Finally, it should be noted that the addition of  $p_T^{\text{cone}}$  to the loose object may cause the loose leptons in the denominator sample to migrate into higher bins. This results in an overall decrease in the number of loose objects in the lower  $p_T + p_T^{\text{cone}}$  bins due to there not being additional leptons at lower  $p_T$  to replace them. Since the fake factor is a ratio of the number of events in a bin, this effect causes the first few bins of the fake factor to increase, as can be seen clearly in Figure 5.17. However, the signal and control regions (and their corresponding  $NL$  regions) contain a  $p_T > 27$  GeV cut that prevents these migrations from negatively impacting the fake estimation.

---

<sup>1471</sup> **5.3.4.4 Systematic uncertainties**

<sup>1472</sup> Four sources of systematic uncertainty are considered: the dijet event selection, the prompt back-  
<sup>1473</sup> ground subtraction, the jet flavor composition, and residual dependence on the underlying jet  $p_T$   
<sup>1474</sup> spectrum. In order to measure the impact of these systematics, new fake factors are computed  
<sup>1475</sup> with each of the systematic variations and the differences from the nominal values are taken as the  
<sup>1476</sup> uncertainty.

- <sup>1477</sup> 1. In order to estimate uncertainties due to the dijet selection, the cut on  $M_T + MET$  is varied  
<sup>1478</sup> by  $\pm 5$  GeV,  $\Delta\phi(l, j)$  by  $\pm 0.1$ , and the jet  $p_T$  cut by  $+5$  GeV.
- <sup>1479</sup> 2. To estimate the systematic uncertainty on the prompt background subtraction, the MC pre-  
<sup>1480</sup> diction in a  $W+jets$  control region is compared to data. The discrepancy between data and  
<sup>1481</sup> MC is found to be approximately 10% [46]. Therefore, the prompt background used for the  
<sup>1482</sup> subtraction is scaled up and down by  $\pm 10\%$ .
- <sup>1483</sup> 3. The difference in the jet flavor composition between the dijet events and the events in the  
<sup>1484</sup>  $NL$  regions can affect the accuracy of the fake background estimation. The dijet sample is  
<sup>1485</sup> dominated by light jets, while the  $NL$  regions tend to be dominated by heavy flavor from  $t\bar{t}$ .  
<sup>1486</sup> To account for this, the fake factor is computed with a  $b$ -jet veto.
- <sup>1487</sup> 4. To measure any residual dependence on the underlying jet  $p_T$  spectrum, the leading jet  $p_T$   
<sup>1488</sup> distribution is reweighted to match the  $p_T$  spectrum of truth jets that produce fake leptons  
<sup>1489</sup> in MC simulations. This results in an increase in the number of nominal and loose leptons at  
<sup>1490</sup> high momentum [46].

<sup>1491</sup> **5.3.4.5 Results of the fake factor**

<sup>1492</sup> The fake background contribution in the signal region is estimated by applying the fake factors  
<sup>1493</sup> to the equivalent  $NL$  region using Equation 5.9, where the fake factor used corresponds to the  
<sup>1494</sup> flavor of the loose lepton in the event. As usual, the prompt background is subtracted from the  
<sup>1495</sup>  $NL$  events using MC simulation. Charge misidentification is handled using the same method as  
<sup>1496</sup> in Section 5.3.3, with an additional set of charge flip rates calculated for loose leptons. The fake  
<sup>1497</sup> background yields in the signal region are listed in Table 5.15. An overall uncertainty of 50% is  
<sup>1498</sup> assigned to the fake background estimation in  $\mu^\pm\mu^\pm$  events, and between 40% to 90% for  $e^\pm e^\pm$  and  
<sup>1499</sup>  $\mu^\pm e^\pm$  events, including both statistical and systematic effects.

fake factor	$p_T[15, 20]$	$p_T[20, 27]$	$p_T[27, 35]$	$p_T[35, 45]$	$p_T[45, 55]$	$p_T[55, 65]$	$p_T[65, 75]$	$p_T[75, 200]$
nominal	$0.649 \pm 0.007$	$0.083 \pm 0.002$	$0.024 \pm 0.002$	$0.021 \pm 0.003$	$0.044 \pm 0.007$	$0.067 \pm 0.018$	$0.160 \pm 0.055$	$0.481 \pm 0.088$
MT+MET	$0.649 \pm 0.007$	$0.082 \pm 0.002$	$0.082 \pm 0.002$	$0.020 \pm 0.003$	$0.045 \pm 0.007$	$0.068 \pm 0.018$	$0.207 \pm 0.062$	$0.523 \pm 0.086$
$\Delta\phi(\ell, j)$	$0.645 \pm 0.008$	$0.083 \pm 0.003$	$0.024 \pm 0.002$	$0.021 \pm 0.004$	$0.045 \pm 0.008$	$0.064 \pm 0.021$	$0.064 \pm 0.058$	$0.438 \pm 0.092$
Jet $p_T$	$0.650 \pm 0.007$	$0.083 \pm 0.002$	$0.024 \pm 0.002$	$0.021 \pm 0.003$	$0.045 \pm 0.007$	$0.069 \pm 0.018$	$0.159 \pm 0.018$	$0.481 \pm 0.088$
$N_{b\text{-jet}} = 0$	$0.724 \pm 0.003$	$0.094 \pm 0.001$	$0.035 \pm 0.001$	$0.025 \pm 0.002$	$0.022 \pm 0.004$	$0.060 \pm 0.015$	$0.026 \pm 0.053$	$0.044 \pm 0.134$
Bkg. subtraction	$0.648 \pm 0.007$	$0.083 \pm 0.002$	$0.024 \pm 0.002$	$0.019 \pm 0.003$	$0.037 \pm 0.007$	$0.044 \pm 0.019$	$0.096 \pm 0.062$	$0.370 \pm 0.082$
Jet $p_T$ Reweighting	$0.649 \pm 0.007$	$0.083 \pm 0.002$	$0.025 \pm 0.002$	$0.022 \pm 0.003$	$0.050 \pm 0.007$	$0.090 \pm 0.017$	$0.224 \pm 0.052$	$0.591 \pm 0.099$
	$0.539 \pm 0.077$	$0.093 \pm 0.007$	$0.025 \pm 0.004$	$0.043 \pm 0.019$	$0.063 \pm 0.014$	$0.085 \pm 0.025$	$0.141 \pm 0.110$	$1.962 \pm 0.492$

(a) Fake factor for muons.

fake factor	$p_T[20, 27]$	$p_T[27, 35]$	$p_T[35, 45]$	$p_T[45, 55]$	$p_T[55, 65]$	$p_T[65, 75]$	$p_T[75, 200]$
nominal	$0.491 \pm 0.031$	$0.140 \pm 0.020$	$0.111 \pm 0.023$	$0.256 \pm 0.049$	$0.546 \pm 0.091$	$0.460 \pm 0.140$	$0.939 \pm 0.125$
MT+MET	$0.493 \pm 0.030$	$0.138 \pm 0.019$	$0.115 \pm 0.022$	$0.261 \pm 0.045$	$0.559 \pm 0.084$	$0.656 \pm 0.091$	$0.802 \pm 0.016$
$\Delta\phi(\ell, j)$	$0.488 \pm 0.032$	$0.137 \pm 0.020$	$0.110 \pm 0.025$	$0.283 \pm 0.053$	$0.503 \pm 0.097$	$0.351 \pm 0.149$	$1.117 \pm 0.255$
Jet $p_T$	$0.489 \pm 0.035$	$0.134 \pm 0.021$	$0.105 \pm 0.025$	$0.224 \pm 0.048$	$0.593 \pm 0.093$	$0.356 \pm 0.144$	$0.928 \pm 0.177$
$N_{b\text{-jet}} = 0$	$0.506 \pm 0.029$	$0.140 \pm 0.018$	$0.111 \pm 0.022$	$0.260 \pm 0.046$	$0.545 \pm 0.084$	$0.546 \pm 0.120$	$0.882 \pm 0.103$
Jet $p_T$	$0.493 \pm 0.032$	$0.146 \pm 0.021$	$0.115 \pm 0.024$	$0.259 \pm 0.049$	$0.550 \pm 0.091$	$0.460 \pm 0.140$	$0.939 \pm 0.125$
$N_{b\text{-jet}} = 0$	$0.387 \pm 0.009$	$0.130 \pm 0.008$	$0.321 \pm 0.012$	$0.473 \pm 0.015$	$0.716 \pm 0.180$	$0.716 \pm 0.180$	$0.716 \pm 0.180$
Bkg. subtraction	$0.488 \pm 0.031$	$0.138 \pm 0.020$	$0.106 \pm 0.023$	$0.248 \pm 0.049$	$0.529 \pm 0.092$	$0.434 \pm 0.143$	$0.888 \pm 0.115$
Jet $p_T$ Reweighting	$0.493 \pm 0.031$	$0.142 \pm 0.020$	$0.115 \pm 0.023$	$0.264 \pm 0.049$	$0.563 \pm 0.090$	$0.485 \pm 0.136$	$0.989 \pm 0.132$
	$0.445 \pm 0.055$	$0.137 \pm 0.037$	$0.065 \pm 0.023$	$0.115 \pm 0.033$	$0.603 \pm 0.047$	$0.104 \pm 0.105$	$0.299 \pm 0.260$

(b) Fake factor for central electrons ( $|\eta| < 1.37$ ).

fake factor	$p_T[20, 27]$	$p_T[27, 35]$	$p_T[35, 45]$	$p_T[45, 55]$	$p_T[55, 65]$	$p_T[65, 75]$	$p_T[75, 200]$
nominal	$0.487 \pm 0.046$	$0.148 \pm 0.031$	$0.253 \pm 0.046$	$0.412 \pm 0.071$	$0.556 \pm 0.117$	$0.691 \pm 0.117$	$1.340 \pm 0.340$
MT+MET	$0.483 \pm 0.045$	$0.152 \pm 0.031$	$0.241 \pm 0.043$	$0.443 \pm 0.070$	$0.565 \pm 0.106$	$0.668 \pm 0.117$	$1.075 \pm 0.189$
$\Delta\phi(\ell, j)$	$0.495 \pm 0.047$	$0.156 \pm 0.033$	$0.271 \pm 0.052$	$0.364 \pm 0.074$	$0.664 \pm 0.107$	$0.749 \pm 0.056$	$0.885 \pm 0.084$
Jet $p_T$	$0.471 \pm 0.051$	$0.158 \pm 0.035$	$0.247 \pm 0.051$	$0.474 \pm 0.085$	$0.283 \pm 0.107$	$0.546 \pm 0.149$	$1.189 \pm 0.266$
$N_{b\text{-jet}} = 0$	$0.478 \pm 0.042$	$0.170 \pm 0.031$	$0.274 \pm 0.046$	$0.389 \pm 0.066$	$0.645 \pm 0.104$	$0.757 \pm 0.102$	$1.319 \pm 0.326$
Jet $p_T$	$0.523 \pm 0.048$	$0.149 \pm 0.033$	$0.235 \pm 0.045$	$0.429 \pm 0.073$	$0.555 \pm 0.117$	$0.691 \pm 0.117$	$1.340 \pm 0.340$
$N_{b\text{-jet}} = 0$	$0.525 \pm 0.011$	$0.234 \pm 0.013$	$0.644 \pm 0.016$	$0.710 \pm 0.014$	$0.274 \pm 0.316$	$0.274 \pm 0.316$	$0.274 \pm 0.316$
Bkg. subtraction	$0.484 \pm 0.046$	$0.146 \pm 0.031$	$0.248 \pm 0.046$	$0.406 \pm 0.071$	$0.545 \pm 0.118$	$0.676 \pm 0.118$	$1.317 \pm 0.337$
Jet $p_T$ Reweighting	$0.489 \pm 0.046$	$0.151 \pm 0.031$	$0.257 \pm 0.046$	$0.419 \pm 0.071$	$0.568 \pm 0.117$	$0.705 \pm 0.115$	$1.363 \pm 0.342$
	$0.328 \pm 0.068$	$0.124 \pm 0.048$	$0.297 \pm 0.100$	$0.234 \pm 0.061$	$0.680 \pm 0.092$	$0.452 \pm 0.138$	$2.385 \pm 1.729$

(c) Fake factor for forward electrons ( $1.37 < |\eta|$ ).Table 5.14: Values of the fake factor in each  $p_T$  bin and for each individual systematic source.

	estimated yield	$f_e$ stat. up	$f_e$ stat. dn	$f_e$ syst. up	$f_e$ syst. dn	$f_\mu$ stat. up	$f_\mu$ stat. dn	$f_\mu$ syst. up	$f_\mu$ syst. dn
$e^\pm e^\pm$	$11.42 \pm 3.13$	—	—	—	—	—	—	—	—
$\mu^\pm \mu^\pm$	$4.82 \pm 0.77$	—	—	—	—	$0.65$	$-0.65$	$3.64$	$-0.61$
$\mu^\pm e^\pm$	$37.08 \pm 5.16$	$4.90$	$-4.90$	$5.59$	$-14.34$	$1.39$	$-1.39$	$16.10$	$-1.98$

Table 5.15: Estimated yields for the fake lepton background. The estimated yield is shown in the first column together with the statistical uncertainty followed by the systematic uncertainties from variations of the the fake factors within their statistical (stat.) and systematic (syst.) uncertainties. The labels  $f_e$  and  $f_\mu$  indicate the fake factors for electrons and muons, respectively.

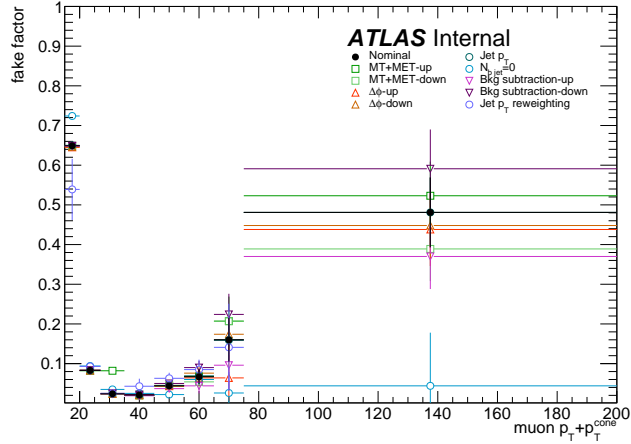


Figure 5.20: Systematic variations in the fake factor as a function of muon  $p_T + p_T^{\text{cone}}$ . The individual fake factors obtained for each systematic variation are displayed with their statistical uncertainties.

#### 1500 5.3.4.6 Validation of the fake factor

1501 The accuracy of the fake factor method is tested in several validation regions, the most sensitive  
 1502 of which is the same-sign top fakes VR (SS top VR), defined in Table 5.16. This region inverts  
 1503 the signal region's  $b$ -jet veto to accept events with exactly one  $b$ -jet. Due to this requirement, the  
 1504 dominant source of events comes from the  $t\bar{t}$  process where a  $b$ -jet fakes an isolated lepton. The  
 1505 distribution of the subleading lepton  $p_T$  in this VR is shown in Figure 5.22 for all lepton flavor  
 1506 combinations. There is good agreement between the data and the prediction, even when only taking  
 1507 into account the statistical uncertainty and not the large systematic uncertainties assigned to the  
 1508 fake estimation.

Same-sign inclusive VR
Exactly 2 same-sign signal leptons
$p_T > 27$ GeV for both leptons
$m_{ll} > 20$ GeV
$ m_{ee} - m_Z  > 15$ GeV ( $e^\pm e^\pm$ -channel only)
$N_{b\text{-jet}} = 1$
$N_{\text{jet}} \geq 2$
Leading jet $p_T > 65$ GeV
Subleading jet $p_T > 35$ GeV

Table 5.16: Selection criteria for the same-sign top fakes validation region.

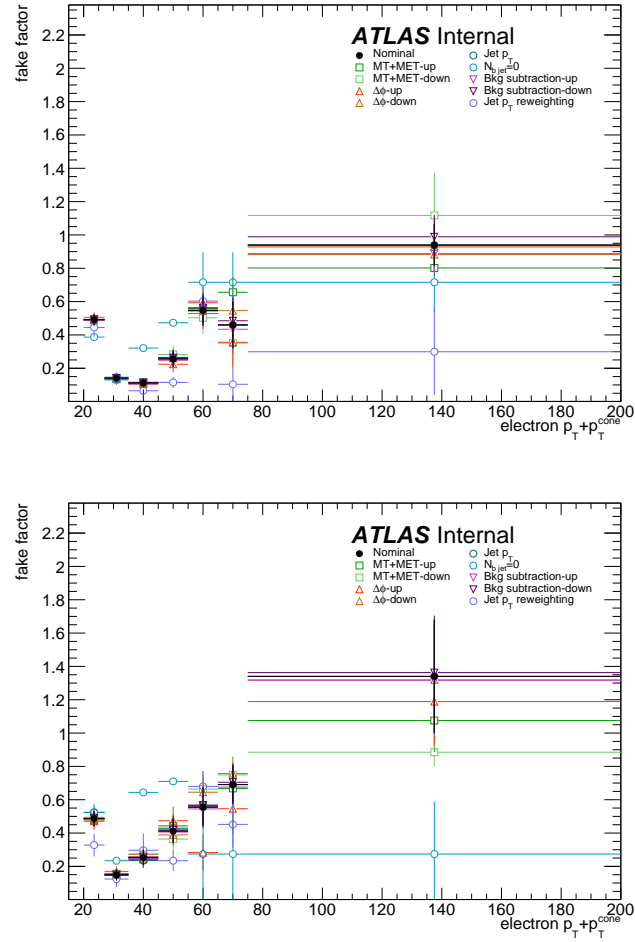


Figure 5.21: Systematic variations in the fake factor as a function of electron  $p_T + p_T^{\text{cone}}$  in the central ( $|\eta| < 1.37$ , top) and forward ( $|\eta| > 1.37$ , bottom) regions of the detector. The individual fake factors obtained for each systematic variation are displayed with their statistical uncertainties.

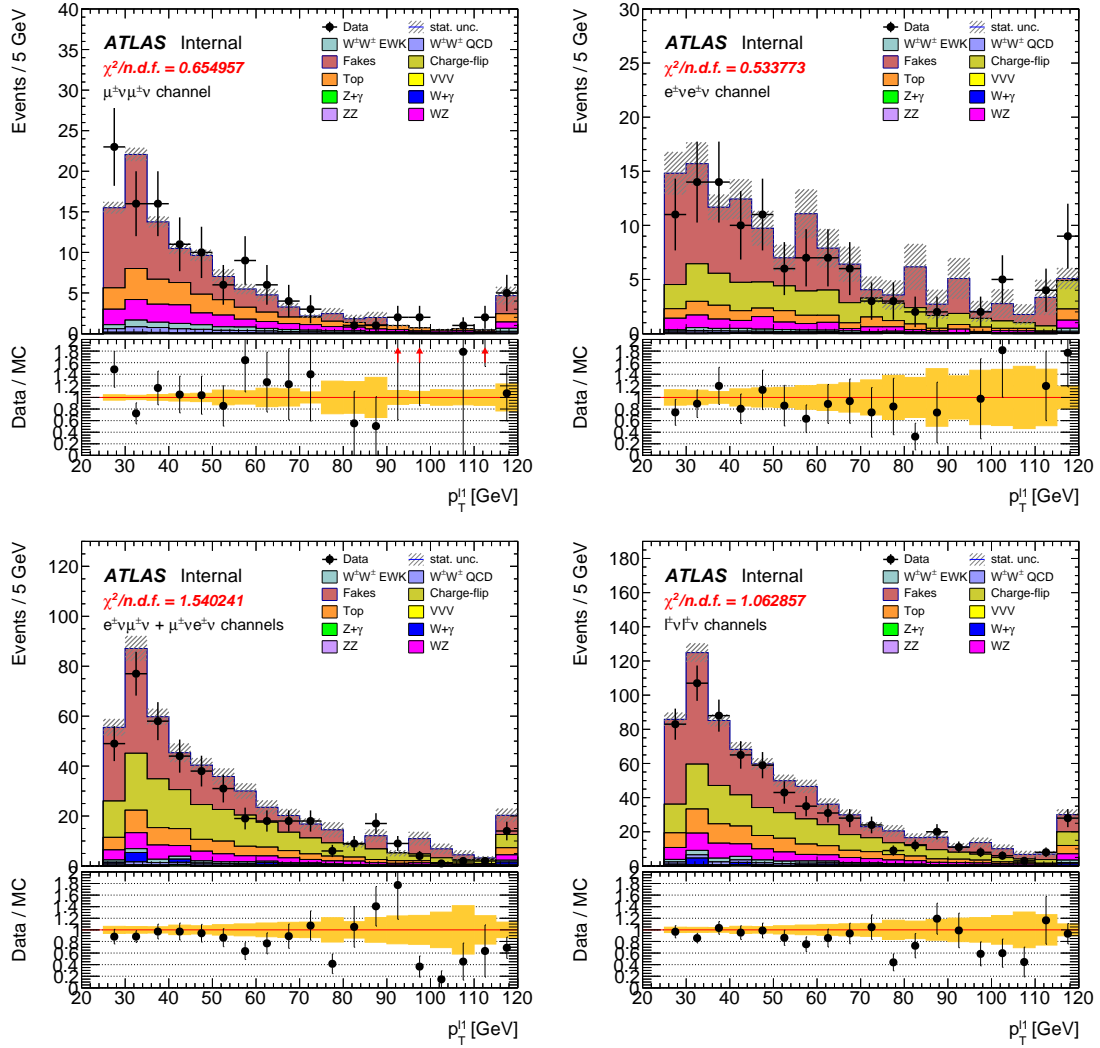


Figure 5.22: Distributions of the subleading lepton  $p_T$  in the same-sign top fakes VR for  $\mu^\pm\mu^\pm$  events (top right),  $e^\pm e^\pm$  events (top left),  $\mu^\pm e^\pm$  events (bottom left), and all events combined (bottom right). All errors are statistical only.

1509 **5.3.5 Reduction of  $WZ$  background using custom overlap removal**

1510 The dominant source of prompt background in this analysis comes from  $WZ$  events where both  
 1511 bosons decay leptonically. Traditionally, the background is dealt with by imposing a veto on any  
 1512 event with a third lepton passing some loose identification criteria (the so-called *trilepton veto*). In  
 1513 the case of this analysis, if one or more leptons (in addition to the two signal leptons) passed the  
 1514 preselection criteria, the event would be rejected. However,  $WZ$  events can still enter the signal  
 1515 region if one of the leptons fails the veto selection or falls outside of the detector’s acceptance.

1516 In order to understand the sources of  $WZ$  events that are not removed by the trilepton veto,  
 1517 a study was performed on truth-level leptons<sup>16</sup> on  $W^\pm W^\pm jj$  and  $WZ$  MC samples. Events with  
 1518 three truth leptons were selected, and each was matched to its reconstruction-level partner by finding  
 1519 the closest  $\Delta R(\text{truth}, \text{reco})$  and  $\Delta p_{\text{T},\text{truth},\text{reco}}$  match. For events surviving the trilepton veto, the  
 1520 two signal leptons were removed, and the remaining leptons represent real leptons that failed to  
 1521 be selected for the veto. Between 40-50% of these leptons fell outside of the eta acceptance of the  
 1522 analysis (see Figure 5.23) and were unrecoverable. The second largest source of leptons failing the  
 1523 preselection was the OR, defined in Section 5.2.1.4. The standard OR procedure appeared to be  
 1524 too aggressive in removing leptons in favor of jets, causing many three lepton events to “lose” their  
 1525 third lepton and pass the trilepton veto. Therefore a *Custom OR* was investigated which would  
 1526 replace the standard OR in the preselection and allow for better  $WZ$  rejection by removing fewer  
 1527 third leptons.

1528 **TODO:** Mention how the extra leptons in the  $W^\pm W^\pm jj$  are background leptons since there are  
 1529 only 2 from the main decay

1530 In order to construct a “custom” OR, a new quantity is defined between a lepton ( $l$ ) and a nearby  
 1531 jet ( $j$ )

$$p_{\text{T},\text{ratio}}(l, j) = \frac{p_{\text{T}l}}{p_{\text{T}j}} \quad (5.13)$$

1532 which, along with  $\Delta R(l, j)$ , will allow for more third leptons to pass the preselection. The idea  
 1533 behind including  $p_{\text{T},\text{ratio}}$  is to be able to preferentially remove background leptons originating from  
 1534 jets (i.e. those that carry a low percentage of the total jet momentum) instead of removing *any*  
 1535 lepton near to jet. The distributions of  $p_{\text{T},\text{ratio}}$  and the associated efficiency curves for muons and  
 1536 electrons can be found in Figures 5.24 and 5.26, respectively, and the distributions for  $\Delta R(\mu, j)$  for

---

<sup>16</sup>Truth particles are the particles produced directly by the MC generator before being passed through the full detector simulation, at which point they are considered *reconstruction-level* (or *reco-level*) particles.

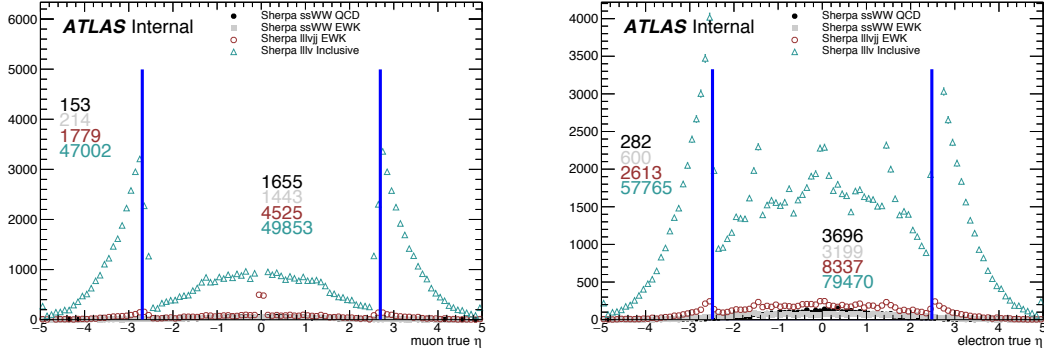


Figure 5.23: Pseudorapidity ( $\eta$ ) distributions of truth muons (top) and electrons (bottom) for Sherpa  $W^\pm W^\pm jj$  and  $WZ$  MC samples. The blue vertical lines represent the allowed  $\eta$  range for each lepton flavor. The numbers correspond to the number of raw MC events that fall within and outside of the allowed  $\eta$  range for each MC sample.

1537 muons can be found in Figure 5.25. Since all electrons have an associated jet in the calorimeters,  
1538 the  $\Delta R(e, j)$  variable is not a good quantity to use for this custom OR.

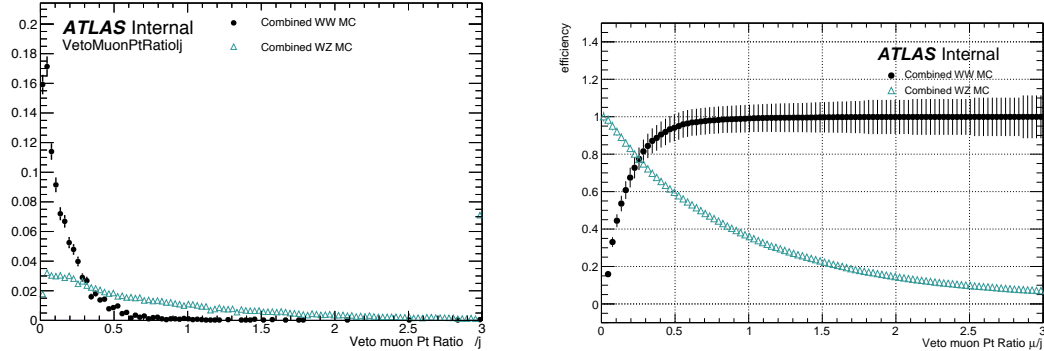


Figure 5.24: Distributions of  $p_{T,\text{ratio}}(\mu, j)$  for EWK and QCD  $W^\pm W^\pm jj$  signal (black) and  $WZ$  background (teal) for truth-matched third muons in events that pass the trilepton veto. Both distributions are normalized to unit area. The associated efficiency curves are on the right where efficiency is defined as the percentage of total events that would pass a cut on  $p_{T,\text{ratio}}(\mu, j)$  at a given value on the  $x$ -axis.

1539 A workingpoint for the Custom OR was chosen by requiring 90% signal retention for muons  
1540 and 90% background rejection for electrons. The cut on electrons was allowed to be much tighter  
1541 because the number of signal events with a third electron is considerably smaller than for muons.  
1542 It should be re-emphasized the signal events that are present in Figures 5.24–5.26 do not represent  
1543 the full set of signal events, but only those with a real third lepton (which must come from some

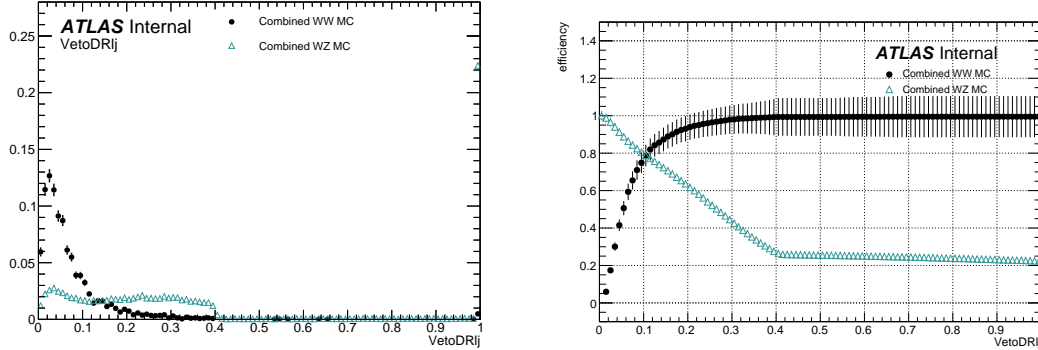


Figure 5.25: Distributions of  $\Delta R(\mu, j)$  for EWK and QCD  $W^\pm W^\pm jj$  signal (black) and  $WZ$  background (teal) for truth-matched third muons in events that pass the trilepton veto. Both distributions are normalized to unit area. The associated efficiency curves are on the right where efficiency is defined as the percentage of total events that would pass a cut on  $\Delta R(\mu, j)$  at a given value on the  $x$ -axis.

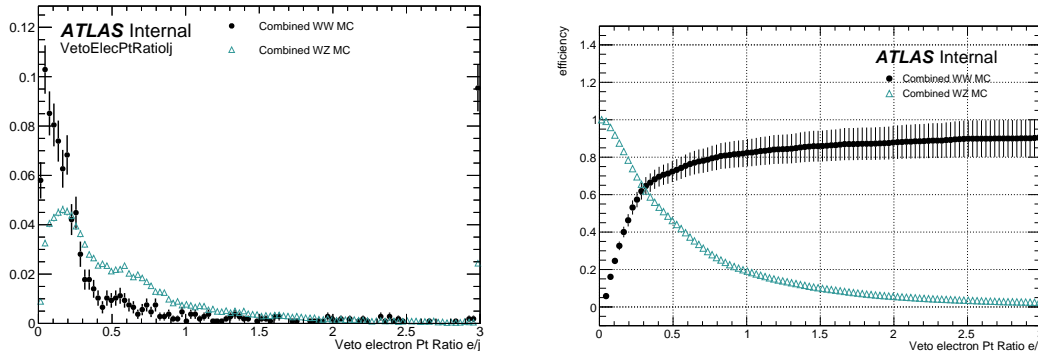


Figure 5.26: Distributions of  $p_{T,\text{ratio}}(e, j)$  for EWK and QCD  $W^\pm W^\pm jj$  signal (black) and  $WZ$  background (teal) for truth-matched third electrons in events that pass the trilepton veto. Both distributions are normalized to unit area. The associated efficiency curves are on the right where efficiency is defined as the percentage of total events that would pass a cut on  $p_{T,\text{ratio}}(e, j)$  at a given value on the  $x$ -axis.

source other than the signal  $W^\pm W^\pm jj$  process). For muons, an or of  $p_{T,\text{ratio}}(\mu, j)$  and  $\Delta R(\mu, j)$  is used to maximize the third lepton acceptance due to correlations between the quantities, as shown in Figure 5.27; for electrons, only a cut on  $p_{T,\text{ratio}}(e, j)$  is used. The Custom OR workingpoint is outlined in Table 5.17.

Custom OR Definition	
Muons	$p_{T,\text{ratio}}(\mu, j) > 0.40$ or $\Delta R(\mu, j) > 0.15$
Electrons	$p_{T,\text{ratio}}(e, j) > 0.18$

Table 5.17: Custom OR definition. Leptons must pass this selection in order to be counted for the trilepton veto.

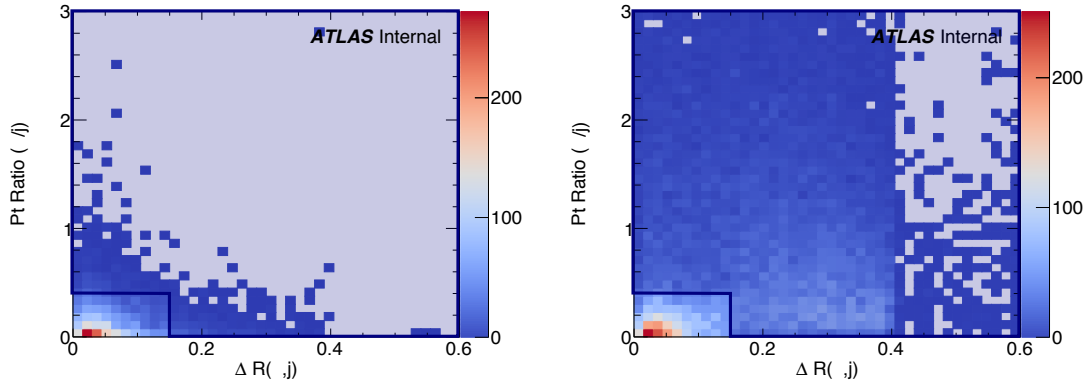


Figure 5.27: Two-dimensional plots of  $p_{T,\text{ratio}}(\mu, j)$  vs  $\Delta R(\mu, j)$  for truth-matched third muons in events that pass the trilepton veto for EWK and QCD  $W^\pm W^\pm jj$  signal (left) and  $WZ$  background (right). The blue overlay indicates the area in which the third leptons will pass the custom OR and result in the event failing the trilepton veto.

Tests of the performance of the Custom OR yield promising results, with approximately 20% reduction in  $WZ$  background compared to less than 2% signal loss in the signal region. Unfortunately, due to differences between the primary analysis framework and the one used for testing, in practice the gains in  $WZ$  rejection are not nearly as substantial, and ultimately the Custom OR is not included in the final analysis. However, it is still a potentially useful tool for improving background rejection via lepton number vetoes in analyses with overly aggressive OR procedures.

#### 5.4 Cross section measurement

The  $W^\pm W^\pm jj$  EWK cross section is extracted from the signal region using a maximum-likelihood fit applied simultaneously to four  $m_{jj}$  bins in the signal region as well as to the low- $m_{jj}$  and  $WZ$

control regions. For the fit and cross section extraction, the signal region is defined as in Table 5.8 with the dijet invariant mass requirement raised to  $m_{jj} > 500$  GeV. The low- $m_{jj}$  region is defined to mirror the signal region exactly with the dijet invariant mass inverted to  $200 < m_{jj} < 500$  GeV, and the  $WZ$  control region is defined previously in Section 5.3.1.

The signal and low- $m_{jj}$  regions are split into six channels based on the flavor and charge of the dilepton pair:  $\mu^+\mu^+$ ,  $\mu^-\mu^-$ ,  $\mu^+e^+$ ,  $\mu^-e^-$ ,  $e^+e^+$ , and  $e^-e^-$ . This split by charge increases the sensitivity of the measurement due to the  $W^+/W^-$  charge asymmetry at hadron colliders favoring the production of  $W^+$  bosons [79]. Since the signal events contain two  $W$  bosons, the signal strength compared to charge-symmetric backgrounds is much greater in the  $++$  channels for both charges combined. The  $WZ$  control region is included in the fit as a single bin ( $l^\pm l^\pm l^\pm$ ).

The maximum likelihood fit and cross section extractions are outlined in Sections 5.4.1 and 5.4.3, respectively. The results of the cross section measurement and of the analysis as a whole are presented in Section 5.6.

#### 5.4.1 Maximum likelihood fit

**TODO:** This section is very similar to what is written in the support note... May need to put some work into flushing it out so it's not so close to copy-paste The number of predicted signal events in each channel  $c$  and  $m_{jj}$  bin  $b$  can be calculated from the SM predicted signal cross section  $\sigma_{\text{theo}}^{\text{tot}}$ , the total integrated luminosity  $\mathcal{L}$ , the signal acceptance  $\mathcal{A}$ , and the efficiency corrections  $\mathcal{C}(\theta)$ , where  $\theta$  represents the set of nuisance parameters that parameterize the effects of each systematic uncertainty on the signal and background expectations. The acceptance and efficiency corrections will be covered in more detail in Section 5.4.2.

$$N_{cb}^{\text{sig}}(\theta) = \sigma_{\text{theo}}^{\text{tot}} \mathcal{A}_b \mathcal{C}_b(\theta) \mathcal{L} \quad (5.14)$$

A signal strength parameter  $\mu$  is defined as the ratio of the measured cross section to the SM predicted cross section. The expected number of events in a given channel and bin can then be expressed as the sum of the estimated background ( $N_{cb}^{\text{bkg}}(\theta)$ ) and the number of predicted signal events scaled by  $\mu$ :

$$\begin{aligned} N_{cb}^{\text{exp}}(\theta) &= \mu N_{cb}^{\text{sig}}(\theta) + N_{cb}^{\text{bkg}}(\theta) \\ &= \mu \sigma_{\text{theo}}^{\text{tot}} \mathcal{A}_b \mathcal{C}_b(\theta) \mathcal{L} + N_{cb}^{\text{bkg}}(\theta) \end{aligned} \quad (5.15)$$

The nuisance parameters are constrained by Gaussian probability distribution functions, and the normalization of the  $WZ$  background mentioned in Section 5.3.1 is included in the fit as a free

1584 parameter. The expected yields for signal and background processes are adjusted by the set of  
 1585 nuisance parameters within the constraints of the systematic uncertainties. The yields after the fit  
 1586 correspond to the value that best matches the observed data.

1587 The number of events per channel and bin after the fit can be written as a sum of the predicted  
 1588 event yields for each sample  $s$ :

$$\nu_{cb}(\phi, \theta, \gamma_{cb}) = \gamma_{cb} \sum_s [\eta_{cs}(\theta) \phi_{cs}(\theta) \lambda] h_{cbs}(\theta) \quad (5.16)$$

1589 In this equation, the fitted number of events in a given channel and bin is obtained by weighting  
 1590 the histogram of predicted yields  $h_{cbs}$  by the product of a given luminosity  $\lambda$  and any normalization  
 1591 factors  $\phi_{cs}$  that may be given for each channel and sample. The input histogram and the normaliza-  
 1592 tion factors may depend on the nuisance parameters  $\theta$  taking into account sources of systematic  
 1593 uncertainty. Uncertainties on the normalization factors  $\eta_{cs}(\theta)$  are also included. Finally, bin-by-bin  
 1594 scale factors  $\gamma_{cb}$  are included to parameterize the statistical uncertainties of the MC predictions.

1595 The binned likelihood function is given by a product of Gaussian functions for the luminosity  
 1596 and for the background uncertainties and a product of Poisson functions for the number of observed  
 1597 events in each bin and channel:

$$L(\mu|\theta) = \mathcal{G}(\mathcal{L}|\theta_{\mathcal{L}}, \sigma_{\mathcal{L}}) \cdot \prod_c \prod_b \mathcal{P}(N_{cb}^{\text{meas.}} | \nu_{cb}(\mu)) \prod_p \mathcal{G}(\theta_p^0 | \theta_p) \quad (5.17)$$

1598 where  $\mathcal{G}$  and  $\mathcal{P}$  are the Gaussian and Poisson functions, respectively. As before,  $\mathcal{L}$  represents the  
 1599 integrated luminosity with uncertainty  $\sigma_{\mathcal{L}}$  and associated nuisance parameter  $\theta_{\mathcal{L}}$ . The number of  
 1600 measured events in a given bin and channel is represented by  $N_{cb}^{\text{meas.}}$ , and  $\nu_{cb}(\mu)$  is the predicted  
 1601 number of events defined in Equation 5.16 expressed as a function of the signal strength  $\mu$ . Finally,  
 1602 the set of nuisance parameters  $\theta$  and any auxiliary measurements used to constrain them  $\theta^0$  are  
 1603 multiplied for each parameter  $p$ .

1604 The profile likelihood ratio is defined as

$$q_{\mu} = -2 \ln \frac{L(\mu, \hat{\theta}_{\mu})}{L(\hat{\mu}, \hat{\theta})} \quad (5.18)$$

1605 with  $\hat{\mu}$  and  $\hat{\theta}$  as the unconditional maximum likelihood estimates and  $\hat{\theta}$  as the conditional maximum  
 1606 likelihood estimate for a given value of  $\mu$ . The fitted signal strength  $\hat{\mu}$  is obtained by maximizing  
 1607 the likelihood function with respect to all parameters. The compatibility of the observed data  
 1608 with the background-only hypothesis can then be calculated by setting  $\mu = 0$ . Observation of the  
 1609  $W^{\pm}W^{\pm}jj$  EWK process is claimed if the data is found to be inconsistent with the background-only  
 1610 hypothesis by more than  $5\sigma$ .

1611 **5.4.2 Definition of the fiducial volume**

1612 Before extracting the cross section, it is necessary to define the fiducial volume, or the phase space  
 1613 of measurable events. It is a subset of the total phase space defined by selection requirements  
 1614 designed to mirror those applied in the analysis as closely as possible. The selection criteria for the  
 1615 fiducial volume are listed in Table 5.18.

Fiducial region selection	
Lepton selection	Two prompt leptons ( $e, \mu$ ) $p_T > 27$ GeV and $ \eta  < 2.5$ for both leptons Both leptons with the same electric charge Dilepton invariant mass $m_{ll} > 20$ GeV Dilepton separation $\Delta R(ll) > 0.3$
Missing transverse energy	Two neutrino system with $p_T^{\nu\nu} > 30$ GeV
Jet selection	At least two jets Leading jet $p_T > 65$ GeV Subleading jet $p_T > 35$ GeV Leading and subleading jet $ \eta  < 4.5$ Jet-lepton separation $\Delta R(l, j) > 0.3$ Dijet invariant mass $m_{jj} > 500$ GeV Dijet separation $\Delta y_{jj} > 2.0$

Table 5.18: Definition of the fiducial volume.

1616 In MC simulations, the total phase space is generated, providing the total theoretical cross section  
 1617  $\sigma_{\text{theo}}^{\text{tot}}$  and the total number of signal events  $\mathcal{N}_{\text{sig}}^{\text{tot}}$ <sup>17</sup>. After applying the fiducial selection at truth  
 1618 level, the total number of signal events in the fiducial region  $\mathcal{N}_{\text{sig}}^{\text{fid}}$  is obtained. An acceptance factor  
 1619  $\mathcal{A}$  is used to represent the efficiency of events falling in the fiducial region at truth level:

$$\mathcal{A} = \frac{\mathcal{N}_{\text{sig}}^{\text{fid}}}{\mathcal{N}_{\text{sig}}^{\text{tot}}} \quad (5.19)$$

1620 A correction factor  $\mathcal{C}$  is also necessary to translate from the truth level fiducial volume to the  
 1621 reconstruction level signal region and is defined in terms of the number of reconstruction level MC  
 1622 events in the signal region  $N_{\text{sig}, \text{MC}}^{\text{SR}}$ :

$$\mathcal{C} = \frac{N_{\text{sig}, \text{MC}}^{\text{SR}}}{\mathcal{N}_{\text{sig}}^{\text{fid}}} \quad (5.20)$$

1623 Since the fit is binned in  $m_{jj}$ , the acceptance and efficiency correction factors need to be as well.  
 1624 Therefore,  $\mathcal{A}_i$  and  $\mathcal{C}_{ij}$  are written in terms of truth  $m_{jj}$  bins  $i$  and reconstruction  $m_{jj}$  bins  $j$ . A  
 1625 graphical representation of these regions and the use of the acceptance and correction factors can  
 1626 be seen in Figure 5.28.

<sup>17</sup>For the purpose of clarity, the number of events at truth level is represented by a script  $\mathcal{N}$ , and the number of events at reconstruction level uses a regular  $N$ .

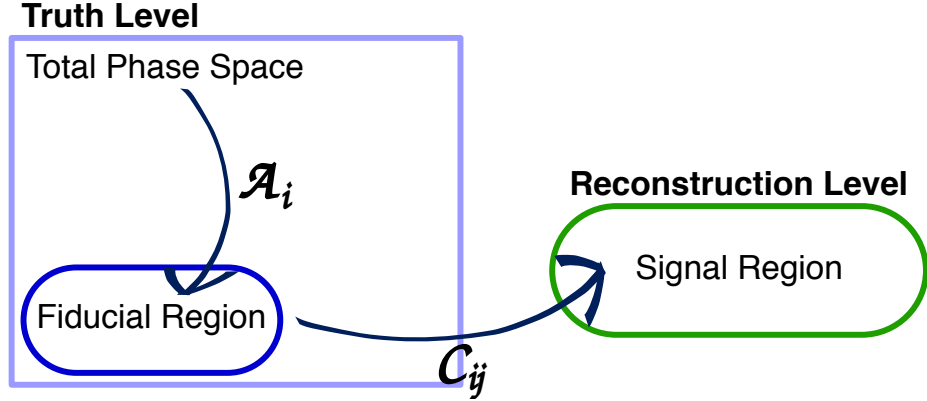


Figure 5.28: Visual representation of the different kinematic regions relevant to the cross section measurement. The acceptance factor  $\mathcal{A}$  converts from the truth level total phase space to the truth level fiducial region, and the efficiency correction  $\mathcal{C}$  translates the fiducial region in to the reconstruction level signal region.

#### 1627 5.4.3 Cross section extraction

1628 The  $W^\pm W^\pm jj$  EWK fiducial cross section is measured using the signal strength parameter  $\mu$  that is  
 1629 determined by the maximum likelihood fit. This parameter is dependent on the nuisance parameters  
 1630  $\theta$  and can be written explicitly in terms of the measured and theoretical cross sections as:

$$\mu(\theta) = \frac{\sigma_{\text{meas}}^{\text{SR}}}{\sigma_{\text{theo}}^{\text{SR}}} \quad (5.21)$$

1631 In the simple case with only one bin, the equation for the total number of expected events in the  
 1632 signal region first introduced in Equation 5.15 can be written as:

$$N_{\text{exp}}^{\text{SR}}(\theta) = \mu(\theta) \cdot \sigma_{\text{theo}}^{\text{tot}} \cdot \mathcal{L} \cdot \mathcal{A} \cdot \mathcal{C}(\theta) + N_{\text{bkg}}^{\text{SR}}(\theta) \quad (5.22)$$

1633 with the non-binned versions of  $\mathcal{A}$  and  $\mathcal{C}$  defined in Equations 5.19 and 5.20, respectively.

1634 If the measured fiducial cross section is written as:

$$\sigma_{\text{meas}}^{\text{fid}} = \mu \cdot \mathcal{A} \cdot \sigma_{\text{theo}}^{\text{tot}} \quad (5.23)$$

1635 then Equation 5.22 can be rearranged to read:

$$\sigma_{\text{meas}}^{\text{fid}} = \frac{N_{\text{exp}}^{\text{SR}}(\theta) - N_{\text{bkg}}^{\text{SR}}(\theta)}{\mathcal{L} \cdot \mathcal{C}(\theta)} \quad (5.24)$$

1636 The measured fiducial cross section can finally be rewritten in terms of  $\hat{\mu}$ , which is the best estimator  
 1637 of the signal strength as extracted from the fit:

$$\begin{aligned} \sigma_{\text{meas}}^{\text{fid}} &= \hat{\mu}(\theta) \cdot \sigma_{\text{theo}}^{\text{tot}} \cdot \mathcal{A} \\ &= \hat{\mu}(\theta) \cdot \sigma_{\text{theo}}^{\text{fid}} \end{aligned} \quad (5.25)$$

1638 In practice, however, the cross section is not extracted from a single bin, and Equation 5.22  
 1639 becomes for a single channel in truth and reconstruction level  $m_{jj}$  bins  $i$  and  $j$ , respectively:

$$N_{\text{exp}}^{\text{SR}}(\theta) = \mu(\theta) \cdot \sigma_{\text{theo}}^{\text{tot}} \cdot \mathcal{L} \cdot \sum_i \mathcal{A}_i \cdot \sum_j \mathcal{C}_{ij} + \sum_j N_{\text{bkg},j}^{\text{SR}}(\theta) \quad (5.26)$$

1640 where now the binned versions of  $\mathcal{A}_i$  and  $\mathcal{C}_{ij}$  are used. This equation can be extended to include all  
 1641 the analysis channels by increasing the number of bins  $i$  and  $j$ . Additionally, it can be shown that  
 1642 Equation 5.25 holds for this more complex case as well [46], provided care is taken to ensure that  
 1643 all the uncertainties are handled properly.

## 1644 5.5 Summary of uncertainties

1645 Systematic uncertainties enter the final fit as nuisance parameters which can impact the estimated  
 1646 signal and background yields and the shapes of the  $m_{jj}$  distributions. These uncertainties can arise  
 1647 from the experimental methods or from the theoretical calculations used in the analysis. This section  
 1648 summarizes the systematic uncertainties; the experimental uncertainties are detailed in Section 5.5.1,  
 1649 and the theoretical uncertainties are covered in Section 5.5.2. The impacts of the systematic uncer-  
 1650 tainties on the final cross section measurement are summarized in Table 5.19.

Source	Impact [%]
Reconstruction	$\pm 4.0$
Electrons	$\pm 0.5$
Muons	$\pm 1.2$
Jets and $E_{\text{T}}^{\text{miss}}$	$\pm 2.8$
$b$ -tagging	$\pm 2.0$
Pileup	$\pm 1.5$
Background	$\pm 5.0$
Misid. leptons	$\pm 3.9$
Charge misrec.	$\pm 0.3$
$WZ$	$\pm 1.3$
$W^\pm W^\pm jj$ QCD	$\pm 2.8$
Other	$\pm 0.8$
Signal	$\pm 3.6$
Interference	$\pm 1.0$
EW Corrections	$\pm 1.3$
Shower, Scale, PDF & $\alpha_s$	$\pm 3.2$
Total	$\pm 7.4$

Table 5.19: Impact of various systematic effects on the fiducial cross section measurement. The impact of a given source of uncertainty is computed by performing the fit with the corresponding nuisance parameter varied up or down by one standard deviation from its nominal value.

---

### 1651 5.5.1 Experimental uncertainties

1652 Experimental uncertainties include detector effects as well as uncertainties on the background es-  
 1653 timation methods. Sources of systematic uncertainty on the measurement of physics objects are  
 1654 listed in Table 5.20, grouped by the relevant object type. For backgrounds estimated from MC  
 1655 simulations, variations in these sources of uncertainty are propagated through the analysis to obtain  
 1656 the corresponding uncertainties on the event yields. Additional experimental uncertainties include  
 1657 the integrated luminosity, the photon conversion rate from Section 5.3.2, and the data driven charge  
 1658 misidentification and fake lepton background estimations from Sections 5.3.3 and 5.3.4.5, respec-  
 1659 tively.

1660 The largest sources of experimental uncertainty on the MC estimations come from the jet-related  
 1661 uncertainties and the  $b$ -tagging efficiency, while the largest uncertainty on the background estimation  
 1662 comes from the fake factor. The effects of the uncertainties on the  $W^\pm W^\pm jj$  EWK signal and the  
 1663 dominant MC estimated background,  $WZ$ , are listed in Tables 5.21 and 5.22, respectively. Since  
 1664 the overall contributions from other processes estimated with MC are small, the uncertainties on  
 1665 these backgrounds have a lesser impact on the final measurement; these tables can be found in  
 1666 Appendix B.1.

Experimental uncertainties	
Electrons	Energy resolution
	Energy scale
	Identification efficiency
	Isolation efficiency
	Reconstruction efficiency
	Trigger efficiency
Muons	Energy scale
	Identification efficiency
	Inner detector track resolution
	Muon spectrometer resolution
	Trigger efficiency
$E_T^{\text{miss}}$	Resolution
	Scale
Jets	Energy resolution
	Energy scale
	JVT cut efficiency
	$b$ -tagging efficiency
Jets from pileup	

Table 5.20: List of sources of experimental uncertainties on the reconstruction of physics objects.

$W^\pm W^\pm jj$ EWK	$e^\pm e^\pm$ % Yield	$\mu^\pm e^\pm$ % Yield	$\mu^\pm \mu^\pm$ % Yield
Jet-related Uncertainties	2.28	2.22	2.28
b-tagging efficiency	1.81	1.76	1.74
Pile-up	0.48	0.97	2.42
Trigger efficiency	0.02	0.08	0.47
Lepton reconstruction/ID	1.45	1.14	1.83
MET reconstruction	0.26	0.17	0.21

Table 5.21: Impact of experimental uncertainties for the  $W^\pm W^\pm jj$  EWK processes in all channels.

$WZ$	$e^\pm e^\pm$ % Yield	$\mu^\pm e^\pm$ % Yield	$\mu^\pm \mu^\pm$ % Yield
Jet-related Uncertainties	9.58	5.03	8.45
b-tagging efficiency	2.49	2.23	2.40
Pile-up	2.99	3.49	3.33
Trigger efficiency	0.03	0.09	0.43
Lepton reconstruction/ID	1.52	1.24	3.07
MET reconstruction	0.93	0.79	1.63

Table 5.22: Impact of experimental uncertainties for the  $WZ$  process in all channels.

### 1667 5.5.2 Theoretical uncertainties

1668 It is also necessary to consider uncertainties on the theoretical predictions in the fiducial region. They  
 1669 include the choice of PDF set, the value of the strong coupling constant  $\alpha_s$ , the renormalization  
 1670 scale  $\mu_R$ , the factorization scale  $\mu_F$ , and the parton showering. The size of these uncertainties are  
 1671 measured by generating new samples with variations in a chosen parameters and comparing them  
 1672 to samples using the nominal choice of the parameter. Internal variations on the PDF sets or using  
 1673 a different set entirely results in a relative uncertainty of up to 2.25% on the nominal sample. The  
 1674 impact from varying  $\alpha_s$  is very small, on the order of < 0.01%. The factorization and renormalization  
 1675 scales are independently varied between 0.5-2.0 from their nominal values of 1.0. This results in  
 1676 relative uncertainties on the prediction of up to 15%. Finally, varying the parameters in the parton  
 1677 showering results in up to 8% uncertainty.

#### 1678 5.5.2.1 Uncertainties from EWK-QCD interference

1679 As mentioned in Section 5.0.2,  $W^\pm W^\pm jj$  production consists of both EWK processes. The two  
 1680 production modes cannot be naively separated due to cross terms in the matrix element calculation.  
 1681 These cross terms are referred to as *interference* terms. Since the  $W^\pm W^\pm jj$  EWK production is  
 1682 the focus of the analysis, and the signal region is designed to preferentially select those events, it is  
 1683 important to measure the size of the EWK-QCD interference contributions.

1684     The interference effects are estimated using the `MadGraph` MC generator, as it has a feature that  
 1685     allows direct modelling of the interference term. This allows four samples to be generated:

- 1686     1. Inclusive: All available diagrams are used in the matrix element calculation  
 1687     2. EWK only: Only EWK diagrams ( $\mathcal{O}(\alpha_{\text{EWK}}) = 4$ ) are used  
 1688     3. QCD only: Only QCD diagrams ( $\mathcal{O}(\alpha_s) = 2 \otimes \mathcal{O}(\alpha_{\text{EWK}}) = 2$ ) are used  
 1689     4. Interference: Only the interference terms are used

1690     A minimal set of generator level cuts, listed in Table 5.23, is applied in order to avoid biasing the  
 1691     sample towards either production mode. The cross sections for each of the four channels can be  
 1692     found in Table 5.24. The size of the interference is found to be approximately 6% of the total cross  
 1693     section and is taken as a systematic uncertainty.

Generator level cuts
$\Delta\eta_{jj} < 10$
Jet $p_{\text{T}} > 20$ GeV
$M_{jj} > 10$ GeV

Table 5.23: The set of generator level cuts used for generating the interference samples with `MadGraph`.

Sample	$\sigma$ (fb)
Inclusive	$3.646 \pm 0.0012$
EWK only	$2.132 \pm 0.0005$
QCD only	$1.371 \pm 0.0008$
Interference	$0.227 \pm 0.0002$

Table 5.24: Cross sections for each different  $W^\pm W^\pm jj$  production mode (inclusive, EWK only, QCD only, and interference only) generated using `MadGraph`. The cross sections are calculated using a minimal set of generator level cuts from events where the  $W$  decays to a muon.

## 1694     5.6 Results

1695     After running the full analysis chain, the event yields in the signal region, low- $m_{jj}$  control region,  
 1696     and  $WZ$  control region as well as associated nuisance parameters representing the uncertainties are  
 1697     passed to the maximum likelihood fit. From this fit, the normalization factor for the  $WZ$  control  
 1698     region  $\mu_{WZ}$  and the signal strength parameter in the signal region  $\mu_{\text{obs}}$  are determined, and the  
 1699     predicted yields in each input bin have been shifted according to the process detailed in Section 5.4.1.

1700 The  $WZ$  normalization factor is measured to be:

$$\mu_{WZ} = 0.88^{+0.07}_{-0.07}(\text{stat})^{+0.31}_{-0.21}(\text{theory})^{+0.22}_{-0.11}(\text{sys}) \quad (5.27)$$

1701 and is constrained primarily by the number of data events in the  $WZ$  control region. The observed  
 1702 signal strength of  $W^\pm W^\pm jj$  EWK production, defined in Equation 5.21, is extracted from the fit  
 1703 and measured with respect to the prediction of the **SHERPA v2.2.2** MC generator:

$$\mu_{\text{obs}} = 1.45^{+0.25}_{-0.24}(\text{stat})^{+0.06}_{-0.08}(\text{theory})^{+0.27}_{-0.22}(\text{sys}) \quad (5.28)$$

1704 This corresponds to a rejection of the background-only hypothesis with a significance of  $6.9\sigma$ .

1705 The observed number of data events are compared to the predicted signal and background yields  
 1706 in the signal region in Table 5.25 before applying the fit and in Table 5.26 after the fit. The  $m_{jj}$   
 1707 distributions for data and prediction are shown in Figure 5.29 after the fit, and the fitted event  
 1708 yields in the low- $m_{jj}$  and  $WZ$  control regions are shown in Figure 5.30. Additional distributions  
 1709 can be found in Appendix B.

	$e^+e^+$	$e^-e^-$	$\mu^+e^+$	$\mu^\pm e^\pm m$	$\mu^+\mu^+$	$\mu^-\mu^-$	combined
$WZ$	$1.9 \pm 0.6$	$1.3 \pm 0.4$	$14 \pm 4$	$8.9 \pm 2.6$	$5.5 \pm 1.6$	$3.6 \pm 1.1$	$35 \pm 10$
Non-prompt	$4.1 \pm 2.3$	$2.3 \pm 1.7$	$9 \pm 5$	$6 \pm 4$	$0.57 \pm 0.15$	$0.67 \pm 0.25$	$23 \pm 10$
$e/\gamma$ conversions	$1.74 \pm 0.29$	$1.8 \pm 0.4$	$6.1 \pm 1.6$	$3.7 \pm 0.8$	—	—	$13.4 \pm 2.5$
Other prompt	$0.17 \pm 0.05$	$0.14 \pm 0.04$	$0.90 \pm 0.19$	$0.60 \pm 0.14$	$0.36 \pm 0.10$	$0.19 \pm 0.05$	$2.4 \pm 0.5$
$W^\pm W^\pm jj$ QCD	$0.38 \pm 0.13$	$0.16 \pm 0.05$	$3.0 \pm 1.0$	$1.2 \pm 0.4$	$1.8 \pm 0.6$	$0.76 \pm 0.25$	$7.3 \pm 2.5$
Expected background	$8.2 \pm 2.4$	$5.7 \pm 1.8$	$33 \pm 7$	$21 \pm 5$	$8.2 \pm 1.8$	$5.3 \pm 1.2$	$81 \pm 14$
$W^\pm W^\pm jj$ EWK	$3.8 \pm 0.6$	$1.49 \pm 0.22$	$16.5 \pm 2.5$	$6.5 \pm 1.0$	$9.1 \pm 1.4$	$3.5 \pm 0.5$	$41 \pm 6$
Data	10	4	44	28	25	11	122

Table 5.25: Table of the data and prediction event yields in the signal region before the fit. Numbers are shown for the six lepton flavor and charge channels and for all channels combined. Here the  $WZ$  background yields are normalized to the data in the  $WZ$  control region. The background estimations from the fake factor are included in the “Non-prompt” category, and backgrounds from  $V\gamma$  production and electron charge misidentification are combined in the “ $e/\gamma$  conversions” category. Finally,  $ZZ$ ,  $VVV$ , and  $t\bar{t}V$  backgrounds are combined in the “Other prompt” category.

1710 The last ingredient necessary to measure the  $W^\pm W^\pm jj$  EWK cross section is the theory predicted  
 1711 cross section in the fiducial region defined in Table 5.18. **SHERPA v2.2.2** is used for the calculation,  
 1712 and the cross section in the total generator phase space is  $40.81 \pm 0.05$  fb, and the fiducial cross section  
 1713 is  $2.01 \pm 0.02$  fb. This corresponds to an acceptance factor of  $\mathcal{A} = 0.0493 \pm 0.0002$ . Uncertainties on  
 1714 the simulation are estimated using variations of the scale, parton shower, and PDF set. The final  
 1715 prediction used in the cross section measurement including uncertainties from Section 5.5.2 is:

$$\sigma_{\text{SHERPA}}^{\text{fid}} = 2.01 \pm 0.02(\text{stat})^{+0.29}_{-0.23}(\text{scale})^{+0.16}_{-0.02}(\text{parton shower})^{+0.05}_{-0.03}(\text{PDF}) \text{ fb} \quad (5.29)$$

	$e^+e^+$	$e^-e^-$	$\mu^+e^+$	$\mu^\pm e^\pm m$	$\mu^+\mu^+$	$\mu^-\mu^-$	combined
$WZ$	$1.49 \pm 0.30$	$1.10 \pm 0.26$	$11.7 \pm 1.7$	$8.0 \pm 1.3$	$5.0 \pm 0.6$	$3.5 \pm 0.6$	$31 \pm 4$
Non-prompt	$2.2 \pm 1.3$	$1.2 \pm 0.7$	$5.7 \pm 2.8$	$4.5 \pm 1.8$	$0.57 \pm 0.06$	$0.65 \pm 0.14$	$15 \pm 6$
$e/\gamma$ conversions	$1.6 \pm 0.4$	$1.6 \pm 0.5$	$6.3 \pm 1.6$	$4.3 \pm 1.1$	—	—	$13.8 \pm 2.9$
Other prompt	$0.16 \pm 0.04$	$0.14 \pm 0.04$	$0.90 \pm 0.19$	$0.63 \pm 0.13$	$0.39 \pm 0.09$	$0.22 \pm 0.05$	$2.4 \pm 0.5$
$W^\pm W^\pm jj$ QCD	$0.35 \pm 0.13$	$0.15 \pm 0.05$	$2.9 \pm 1.0$	$1.2 \pm 0.4$	$1.8 \pm 0.6$	$0.76 \pm 0.25$	$7.2 \pm 2.4$
Expected background	$5.8 \pm 1.5$	$4.1 \pm 1.1$	$27 \pm 4$	$18.7 \pm 2.6$	$7.7 \pm 0.8$	$5.1 \pm 0.6$	$69 \pm 7$
$W^\pm W^\pm jj$ EWK	$5.6 \pm 1.0$	$2.2 \pm 0.4$	$24 \pm 5$	$9.4 \pm 1.8$	$13.5 \pm 2.5$	$5.2 \pm 1.0$	$60 \pm 11$
Data	10	4	44	28	25	11	122

Table 5.26: Table of the data and prediction event yields in the signal region after the fit. Numbers are shown for the six lepton flavor and charge channels and for all channels combined. The background estimations from the fake factor are included in the “Non-prompt” category, and backgrounds from  $V\gamma$  production and electron charge misidentification are combined in the “ $e/\gamma$  conversions” category. Finally,  $ZZ$ ,  $VVV$ , and  $t\bar{t}V$  backgrounds are combined in the “Other prompt” category.

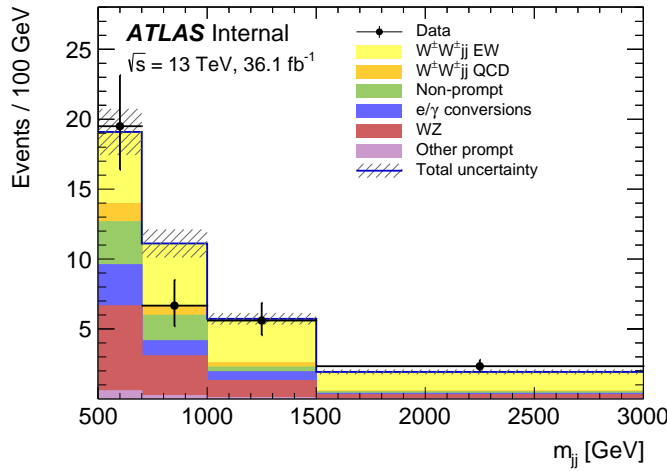


Figure 5.29: The dijet invariant mass  $m_{jj}$  distributions for data and predicted signal and background in the signal region after the fit. The shaded band represents the statistical and systematic uncertainties added in quadrature. Note that the bins have been scaled such that they represent the number of events per  $100 \text{ GeV}$  in  $m_{jj}$ . The background estimations from the fake factor are included in the “Non-prompt” category, and backgrounds from  $V\gamma$  production and electron charge misidentification are combined in the “ $e/\gamma$  conversions” category. Finally,  $ZZ$ ,  $VVV$ , and  $t\bar{t}V$  backgrounds are combined in the “Other prompt” category.

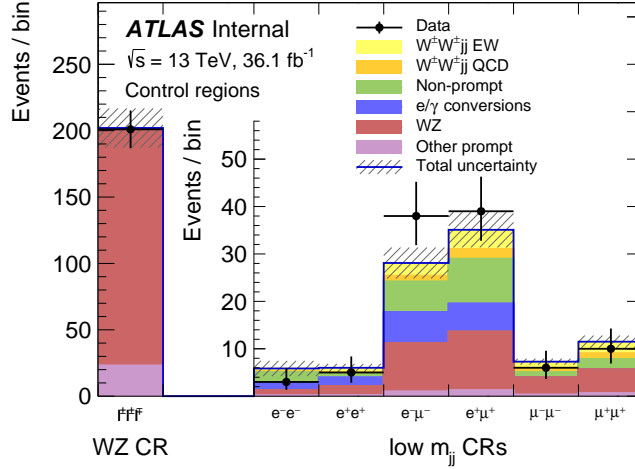


Figure 5.30: The event yields for data and predicted signal and background in the  $WZ$  and low- $m_{jj}$  control regions after the fit. The shaded band represents the statistical and systematic uncertainties added in quadrature. The background estimations from the fake factor are included in the “Non-prompt” category, and backgrounds from  $V\gamma$  production and electron charge misidentification are combined in the “ $e/\gamma$  conversions” category. Finally,  $ZZ$ ,  $VVV$ , and  $t\bar{t}V$  backgrounds are combined in the “Other prompt” category.

1716 Combining this **SHERPA** prediction with the measured signal strength  $\mu_{\text{obs}}$  from Equation 5.28,  
 1717 the measured fiducial cross section  $\sigma_{\text{meas}}^{\text{fid}}$  can be calculated using Equation 5.25:

$$\sigma_{\text{meas}}^{\text{fid}} = 2.91^{+0.51}_{-0.47}(\text{stat})^{+0.12}_{-0.16}(\text{theory})^{+0.24}_{-0.23}(\text{sys})^{+0.08}_{-0.06}(\text{luminosity}) \text{ fb} \quad (5.30)$$

1718 A plot comparing the measured fiducial cross section to two theoretical calculations is shown in  
 1719 Figure 5.31. The measured value is compared to the **SHERPA v2.2.2** prediction used to calculate  
 1720  $\mu_{\text{obs}}$  as well as to **POWHEG-BOX v2**. As mentioned in Section 5.1.1, this **POWHEG** sample does not  
 1721 include the resonant triboson diagrams and is only used here for a visual comparison.

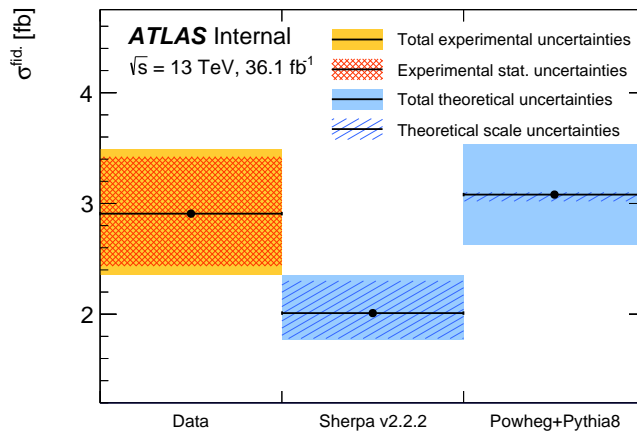


Figure 5.31: Comparison of the measured  $W^\pm W^\pm jj$  EWK fiducial cross section with theoretical calculations from **SHERPA v2.2.2** and **POWHEG-BOX v2**. The light orange band represents the total experimental uncertainty on the measured value, and the dark orange hashed band is the statistical uncertainty. For the simulations, the light blue band represents the total theoretical uncertainty, and the dark blue hashed band are the scale uncertainties. The theory predictions do not include the interference between the EWK and QCD production.

1722

## CHAPTER 6

1723

# Prospects for same-sign $WW$ at the High Luminosity LHC

1724

1725 On December 3, 2018, Run 2 of the LHC officially ended, and the collider was shut down to begin  
1726 the first of two scheduled extended maintenance periods [80]. During these two long shutdowns,  
1727 the Phase-I and Phase-II upgrades of the LHC and ATLAS will occur in order to prepare for the  
1728 High-Luminosity LHC (HL-LHC) which is scheduled to begin operation in 2026 [81].

1729 The HL-LHC is planned to run at a center-of-mass energy of  $\sqrt{s} = 14$  TeV with an instantaneous  
1730 luminosity of  $\mathcal{L} = 5 \times 10^{34}$  cm $^{-2}$ s $^{-1}$  with up to 200 collisions per beam-crossing. Over the course  
1731 of operation, the HL-LHC is expected to collect a total integrated luminosity of  $\mathcal{L} = 3000$  fb $^{-1}$  by  
1732 2035 [82]. **TODO: Compare to current LHC numbers?**

1733 These run conditions will be much harsher than what ATLAS has experienced so far, and there  
1734 are several upgrades planned for the detector to operate in the high luminosity environment. Most  
1735 notably, the entire ID will be replaced with an all-silicon tracker which will extend the coverage from  
1736  $|\eta| \leq 2.7$  up to  $|\eta| \leq 4.0$ . This will allow for reconstruction of charged particle tracks which can  
1737 in turn be matched to clusters in the calorimeters for electron identification or forward jet tagging  
1738 [83].

1739 The upgraded detector, the higher beam energy, and the increased volume of data to be collected  
1740 provides the opportunity to measure rarer processes with a much higher precision than what was  
1741 possible in Run 1. Same-sign  $W^\pm W^\pm jj$  production, is one such process. With greater statistics,  
1742 the accuracy of the cross section measurement can be improved over the 13 TeV analysis detailed in  
1743 Chapter 5, and it also will allow for more detailed physics studies, such as measuring the polarization  
1744 of the  $W$  bosons. A measurement of the longitudinal polarization of the scattered  $W$  bosons has

1745 not yet been possible, but it remains of great interest due to its sensitivity to electroweak symmetry  
 1746 breaking [84]. The analysis detailed in this chapter is based off of the 2018 ATLAS HL-LHC  
 1747  $W^\pm W^\pm jj$  prospects study [85] which is itself an extension of the 2017 ATLAS study [86]. **TODO:**  
 1748 mention CMS's study + yellow report?

### 1749 6.0.1 Analysis Overview

1750 The experimental signature of interest is identical to the 13 TeV analysis: two prompt leptons (either  
 1751 electrons or muons) with the same charge, missing transverse energy, and two high energy, forward  
 1752 jets. These jets are again required to have a large angular separation and a high combined invariant  
 1753 mass to preferentially select EWK- over QCD-produced  $W^\pm W^\pm jj$  events.

1754 Background processes are again similar to the 13 TeV analysis and are summarized again here.  
 1755 The dominant source of prompt background from  $WZ+jets$  events where both bosons decay lepton-  
 1756ically. If the lepton from the  $Z$ -decay with opposite charge from the  $W$  falls outside of the detector  
 1757 acceptance or is not identified, the remainder could appear to be a  $W^\pm W^\pm jj$  signal event. To a  
 1758 lesser extent,  $ZZ+jets$  events can enter the signal region in much the same way provided two lep-  
 1759 tons are “lost”. Other prompt sources include  $t\bar{t}+V$  and multiple parton interactions, however  
 1760 these processes do not contribute much. These prompt backgrounds are expected to contribute  
 1761 less than in Run 2 with the addition of forward tracking in the upgraded ATLAS detector. Jets  
 1762 mis-reconstructed as leptons or leptons from hadronic decays (such as  $t\bar{t}$  and  $W+jets$  production)  
 1763 comprise the non-prompt lepton background. Lastly, events with two prompt, opposite-charge elec-  
 1764 trons can appear as a same-sign event provided one of the electrons is mis-reconstructed as the  
 1765 wrong charge.

1766 In this analysis, the EWK production of  $W^\pm W^\pm jj$  is studied in the context of the planned  
 1767 HL-LHC run conditions and upgraded ATLAS detector. An optimized event selection (referred to  
 1768 as the *optimized selection*) is also explored in an effort to gain increased signal significance over  
 1769 the *default selection*. The cross section of the inclusive EWK production is measured for both the  
 1770 default and optimized selections, and the extraction of the longitudinal scattering significance is  
 1771 measured with the optimized selection.

## 1772 6.1 Theoretical motivation

1773 The theoretical motivation for studying the ssWW process—and VBS in general—is detailed in Sec-  
 1774 tion 5.0.2. Since it is specifically the scattering of *longitudinally polarized* vector bosons that violates

1775 unitarity without a SM Higgs boson, a direct measurement of this cross section will be very useful  
 1776 for understanding how the Higgs unitarizes the process [84].

### 1777 6.1.1 Experimental sensitivity to longitudinal polarization

1778 **TODO:** mention that since there are so many polarization possibilities, a large integrated luminosity  
 1779 is needed to measure just one of them individually There are three possible polarization states for  
 1780 a massive vector boson: two transverse (+ or -) and one longitudinal (0). Therefore, in a system  
 1781 with two  $W$  bosons, the overall polarization can be purely longitudinal (00), purely transverse (++,  
 1782 --, and +-), or mixed (+0 and -0). The three combinations will be referred to as  $LL$ ,  $TT$ , and  
 1783  $LT$  respectively.

1784 In order extract the longitudinal scattering component, it is necessary to find variables that  
 1785 distinguish the  $LL$  from the  $TT$  and  $LT$ . Several were studied, and those with the best discriminating  
 1786 power between the polarizations are the leading and subleading lepton  $p_T$  as well as the azimuthal  
 1787 separation ( $|\Delta\phi_{jj}|$ ) of the two VBS jets. The  $LL$  events prefer lower  $p_T$  for both signal leptons  
 1788 (see Figure 6.1), which motivates keeping cuts on these quantities as low as possible in the event  
 1789 selection. In the case of  $|\Delta\phi_{jj}|$ , the  $LL$  events generally had a larger dijet separation (see Figure 6.2),  
 1790 and this variable is used in a binned likelihood fit to extract the longitudinal scattering significance.

## 1791 6.2 Monte Carlo samples

1792 As no real HL-LHC data will be available for many years, all signal and background processes  
 1793 are modeled using MC simulations generated at  $\sqrt{s} = 14$  TeV, with the event yields scaled to the  
 1794 anticipated HL-LHC integrated luminosity of  $\mathcal{L} = 3000 \text{ fb}^{-1}$ . The MC samples used in the analysis  
 1795 are generated at particle-level and have not been run through the typical full simulation of the  
 1796 ATLAS detector. Instead, smearing functions derived from a **GEANT4** simulation of the upgraded  
 1797 ATLAS detector are used to estimate detector effects such as momentum resolution. In addition,  
 1798 pileup events are fully simulated. The MC samples used in this analysis are summarized in Table 6.1.

1799 The signal sample consists of both VBS and non-VBS electroweak (EWK)  $W^\pm W^\pm jj$  production,  
 1800 and it is simulated with the **Madgraph5\_aMC@NLO** generator using the NNPDF3.0 PDF set and in-  
 1801 terfaced with **PYTHIA v8** [87] for hadronization and parton showering. To study the longitudinal  
 1802 polarization more directly, two additional **Madgraph5\_aMC@NLO**  $W^\pm W^\pm jj$  samples are used: one  
 1803 containing only the longitudinal contribution (LL) and a second containing the transverse (TT) and  
 1804 mixed (LT) contributions.

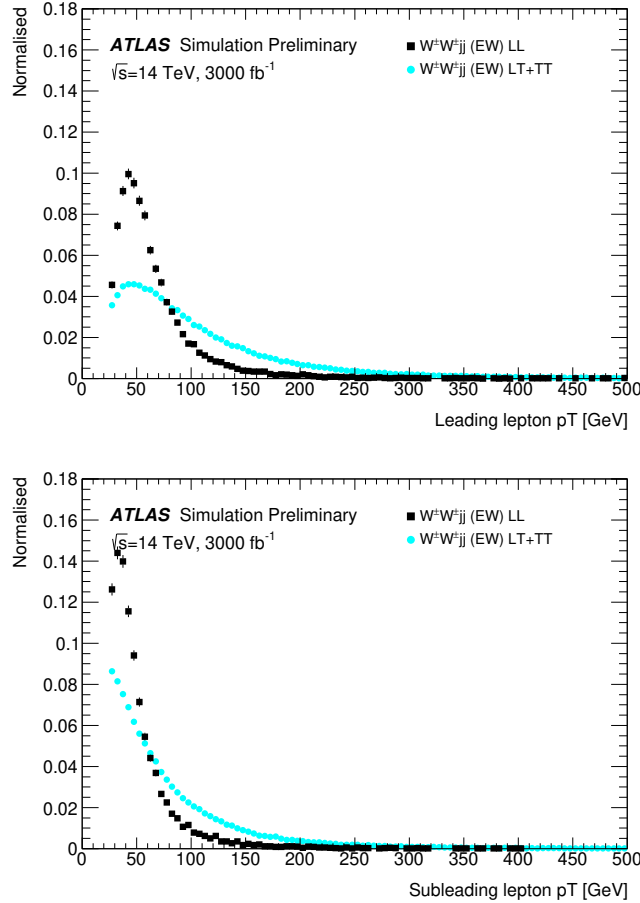


Figure 6.1: Comparison of the leading (top) and subleading (bottom) lepton  $p_T$  distributions for purely longitudinal (LL, black) and mixed polarization (LT+TT, cyan)  $W^\pm W^\pm jj$  events.

1805 There are many other processes that can produce the same final state as the  $W^\pm W^\pm jj$  and  
 1806 must also be accounted for using MC simulations.  $WZ$  events are generated using **SHERPA v2.2.0**,  
 1807 which includes up to one parton at NLO in the strong coupling constant and up to three addi-  
 1808 tional partons at LO. Both EWK and QCD production are included in these samples.  $ZZ$  and  
 1809 triboson  $VVV$  ( $V = W, Z$ ) events are generated using **SHERPA v2.2.2** with up to two additional  
 1810 partons in the final state. For the triboson backgrounds, the bosons can decay leptonically or  
 1811 hadronically.  $W+jets$  backgrounds are generated for electron, muon, and tau final states at LO  
 1812 with **Madgraph5\_aMC@NLO** and the **NNPDF3.0** set with showering from **PYTHIA v8**.  $Z+jets$  events are  
 1813 produced using **POWHEG-BOX v2** and the **CT10** PDF set interfaced with **PYTHIA v8**. Finally,  $t\bar{t}$  and  
 1814 single-top events are generated using **POWHEG-BOX** with showering from **PYTHIA v6**.

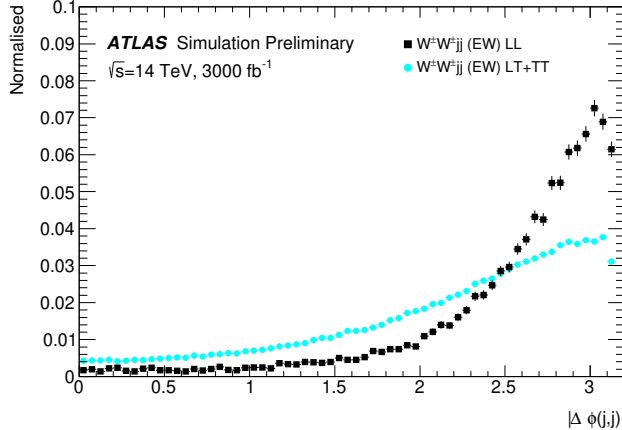


Figure 6.2: Comparison of the azimuthal dijet separation ( $|\Delta\phi_{jj}|$ ) for purely longitudinal (LL, black) and mixed polarization (LT+TT, cyan)  $W^\pm W^\pm jj$  events.

Process	Generator	Comments
$W^\pm W^\pm jj$ (EWK)	Madgraph5_aMC@NLO	Signal sample
$W^\pm W^\pm jj$ (QCD)	Madgraph5_aMC@NLO	
$W^\pm W^\pm jj$ (LL)	Madgraph5_aMC@NLO	Pure longitudinal polarization sample
$W^\pm W^\pm jj$ (TT+LT)	Madgraph5_aMC@NLO	Mixed and transverse polarization sample
Diboson	SHERPA v2.2.0	$WZ$ events
	SHERPA v2.2.2	$ZZ$ events
Triboson	SHERPA v2.2.2	
$W+jets$	Madgraph5_aMC@NLO	
$Z+jets$	POWHEG-BOX v2	
$t\bar{t}$	POWHEG-BOX	
Single top	POWHEG-BOS	

Table 6.1: Summary of MC samples used in the analysis.

### 1815 6.3 Background estimations

1816 In this analysis, all background contributions are estimated using MC simulations. Backgrounds such  
 1817 as electron charge misidentification and fake electrons from jets (which are traditionally estimated  
 1818 using data-driven techniques) are estimated using a set of parameterization functions applied to the  
 1819 MC. These functions calculate the probability that an electron is assigned the wrong charge or a  
 1820 jet is mis-reconstructed as an electron parameterized by the  $p_T$  and  $\eta$  of the electron or jet. The  
 1821 probabilities are derived from studies on expected electron performance with the upgraded ATLAS  
 1822 detector [88].

1823 Processes involving two  $W$  and  $Z$  bosons are grouped together as *diboson* backgrounds, with the

exception of  $W^\pm W^\pm jj$  events produced via QCD interactions, which are kept separate. Similarly, all backgrounds with three vector bosons are combined and labeled as *triboson*. Any  $W+jets$  or top events that pass selection and do not contain a fake electron, as well as any  $Z+jets$  events without an electron identified as having its charge misidentified are combined as *other non-prompt* backgrounds.

### 6.3.1 Truth-based isolation

To properly calculate particle isolation, it requires information from several detector subsystems including tracking and calorimeter responses. Since the MC samples used in this analysis have not been run through a full detector simulation, it is not possible to construct the canonical isolation variables used in analyses. At truth-level, this is generally not a serious concern as  $p_T$  signal leptons tend to be well isolated to begin with. However, isolation is one of the most powerful tools for rejecting leptons from non-prompt sources such as top events, which are produced in association with additional nearby particles from  $b$  and  $c$  quark decays. In this analysis, with the absence of any sort of isolation requirement, contributions from top backgrounds (including single top,  $t\bar{t}$  and  $t\bar{t} + V$ ) are more than an order of magnitude higher than expected.

As a result, it is necessary to find one or more quantities that are comparable to the isolation information that is available in fully-simulated samples. Analogues to track- and calorimeter-based isolation variables are constructed by summing the momentum and energy, respectively, of stable truth particles with  $p_T > 1$  GeV within a specified radius of each signal lepton. For the track-based isolation, only charged truth particles are used; both charged and neutral particles (excluding neutrinos) are included for the calorimeter-based isolation. Ultimately, a set of isolation cuts are chosen that are similar to those recommended by ATLAS for Run 2 analyses. The truth-based isolation requirements are listed in Table 6.2.

	Electron Isolation	Muon Isolation
Track-based isolation cone size	$\Delta R < 0.2$	$\Delta R < 0.3$
Track-based isolation requirement	$\sum p_T/p_T^e < 0.06$	$\sum p_T/p_T^\mu < 0.04$
Calorimeter-based isolation cone size	$\Delta R < 0.2$	$\Delta R < 0.2$
Calorimeter-based isolation requirement	$\sum E_T/p_T^e < 0.06$	$\sum E_T/p_T^\mu < 0.15$

Table 6.2: Truth-based isolation requirements for electrons and muons.

The truth-based isolation requirement reduces the top background by over 99%, and the percentage of the total background consisting of top events is reduced from 83% to 2%. Additional details on the truth-based isolation studies are presented in Appendix A.

---

1849 **6.4 Object and event selection**

1850 **6.4.1 Object selection**

1851 Electrons and muons are preselected to have  $p_T > 7$  and  $6$  GeV, respectively, and  $|\eta| \leq 4.0$ . The  
 1852 likelihood of a given lepton to pass the trigger and identification requirements is estimated by  
 1853 calculating an efficiency dependent on the  $p_T$  and  $\eta$  of the lepton. The leptons are also required to  
 1854 pass the isolation criteria detailed in Table 6.2. Jets that have been tagged as a fake electron by the  
 1855 functions described in Section 6.3 are treated as electrons for the purpose of the object selection and  
 1856 are subject to the same criteria. In order to be considered a signal lepton, an additional requirement  
 1857 of  $p_T > 25$  GeV is applied on top of the preselection. The two highest  $p_T$  leptons passing this  
 1858 selection are chosen to be the leading and subleading signal leptons.

1859 Jets are clustered using the anti- $k_t$  algorithm [71] from final-state particles within a radius of  
 1860  $\Delta R = 0.4$  (excluding muons and neutrinos). Jets are required to have  $p_T > 30$  GeV and lie within  
 1861  $|\eta| < 4.5$ , with an additional cut of  $p_T > 70$  GeV for jets above  $|\eta| \geq 3.8$  in order to suppress jets  
 1862 from pileup interactions. Jets overlapping with a preselected electron within  $\Delta R(e, j) < 0.05$  are  
 1863 removed in order to prevent double counting. The two highest  $p_T$  jets are defined as the leading  
 1864 and subleading *tag jets*.

1865 **6.4.2 Event selection**

1866 The default event selection is summarized in Table 6.3 and described here. Exactly two signal  
 1867 leptons are required with the same electric charge and separated from each other by  $\Delta R(l l) > 0.3$ .  
 1868 In order to suppress contributions from Drell-Yan backgrounds, the two signal leptons must have  
 1869 an invariant mass  $m_{ll}$  greater than  $20$  GeV. Additionally, if both signal leptons are electrons, their  
 1870 mass must be at least  $10$  GeV from the  $Z$ -boson mass in order to reduce background from  $Z$ -boson  
 1871 decays<sup>18</sup>. The event is required to have at least  $40$  GeV of missing transverse energy ( $E_T^{\text{miss}}$ ) to  
 1872 account for the two neutrinos from the  $W$  decays. Events with additional preselected leptons are  
 1873 vetoed, which greatly reduces  $WZ$  and  $ZZ$  backgrounds.

1874 Each event must have at least two jets, and both tag jets are required to not overlap with the  
 1875 signal leptons, and there is a veto on events with one or more  $b$ -jets. In order to preferentially select  
 1876 EWK production, the tag jets are also required to have a large separation between them and a large

---

<sup>18</sup>The electron charge misidentification rate in the upgraded ATLAS detector is estimated to be high enough that contributions from  $Z \rightarrow ee$  backgrounds are non-negligible.

<sup>1877</sup> invariant mass. Finally, a cut on the lepton centrality<sup>19</sup>,  $\zeta$ , defined in Equation 6.1 enhances the  
<sup>1878</sup> EWK  $W^\pm W^\pm jj$  signal.

$$\zeta = \min[\min(\eta_{\ell 1}, \eta_{\ell 2}) - \min(\eta_{j 1}, \eta_{j 2}), \max(\eta_{j 1}, \eta_{j 2}) - \max(\eta_{\ell 1}, \eta_{\ell 2})] \quad (6.1)$$

Selection requirement	Selection value
Lepton kinematics	$p_T > 25 \text{ GeV}$ $ \eta  \leq 4.0$
Jet kinematics	$p_T > 30 \text{ GeV}$ for $ \eta  \leq 4.5$ $p_T > 70 \text{ GeV}$ for $ \eta  > 3.8$
Dilepton charge	Exactly two signal leptons with same charge
Dilepton separation	$\Delta R_{l,l} \geq 0.3$
Dilepton mass	$m_{ll} > 20 \text{ GeV}$
$Z$ boson veto	$ m_{ee} - m_Z  > 10 \text{ GeV}$ ( $ee$ -channel only)
$E_T^{\text{miss}}$	$E_T^{\text{miss}} > 40 \text{ GeV}$
Jet selection	At least two jets with $\Delta R_{l,j} > 0.3$
$b$ jet veto	$N_{b\text{-jet}} = 0$
Dijet separation	$\Delta \eta_{jj} > 2.5$
Trilepton veto	No additional preselected leptons
Dijet mass	$m_{jj} > 500 \text{ GeV}$
Lepton-jet centrality	$\zeta > 0$

Table 6.3: Summary of the signal event selection.

## <sup>1879</sup> 6.5 Selection optimization

<sup>1880</sup> An upgraded detector along with an increase in center of mass energy and integrated luminosity  
<sup>1881</sup> provides an opportunity to study whether the event selection can be optimized to improve the signal  
<sup>1882</sup> to background ratio.

### <sup>1883</sup> 6.5.1 Random grid search algorithm

<sup>1884</sup> The chosen method for optimizing the event selection is a cut-based algorithm known as the Random  
<sup>1885</sup> Grid Search (RGS) [89]. Consider a simple case of two variables  $x$  and  $y$  chosen to differentiate signal  
<sup>1886</sup> from background. In order to be considered a signal event, a given event would be required to pass  
<sup>1887</sup> a set of selection criteria, called a *cut point*:  $c = \{x > x_c, y > y_c\}$ . A simple method to choose the  
<sup>1888</sup> optimal cut point (i.e. the “best” values of the cuts  $x_c$  and  $y_c$ ) would be to construct an  $n \times m$

---

<sup>19</sup> $\zeta$  is a measurement of whether the two signal leptons lie between the two tagging jets in  $\eta$ , as is preferred by the VBS topology.

1889 rectangular grid in  $x$  and  $y$  consisting of points  $(x_0, y_0), (x_1, y_1), \dots, (x_n, y_m)$ , as in Figure 6.3. One  
 1890 can then choose a cut point  $c_k = \{x > x_i, y > y_j\}$  that maximizes the signal significance as measured  
 1891 by a chosen metric. This would be considered a *rectangular grid search*.

1892 While effective in principle, a rectangular grid search comes with two major drawbacks:

- 1893 1. The algorithm scales exponentially as the number of variables to be optimized increases, as  
 1894 this is effectively increasing the dimensionality of the grid. In the simple case of a square grid  
 1895 with  $N$  bins per variable  $v$ , the number of cut points to be evaluated grows as  $N^v$ .
- 1896 2. Signal and background samples are rarely evenly distributed over the entire grid, resulting  
 1897 in many cut points being sub-optimal and evaluating them would be a waste of computing  
 1898 resources.

1899 To combat these limitations, the RGS algorithm constructs a grid of cut points directly from  
 1900 the signal sample itself. In the two-dimensional example, this means that the variables  $x_i$  and  $y_j$   
 1901 making up the cut point  $c_k = \{x > x_i, y > y_j\}$  take their values directly from a given signal event.  
 1902 This has the benefit of creating a *random grid* of cut points that is biased towards regions of high  
 1903 signal concentration by construction. This reduces the need for exponentially increasing numbers of  
 1904 cut points while ensuring that computing resources are not wasted in regions with few to no signal  
 1905 events. An example of the the two-dimensional random grid is shown in Figure 6.4.

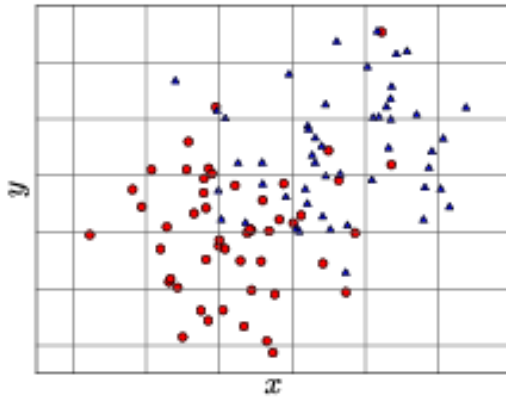


Figure 6.3: A visual representation of a rectangular grid search algorithm. The signal events are the blue triangles, and the red circles are the background events. **TODO: replace with own figure**

1906 Once the random grid of cut points is constructed, the optimal cut point can be chosen using any  
 1907 number of metrics, such as signal to background ratio. For the purpose of the  $W^\pm W^\pm jj$  upgrade

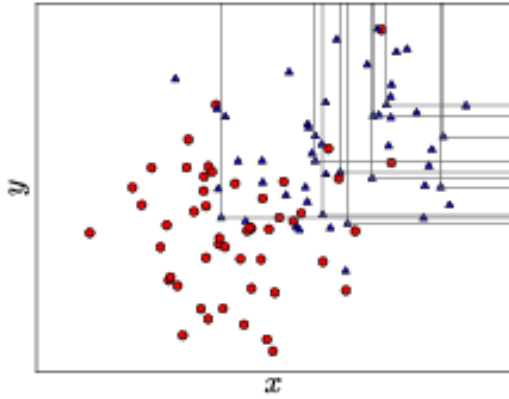


Figure 6.4: A visual representation of a random grid search algorithm. The signal events are the blue triangles, and the red circles are the background events. **TODO: replace with own figure**

1908 study, the optimal cut point is chosen to be the one that maximizes the signal significance  $Z$  as  
1909 defined in Equation 6.2 [90].

$$Z = \sqrt{2 \left[ (s + b) \ln \left( \frac{s + b}{b_0} \right) + b_0 - s - b \right] + \frac{(b - b_0)^2}{\sigma_b^2}} \quad (6.2)$$

1910 where  $s$  and  $b$  are the number of signal and background events, respectively,  $\sigma_b$  is the total uncertainty  
1911 on the background, and  $b_0$  is defined as:

$$b_0 = \frac{1}{2} \left( b - \sigma_b^2 + \sqrt{(b - \sigma_b^2)^2 + 4(s + b)\sigma_b^2} \right) \quad (6.3)$$

1912 In the case where the background is known precisely (i.e.  $\sigma_b = 0$ ), Equation 6.2 simplifies to

$$Z = \sqrt{2 \left( b \left[ (1 + s/b) \ln(1 + s/b) - s/b \right] \right)} \quad (6.4)$$

1913 which further reduces to the familiar  $Z = s/\sqrt{b}$  for the case when  $s \ll b$ .

### 1914 6.5.2 Inputs to the optimization

1915 In order to train the RGS, signal and background samples are prepared from events passing the  
1916 event selection outlined in Table 6.3 up through the  $b$ -jet veto. The signal sample is chosen to be  
1917 the longitudinally polarized  $W^\pm W^\pm jj$  EWK events, and the transverse and mixed polarizations  
1918 are treated as background along with  $W^\pm W^\pm jj$  events from QCD interactions and the traditional  
1919 backgrounds listed in Section 6.3. Splitting the inclusive  $W^\pm W^\pm jj$  EWK events by polarization

1920 allows the optimization to favor the longitudinally polarized events as much as possible, even though  
 1921 they both contribute to the EWK signal.

1922 The following variables are chosen for optimization:

- 1923 • Leading lepton  $p_T$
- 1924 • Dilepton invariant mass ( $m_{ll}$ )
- 1925 • Leading and subleading jet  $p_T$
- 1926 • Dijet invariant mass ( $m_{jj}$ )
- 1927 • Lepton-jet centrality ( $\zeta$ )

1928 Subleading lepton  $p_T$  is omitted as it is desirable to keep the cut value as low as possible due to  
 1929 its sensitivity to the longitudinal polarization (as discussed in Section 6.1.1). Additionally, the dijet  
 1930 separation  $\Delta\eta_{jj}$  was included in the optimization originally, however it was dropped from the list due  
 1931 to the cut value being motivated by differences between EWK and QCD produced  $W^\pm W^\pm jj$  events.

1932 Two additional constraints were imposed when selecting the optimal cut point:

- 1933 1. At least 1000 signal events must survive in order to prevent the optimization from being too  
 1934 aggressive and unnecessarily reducing signal statistics.
- 1935 2. The dijet invariant mass may only vary within a 50 GeV range of the default value (from  
 1936 450 – 550 GeV) due to the cut being physically motivated by the VBS event topology (see  
 1937 Section 5.0.3).

1938 Lastly, the signal significance is calculated without taking into account the uncertainty of the  
 1939 background using Equation 6.4. This is due to the fact that the statistical uncertainties of the fake  
 1940 electron and charge misidentification backgrounds are quite large, owing to poor MC statistics in a  
 1941 few of the samples. If Equation 6.2 were used instead, the optimization will cut unreasonably hard  
 1942 against these backgrounds. Since Monte Carlo statistics is not expected to be a limiting factor when  
 1943 this analysis is performed at the HL-LHC, it is more realistic to simply ignore these large statistical  
 1944 uncertainties for the purpose of the optimization.

### 1945 6.5.3 Results of the optimization

1946 Ultimately, the random grid is constructed from over 38,000 LL-polarized  $W^\pm W^\pm jj$  events in the  
 1947 six variables listed above. After applying the constraints, the optimal cut point reduces the total

background from 9900 to 2310 while reducing the signal from 3489 to 2958. This corresponds to an increase in signal significance from  $Z = 33.26$  to  $Z = 52.63$  as calculated by Equation 6.4. The updates to the event selection are listed in Table 6.4.

The large reduction in the background is primarily a result of the increase in the leading and subleading jet  $p_T$  from 30 GeV to 90 GeV and 45 GeV, respectively. As can be seen in Figure 6.7, this increase removes a significant portion of the backgrounds from jets faking electrons and charge mis-ID. Additionally, the loosening of the lepton-jet centrality cut  $\zeta$  allows more signal events to survive the event selection (see Figure 6.9). Other changes to the event selection are minor and do not individually have a large impact on the signal or background yields.

The full event yields after optimization as well as the cross section measurement are detailed alongside those using the default selection in Section 6.6.

**TODO:** It's a bit awkward to reference the results of the default/optimized before they're properly presented. Maybe move the sections around? not sure...

Selection requirement	Selection value
Lepton kinematics	$p_T > 28$ GeV (leading lepton only)
Jet kinematics	$p_T > 90$ GeV (leading jet) $p_T > 45$ GeV (subleading jet)
Dilepton mass	$m_{ll} > 28$ GeV
Dijet mass	$m_{jj} > 520$ GeV
Lepton-jet centrality	$\zeta > -0.5$

Table 6.4: Updates to the  $W^\pm W^\pm jj$  event selection criteria after optimization. Cuts not listed remain unchanged from the default selection in Table 6.3.

## 6.6 Results

### 6.6.1 Event yields

After applying the full event selection, the analysis is broken down into four channels based off of the flavor of the signal leptons:  $\mu\mu$ ,  $ee$ ,  $\mu e$ , and  $e\mu$ . The full signal and background event yields are shown in Table 6.5 for each channel separately and combined using the default event selection. 3489 EWK  $W^\pm W^\pm jj$  events are expected compared to 9900 background events. The dominant sources of background are jets faking electrons followed by charge misidentification and diboson processes. Triboson events, QCD  $W^\pm W^\pm jj$ , and other non-prompt sources make up approximately 5% of the total background combined.

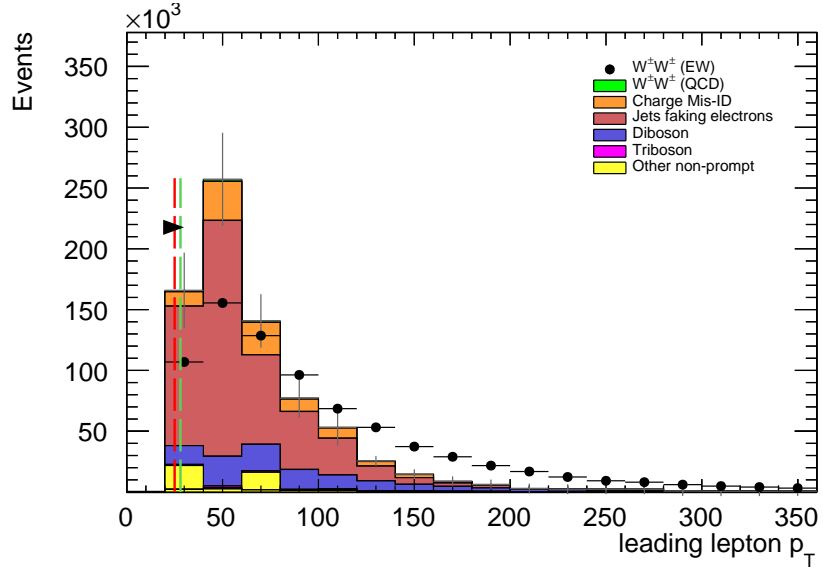


Figure 6.5: Leading lepton  $p_T$  distribution. The default and optimized cuts are represented by the red and green dashed lines, respectively. The  $W^\pm W^\pm jj$  EWK signal (black points) is normalized to the same area as the sum of the backgrounds (colored histogram). **TODO: Move to appendix or omit**

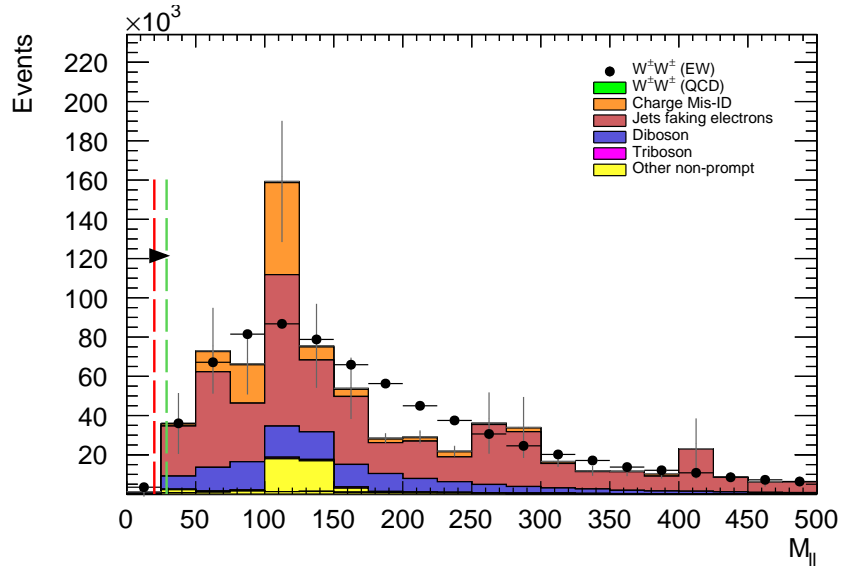


Figure 6.6: Dilepton invariant mass distribution. The default and optimized cuts are represented by the red and green dashed lines, respectively. The  $W^\pm W^\pm jj$  EWK signal (black points) is normalized to the same area as the sum of the backgrounds (colored histogram). **TODO: Move to appendix or omit**

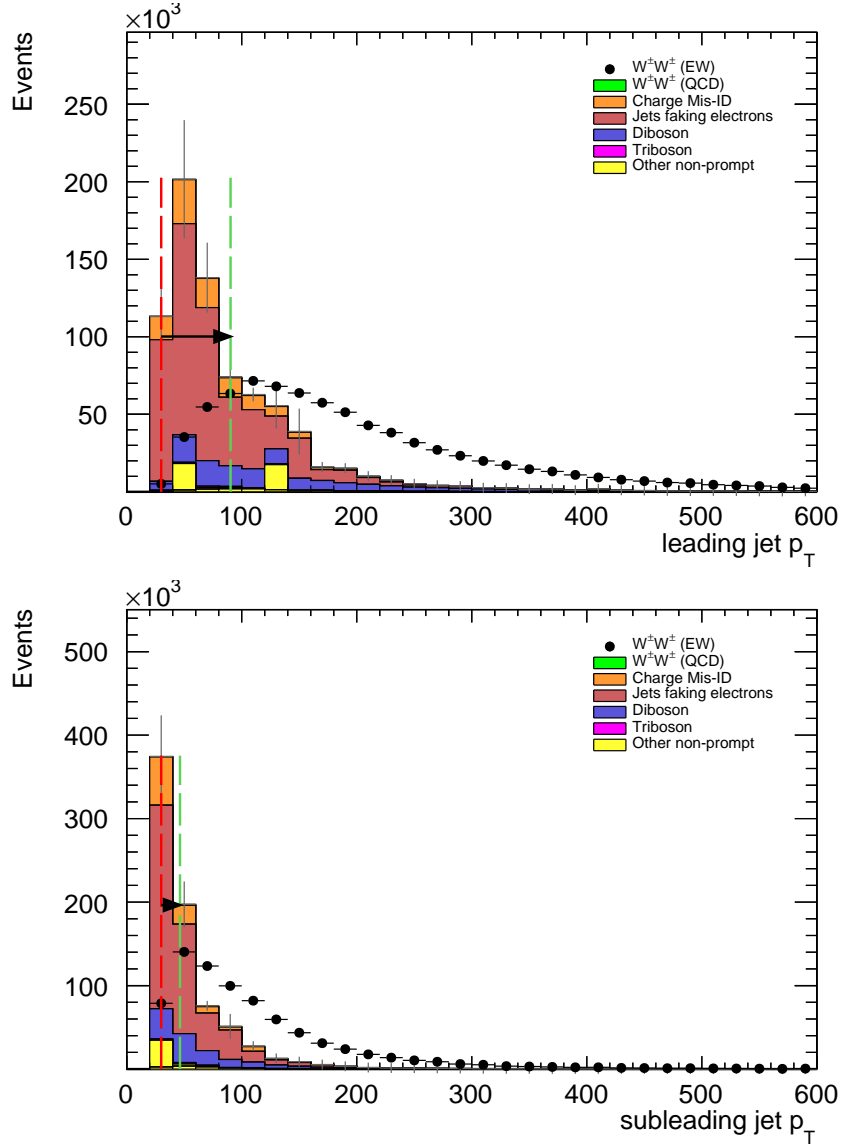


Figure 6.7: Leading (top) and subleading (bottom) jet  $p_T$  distributions. The default and optimized cuts are represented by the red and green dashed lines, respectively. The  $W^\pm W^\pm jj$  EWK signal (black points) is normalized to the same area as the sum of the backgrounds (colored histogram).

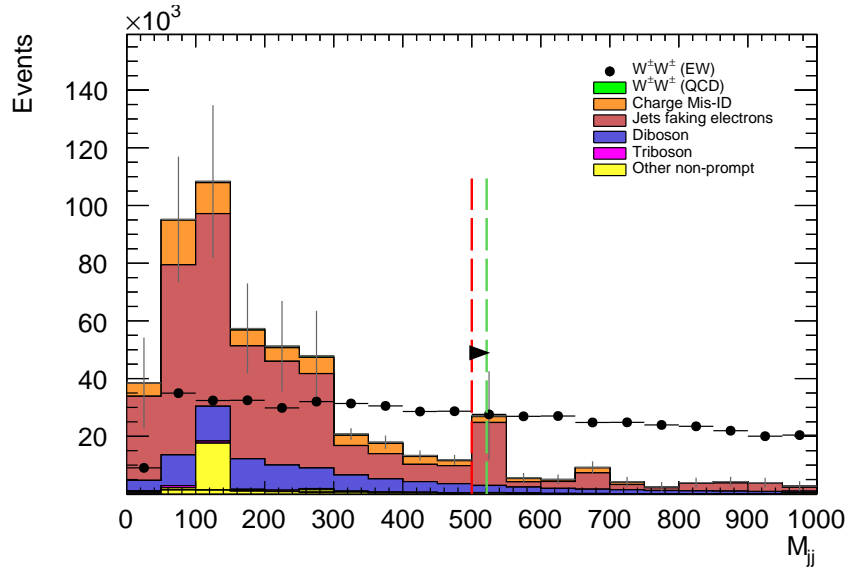


Figure 6.8: Dijet invariant mass distribution. The default and optimized cuts are represented by the red and green dashed lines, respectively. The  $W^\pm W^\pm jj$  EWK signal (black points) is normalized to the same area as the sum of the backgrounds (colored histogram). **TODO:** Move to appendix or omit

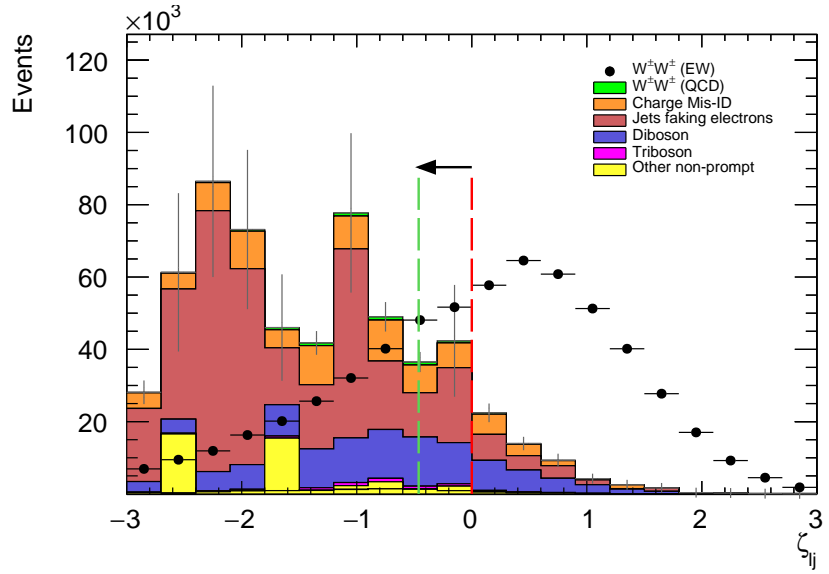


Figure 6.9: Lepton-jet centrality distribution. The default and optimized cuts are represented by the red and green dashed lines, respectively. The  $W^\pm W^\pm jj$  EWK signal (black points) is normalized to the same area as the sum of the backgrounds (colored histogram).

	All channels	$\mu\mu$	$ee$	$\mu e$	$e\mu$
$W^\pm W^\pm jj$ (QCD)	206.4	91.1	22.8	38.4	54.1
Charge Misidentification	2300	0.0	2100	90	160
Jets faking electrons	5000	0.0	3400	1200	340
$WZ + ZZ$	2040	500	438	423	680
Tribosons	115	47	15.4	21.6	31.2
Other non-prompt	210	110	20	60	27
Total Background	9900	750	6000	1900	1290
Signal $W^\pm W^\pm jj$ (EWK)	3489	1435	432	679	944

Table 6.5: Signal and background event yields using the default event selection for an integrated luminosity of  $\mathcal{L} = 3000 \text{ fb}^{-1}$ . Events containing a fake or charge-flipped electron are removed from their respective sources and combined into a single entry each.

1970        The event yields for the optimized selection detailed in Section 6.5.3 are listed in Table 6.6. After  
 1971 optimization, 2958 signal events and just 2310 background events are expected. Diboson events are  
 1972 now the primary source of background, as the optimization greatly reduces the fake and charge  
 1973 misidentification backgrounds. As discussed earlier, the increase in the leading and subleading jet  
 1974  $p_T$  cuts as well as the loosening of the centrality cut are most responsible for the changes in the  
 1975 signal and background yields; distributions of these quantities using the default and the optimized  
 1976 event selections can be found in Figures 6.10, 6.11, and 6.12, respectively.

	All channels	$\mu\mu$	$ee$	$\mu e$	$e\mu$
$W^\pm W^\pm jj$ (QCD)	168.7	74.6	19.7	32.2	42.2
Charge Misidentification	200	0.0	11	30	160
Jets faking electrons	460	0.0	130	260	70
$WZ + ZZ$	1286	322	289	271	404
Tribosons	76	30.1	9.6	15.1	21.6
Other non-prompt	120	29	16.6	50	19
Total Background	2310	455	480	660	710
Signal $W^\pm W^\pm jj$ (EWK)	2958	1228	380	589	761

Table 6.6: Signal and background event yields using the optimized event selection for an integrated luminosity of  $\mathcal{L} = 3000 \text{ fb}^{-1}$ . Events containing a fake or charge-flipped electron are removed from their respective sources and combined into a single entry each.

1977        It is important to note, however, that the MC sample used to estimate  $Z + \text{jets}$  events suffers from  
 1978 poor statistics which results in large per-event weights once scaled to  $\mathcal{L} = 3000 \text{ fb}^{-1}$ . This sample  
 1979 contributes heavily to the fake and charge misidentification backgrounds, and a handful of these  
 1980 events being cut out by the optimization contributes has a large effect on the dramatic reduction  
 1981 of these backgrounds. As a result, these particular optimized results are likely overly optimistic.  
 1982 However, given proper MC statistics, it is still expected that the optimization will outperform the

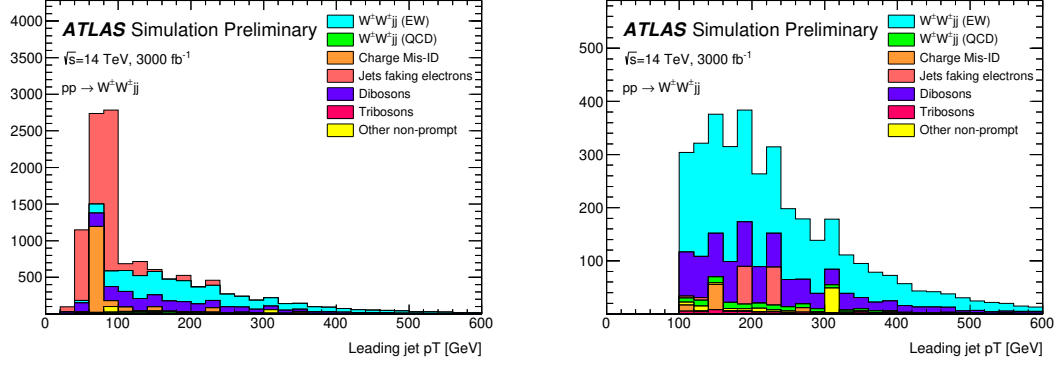


Figure 6.10:  $p_T$  distributions for the leading jet using the default (left) and optimized (right) event selections for all channels combined.

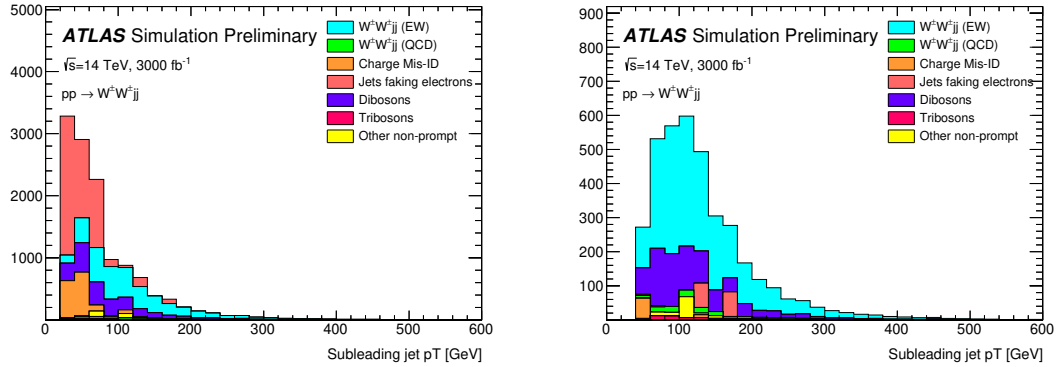


Figure 6.11:  $p_T$  distributions for the subleading jet using the default (left) and optimized (right) event selections for all channels combined.

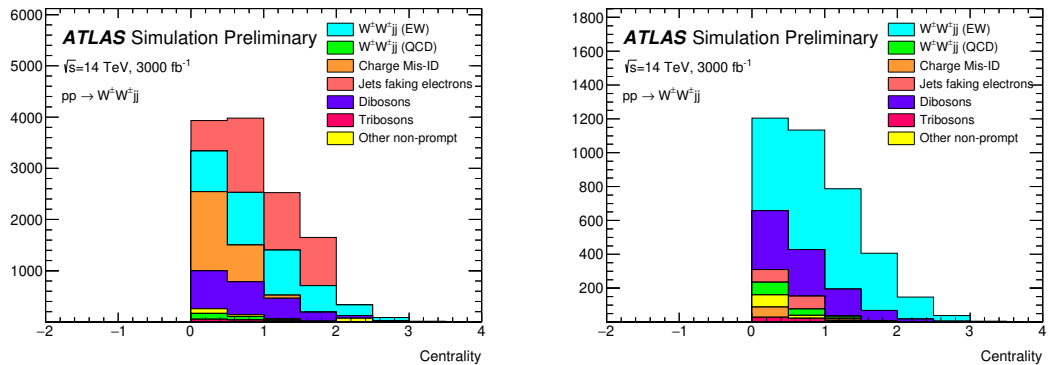


Figure 6.12:  $p_T$  distributions for lepton-jet centrality  $\zeta$  using the default (left) and optimized (right) event selections for all channels combined.

1983 default selection.

### 1984 6.6.2 Uncertainties

1985 TODO: Ask for details on how some of these uncertainties were calculated – specifically the fakes and  
 1986 charge mis-ID The uncertainties considered for the analysis are summarized in Table 6.7. Values for  
 1987 experimental systematics on the trigger efficiency, lepton and jet reconstruction, and flavor tagging  
 1988 are taken directly from the 13 TeV analysis [44]. The rate uncertainties for the background processes  
 1989 are halved from the 13 TeV values.

Source	Uncertainty (%)
$W^\pm W^\pm jj$ (EWK)	3
Luminosity	1
Trigger efficiency	0.5
Lepton reconstruction and identification	1.8
Jets	2.3
Flavor tagging	1.8
Jets faking electrons	20
Charge misidentification	25
$W^\pm W^\pm jj$ (QCD)	20
Top	15
Diboson	10
Triboson	15

Table 6.7: Summary of estimated experimental and rate uncertainties.

### 1990 6.6.3 Cross section measurement

1991 The cross section is calculated using the same method as in the 13 TeV analysis, detailed in Chap-  
 1992 ter 5. TODO: update from chapter reference to subsection reference (once it's written)... Once  
 1993 again, each of the four lepton flavor channels is further split by charge (i.e.  $\mu\mu \rightarrow \mu^+\mu^+ + \mu^-\mu^-$ ),  
 1994 as this increases the sensitivity of the analysis. Each channel's  $m_{jj}$  distribution is combined in a  
 1995 profile likelihood fit to extract the EWK  $W^\pm W^\pm jj$  production cross section. The expected cross  
 1996 section calculated using the default event selection is:

$$\sigma_{W^\pm W^\pm jj}^{\text{expected}} = 16.89 \pm 0.36 \text{ (stat)} \pm 0.53 \text{ (theory)} \pm 0.84 \text{ (syst)} \text{ fb} \quad (6.5)$$

1997 The expected cross section calculated using the optimized event selection is:

$$\sigma_{W^\pm W^\pm jj}^{\text{expected}} = 16.94 \pm 0.36 \text{ (stat)} \pm 0.53 \text{ (theory)} \pm 0.78 \text{ (syst)} \text{ fb} \quad (6.6)$$

1998 The optimized selection should not change the measured value of the cross section, and indeed both  
 1999 are consistent with within uncertainties. The systematic uncertainty is reduced by approximately 7%  
 2000 with the optimized selection. Projections of the total uncertainty on the cross section as a function  
 2001 of integrated luminosity made by [TODO: how was this made?](#) is shown in Figure 6.13. As the  
 2002 integrated luminosity increases past  $\mathcal{L} > 3000 \text{ fb}^{-1}$ , the statistical uncertainty reduces faster than  
 2003 the systematic uncertainties. However, the total uncertainty is expected to reduce by less than a  
 2004 percent with increased luminosity past the planned  $3000 \text{ fb}^{-1}$ .

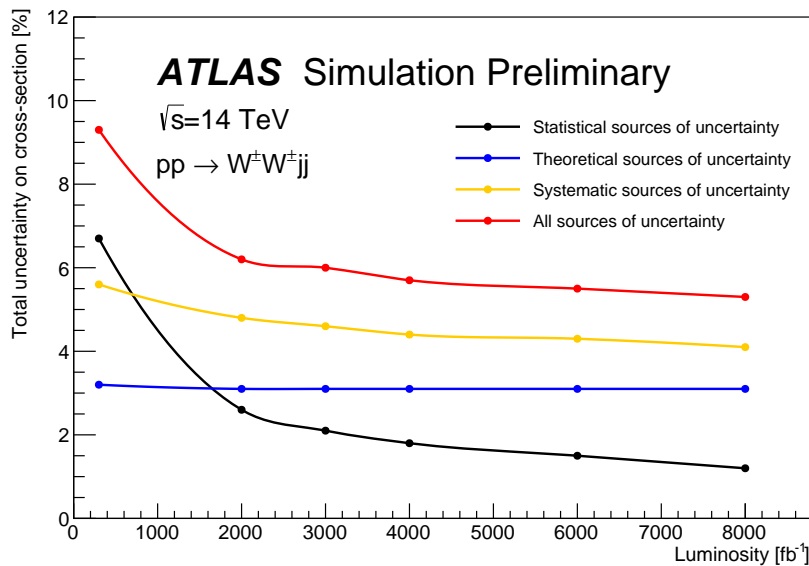


Figure 6.13: Projections of the statistical (black), theoretical (blue), systematic (yellow), and total (red) uncertainties on the measured cross section as a function of integrated luminosity using the optimized event selection.

#### 2005 6.6.4 Longitudinal scattering significance

2006 [TODO: get some details on how this was all done...](#) The longitudinal scattering significance is  
 2007 extracted from the  $|\Delta\phi_{jj}|$  distribution using a simultaneous binned likelihood fit. In order to increase  
 2008 sensitivity, the  $|\Delta\phi_{jj}|$  distribution was split into two bins in  $m_{jj}$ , and an additional cut on the  
 2009 pseudorapidity of the subleading lepton was applied ( $|\eta| < 2.5$ ) to reduce background from fake and  
 2010 charge misidentification. The  $|\Delta\phi_{jj}|$  distributions used in the fit are shown in Figure 6.14. Due to  
 2011 limited statistics, the four lepton flavor channels were not split by charge. The expected significance

2012 of the  $W_L^\pm W_L^\pm jj$  process is  $1.8\sigma$  with a precision of 47% on the measurement. Projections of the  
2013 expected significance as a function of integrated luminosity is shown in Figure 6.15.

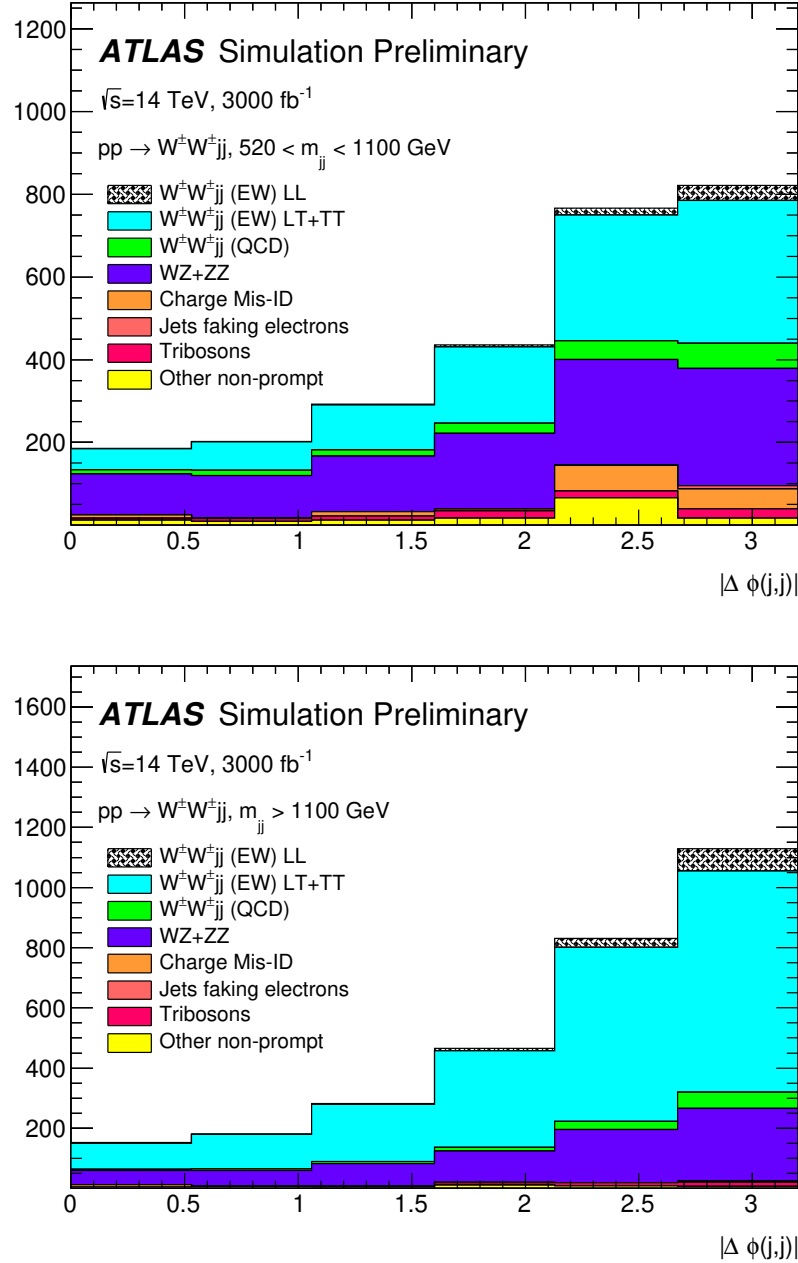


Figure 6.14: Dijet azimuthal separation ( $|\Delta\phi_{jj}|$ ) for the low  $m_{jj}$  region ( $520 < m_{jj} < 1100 \text{ GeV}$ , top) and the high  $m_{jj}$  region ( $m_{jj} > 1100 \text{ GeV}$ , bottom). The purely longitudinal (LL, gray) is plotted separately from the mixed and transverse (LT+TT, cyan) polarizations.

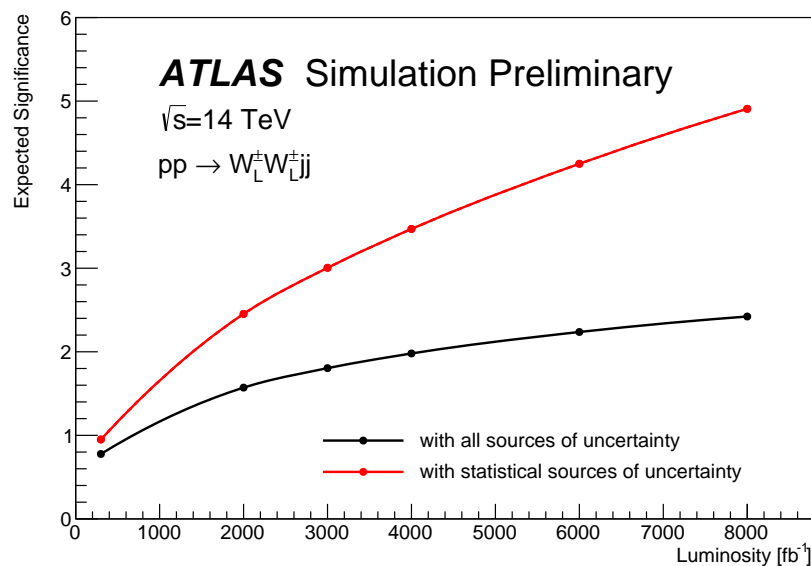


Figure 6.15: Projections of the expected longitudinal scattering significance as a function of integrated luminosity when considering all sources of uncertainties (black) or only statistical uncertainties (red).

2014

## CHAPTER 7

---

2015

## Conclusion

---

2016 Here's where you wrap it up.

2017 **Looking Ahead**

2018

2019 Here's an example of how to have an "informal subsection".

## APPENDIX A

# Additional material on truth isolation

yields by type	all channels	$\mu\mu$	$ee$	$\mu e$	$e\mu$
signal	4011	1583.2	531.7	793.1	1103.1
ww qcd	252.6	105.8	30.4	48	68.4
charge flip	2528.4	0.0	2075.4	255.1	197.8
fakes	7135.4	0.0	4675.1	1904.3	555.9
diboson	2370.4	581.2	491.8	517.9	779.6
triboson	125.5	49.1	17.8	24.6	34.1
top	90150.5	26618	15301.6	25277.9	22953.1
z+jets	241.2	0.0	0.0	0.0	241.2
w+jets	31.4	3.9	7.6	13.2	6.7
total bkg	102803.9	27354	22592	28027.8	24830.1
signal	4011	1583.2	531.7	793.1	1103.1

Table A.1: Event yields prior to applying any form of truth-based isolation criteria.

yields by type	all channels	$\mu\mu$	$ee$	$\mu e$	$e\mu$
signal	3470.5	1427.3	428.8	675.8	938.7
ww qcd	205.8	90.8	22.7	38.3	54
charge flip	2398.3	0.0	2104.6	95.8	197.9
fakes	4309.7	0.0	3390.6	750.8	168.3
diboson	1552.4	311.3	355.6	346.8	538.7
triboson	115	46.8	15.4	21.6	31.2
top	156.9	42.3	14.8	76.6	23.3
z+jets	0.0	0.0	0.0	0.0	0.0
w+jets	0.3	0.0	0.0	0.3	0.0
total bkg	8738.1	491.3	5903.7	1329.8	1013.4
signal	3470.5	1427.3	428.8	675.8	938.7

Table A.2: Event yields after applying a test version of the truth-based isolation.

2023

## APPENDIX B

2024

2025

# Additional material on $W^\pm W^\pm jj$ measurement at $\sqrt{s} = 13$ TeV

2026

### B.1 Impact of experimental uncertainty on MC background estimations

$W^\pm W^\pm jj$ QCD	$ee$ % Yield	$e\mu$ % Yield	$\mu\mu$ % Yield
Jet-related Uncertainties	3.41	3.04	2.85
b-tagging efficiency	2.56	2.48	2.48
Pile-up	4.99	0.45	0.33
Trigger efficiency	0.02	0.08	0.41
Lepton reconstruction/ID	1.62	1.19	1.89
MET reconstruction	0.41	0.22	0.34

Table B.1: Experimental systematics uncertainties for the  $W^\pm W^\pm jj$  QCD processes in all channels.

Triboson	$ee$ % Yield	$e\mu$ % Yield	$\mu\mu$ % Yield
Jet-related Uncertainties	13.09	13.39	16.85
b-tagging efficiency	2.96	3.77	4.95
Pile-up	19.37	24.66	6.87
Trigger efficiency	0.02	0.07	0.47
Lepton reconstruction/ID	1.66	1.27	2.48
MET reconstruction	0.00	0.46	0.00

Table B.2: Experimental systematics uncertainties for triboson process in all channels.

2027

plots go here

$t\bar{t}V$	$ee$ % Yield	$e\mu$ % Yield	$\mu\mu$ % Yield
Jet-related Uncertainties	17.65	11.97	14.27
b-tagging efficiency	15.02	9.04	13.83
Pile-up	8.73	10.69	4.18
Trigger efficiency	0.03	0.08	0.39
Lepton reconstruction/ID	2.57	3.27	2.66
MET reconstruction	1.75	4.16	1.62

Table B.3: Experimental systematics uncertainties for  $t\bar{t}V$  processes in all channels.

$W\gamma$	$ee$ % Yield	$e\mu$ % Yield	$\mu\mu$ % Yield
Jet-related Uncertainties	7.05	33.36	—
b-tagging efficiency	1.97	2.94	—
Pile-up	4.11	14.17	—
Trigger efficiency	0.01	0.14	—
Lepton reconstruction/ID	1.40	1.13	—
MET reconstruction	0.00	0.00	—

Table B.4: Experimental systematics uncertainties for the  $W\gamma$  process in all channels.

$Z\gamma$	$ee$ % Yield	$e\mu$ % Yield	$\mu\mu$ % Yield
Jet-related Uncertainties	16.22	370.44	—
b-tagging efficiency	1.08	3.10	—
Pile-up	12.57	11.51	—
Trigger efficiency	0.02	0.07	—
Lepton reconstruction/ID	1.26	22.01	—
MET reconstruction	0.00	0.00	—

Table B.5: Experimental systematics uncertainties for the  $Z\gamma$  process in all channels.

$ZZ$	$ee$ % Yield	$e\mu$ % Yield	$\mu\mu$ % Yield
Jet-related Uncertainties	15.71	15.76	35.18
b-tagging efficiency	2.23	2.35	2.89
Pile-up	1.22	3.20	4.58
Trigger efficiency	0.03	0.10	0.36
Lepton reconstruction/ID	3.59	3.10	5.70
MET reconstruction	4.84	3.26	3.24

Table B.6: Experimental systematics uncertainties for the  $ZZ$  process in all channels.

---

## Bibliography

---

- 2029 [1] S. Weinberg, *The Quantum Theory of Fields, Volume 1: Foundations*. Cambridge University  
2030 Press, 1995. 2.1
- 2031 [2] M. E. Peskin and D. V. Schroeder, *An Introduction to Quantum Field Theory*.  
2032 Addison-Wesley, 1995. 2.1
- 2033 [3] R. P. Feynman, *Mathematical formulation of the quantum theory of electromagnetic  
2034 interaction*, Phys. Rev. **80** (1950) 440–457. 2.1
- 2035 [4] M. Y. Han and Y. Nambu, *Three-triplet model with double SU(3) symmetry*, Phys. Rev. **139**  
2036 (1965) B1006–B1010. 2.1
- 2037 [5] D. J. Gross and F. Wilczek, *Asymptotically Free Gauge Theories - I*, Phys. Rev. **D8** (1973)  
2038 3633–3652. 2.1
- 2039 [6] D. J. Gross and F. Wilczek, *ASYMPTOTICALLY FREE GAUGE THEORIES. 2.*, Phys.  
2040 Rev. **D9** (1974) 980–993. 2.1
- 2041 [7] H. D. Politzer, *Reliable Perturbative Results for Strong Interactions?*, Phys. Rev. Lett. **30**  
2042 (1973) 1346–1349. [,274(1973)]. 2.1
- 2043 [8] A. Salam and J. C. Ward, *Weak and Electromagnetic Interactions*, Nuovo Cimento **11** (1959)  
2044 568–577. 2.1
- 2045 [9] S. L. Glashow, *The Renormalizability of Vector Meson Interactions*, Nucl. Phys. **10** (1959)  
2046 107–117. 2.1
- 2047 [10] ALEPH, DELPHI, L3, OPAL, SLD, LEP Electroweak Working Group, SLD Electroweak  
2048 Group, SLD Heavy Flavour Group Collaboration, S. Schael et al., *Precision electroweak  
2049 measurements on the Z resonance*, Phys. Rept. **427** (2006) 257–454, arXiv:hep-ex/0509008  
2050 [hep-ex]. 2.1
- 2051 [11] F. Englert and R. Brout, *Broken symmetry and the mass of gauge vector mesons*, Phys. Rev.  
2052 Lett. **13** (1964) 321–323. 2.1
- 2053 [12] P. W. Higgs, *Broken symmetries, massless particles and gauge fields*, Physics Letters **12**  
2054 (1964) 132–133. 2.1

- 2055 [13] P. W. Higgs, *Broken symmetries and the masses of gauge bosons*, Phys. Rev. Lett. **13** (1964)  
2056 508–509. 2.1
- 2057 [14] ATLAS Collaboration, *Observation of a new particle in the search for the Standard Model*  
2058 *Higgs boson with the ATLAS detector at the LHC*, Phys. Lett. B **716** (2012) 1,  
2059 arXiv:1207.7214 [hep-ex]. 2.1, 5.0.2
- 2060 [15] CMS Collaboration, *Observation of a new boson at a mass of 125 GeV with the CMS*  
2061 *experiment at the LHC*, Phys. Lett. B **716** (2012) 30, arXiv:1207.7235 [hep-ex]. 2.1, 5.0.2
- 2062 [16] UA1 Collaboration, G. Arnison et al., *Experimental Observation of Isolated Large Transverse*  
2063 *Energy Electrons with Associated Missing Energy at  $s^{**}(1/2) = 540\text{-GeV}$* , Phys. Lett. **B122**  
2064 (1983) 103–116. [,611(1983)]. 2.2
- 2065 [17] UA1 Collaboration, G. Arnison et al., *Experimental Observation of Lepton Pairs of Invariant*  
2066 *Mass Around  $95\text{-GeV}/c^{**2}$  at the CERN SPS Collider*, Phys. Lett. **B126** (1983) 398–410.  
2067 [,7.55(1983)]. 2.2
- 2068 [18] Particle Data Group Collaboration, K. A. Olive et al., *Review of Particle Physics*, Chin.  
2069 Phys. **C38** (2014) 090001. 2.2, 2.2
- 2070 [19] ATLAS Collaboration, G. Aad et al., *Evidence of  $W\gamma\gamma$  Production in  $pp$  Collisions at*  
2071  $\sqrt{s} = 8\text{ TeV}$  *and Limits on Anomalous Quartic Gauge Couplings with the ATLAS Detector*,  
2072 Phys. Rev. Lett. **115** (2015) no. 3, 031802, arXiv:1503.03243 [hep-ex]. 2.3
- 2073 [20] ATLAS Collaboration, ATLAS Collaboration, *Evidence for Electroweak Production*  
2074 *of  $W^\pm W^\pm jj$  in  $pp$  Collisions at  $\sqrt{s} = 8\text{ TeV}$  with the ATLAS Detector*, Phys. Rev. Lett. **113**  
2075 (2014) no. 14, 141803, arXiv:1405.6241 [hep-ex]. 2.3, 5
- 2076 [21] A. Falkowski, M. Gonzalez-Alonso, A. Greljo, D. Marzocca, and M. Son, *Anomalous Triple*  
2077 *Gauge Couplings in the Effective Field Theory Approach at the LHC*, JHEP **02** (2017) 115,  
2078 arXiv:1609.06312 [hep-ph]. 2.3
- 2079 [22] B. W. Lee, C. Quigg, and H. B. Thacker, *Weak Interactions at Very High-Energies: The Role*  
2080 *of the Higgs Boson Mass*, Phys. Rev. D **16** (1977) 1519. 2.3
- 2081 [23] D. R. Green, P. Meade, and M.-A. Pleier, *Multiboson interactions at the LHC*, Rev. Mod.  
2082 Phys. **89** (2017) no. 3, 035008, arXiv:1610.07572 [hep-ex]. 2.3
- 2083 [24] L. R. Evans and P. Bryant, *LHC Machine*, JINST **3** (2008) S08001.  
2084 <https://cds.cern.ch/record/1129806>. This report is an abridged version of the LHC  
2085 Design Report (CERN-2004-003). 3.1
- 2086 [25] ATLAS Collaboration, *The ATLAS Experiment at the CERN Large Hadron Collider*, JINST  
2087 **3** (2008) S08003. 3.1
- 2088 [26] ATLAS Collaboration, *ATLAS inner detector: Technical Design Report, Vol. 1*. CERN,  
2089 Geneva, 1997. <https://cds.cern.ch/record/331063>. 4
- 2090 [27] P. F. Åkesson, T. Atkinson, M. J. Costa, M. Elsing, S. Fleischmann, A. N. Gaponenko,  
2091 W. Liebig, E. Moyse, A. Salzburger, and M. Siebel, *ATLAS Tracking Event Data Model*,  
2092 Tech. Rep. ATL-SOFT-PUB-2006-004. ATL-COM-SOFT-2006-005.  
2093 CERN-ATL-COM-SOFT-2006-005, CERN, Geneva, Jul, 2006.  
2094 <https://cds.cern.ch/record/973401>. 4.1

- 2095 [28] P. Brückman, A. Hicheur, and S. J. Haywood, *Global chi2 approach to the Alignment of the*  
2096 *ATLAS Silicon Tracking Detectors*, Tech. Rep. ATL-INDET-PUB-2005-002.  
2097 ATL-COM-INDET-2005-004. CERN-ATL-INDET-PUB-2005-002, CERN, Geneva, 2005.  
2098 <https://cds.cern.ch/record/835270>. 4.1, 4.1
- 2099 [29] ATLAS Collaboration Collaboration, *Alignment of the ATLAS Inner Detector Tracking*  
2100 *System with 2010 LHC proton-proton collisions at  $\sqrt{s} = 7 \text{ TeV}$* , Tech. Rep.  
2101 ATLAS-CONF-2011-012, CERN, Geneva, Mar, 2011.  
2102 <https://cds.cern.ch/record/1334582>. 4.1, 4.2.3, 4.14
- 2103 [30] R. Härtel and S. Bethke, *Iterative local Chi2 alignment approach for the ATLAS SCT*  
2104 *detector*, Nov, 2005. <http://cds.cern.ch/record/1511044>. Presented 28 Nov 2005. 4.1
- 2105 [31] ATLAS Collaboration Collaboration, P. Brückman de Renstrom, *Alignment strategy for the*  
2106 *Inner Detector of ATLAS*, . <https://cds.cern.ch/record/1047114>. 4.1
- 2107 [32] *Alignment of the ATLAS Inner Detector and its Performance in 2012*, Tech. Rep.  
2108 ATLAS-CONF-2014-047, CERN, Geneva, Jul, 2014.  
2109 <https://cds.cern.ch/record/1741021>. 4.1, 4.2.1, 4.4
- 2110 [33] J. J. Peña, *Alignment of the ATLAS Inner Detector Upgraded for the LHC Run II*, *J. Phys.*  
2111 *Conf. Ser.* **664** (2015) no. 7, 072025. 4.1
- 2112 [34] J. Alison and I. J. Kroll, *The Road to Discovery: Detector Alignment, Electron Identification,*  
2113 *Particle Misidentification, WW Physics, and the Discovery of the Higgs Boson*, Dec, 2015.  
2114 <https://cds.cern.ch/record/1536507>. Presented 08 Nov 2012. 6
- 2115 [35] *ATLAS Inner Detector Alignment Performance with February 2015 Cosmic Rays Data*, Tech.  
2116 Rep. ATL-PHYS-PUB-2015-009, CERN, Geneva, Apr, 2015.  
2117 <https://cds.cern.ch/record/2008724>. 4.3, 4.2
- 2118 [36] ATLAS Collaboration Collaboration, M. Capeans, G. Darbo, K. Einsweiller, M. Elsing,  
2119 T. Flick, M. Garcia-Sciveres, C. Gemme, H. Pernegger, O. Rohne, and R. Vuillermet, *ATLAS*  
2120 *Insertable B-Layer Technical Design Report*, Tech. Rep. CERN-LHCC-2010-013.  
2121 ATLAS-TDR-19, Sep, 2010. <https://cds.cern.ch/record/1291633>. 4.2
- 2122 [37] *Alignment of the ATLAS Inner Detector with the initial LHC data at  $\sqrt{s} = 13 \text{ TeV}$* , Tech.  
2123 Rep. ATL-PHYS-PUB-2015-031, CERN, Geneva, Jul, 2015.  
2124 <https://cds.cern.ch/record/2038139>. 4.2
- 2125 [38] *Study of the mechanical stability of the ATLAS Insertable B-Layer*, Tech. Rep.  
2126 ATL-INDET-PUB-2015-001, CERN, Geneva, Jun, 2015.  
2127 <https://cds.cern.ch/record/2022587>. 4.2.1
- 2128 [39] *Common Framework Implementation for the Track-Based Alignment of the ATLAS Detector*,  
2129 Tech. Rep. ATL-SOFT-PUB-2014-003, CERN, Geneva, Mar, 2014.  
2130 <https://cds.cern.ch/record/1670354>. 4.2.1
- 2131 [40] ATLAS Collaboration Collaboration, *Study of alignment-related systematic effects on the*  
2132 *ATLAS Inner Detector track reconstruction*, Tech. Rep. ATLAS-CONF-2012-141, CERN,  
2133 Geneva, Oct, 2012. <https://cds.cern.ch/record/1483518>. 4.4, 4.4, 4.4.1.1, 4.4.1.2

- 2134 [41] S. Marti-Garcia, S. Camarda, T. Golling, M. Danninger, N. A. Styles, J. Wollrath, W. K.  
 2135 Di Clemente, S. Henkelmann, J. Jimenez Peña, O. Estrada Pastor, A. K. Morley, H. Oide,  
 2136 A. T. Vermeulen, P. Butti, E. Ricci, F. M. Follega, and R. Iuppa, *Studies of radial distortions*  
 2137 *of the ATLAS Inner Detector*, Tech. Rep. ATL-COM-INDET-2018-010, CERN, Geneva, Mar,  
 2138 2018. <https://cds.cern.ch/record/2306724>. 4.4
- 2139 [42] ATLAS Collaboration Collaboration, *Electron and photon energy calibration with the ATLAS*  
 2140 *detector using data collected in 2015 at  $\sqrt{s} = 13$  TeV*, Tech. Rep. ATL-PHYS-PUB-2016-015,  
 2141 CERN, Geneva, Aug, 2016. <https://cds.cern.ch/record/2203514>. 4.4.1
- 2142 [43] CMS Collaboration, V. Khachatryan et al., *Study of vector boson scattering and search for*  
 2143 *new physics in events with two same-sign leptons and two jets*, *Phys. Rev. Lett.* **114** (2015)  
 2144 no. 5, 051801, arXiv:1410.6315 [hep-ex]. 5
- 2145 [44] ATLAS Collaboration Collaboration, *Observation of electroweak production of a same-sign W*  
 2146 *boson pair in association with two jets in pp collisions at  $\sqrt{s} = 13$  TeV with the ATLAS*  
 2147 *detector*, Tech. Rep. ATLAS-CONF-2018-030, CERN, Geneva, Jul, 2018.  
 2148 <https://cds.cern.ch/record/2629411>. 5, 5.8, 6.6.2
- 2149 [45] CMS Collaboration, CMS Collaboration, *Observation of electroweak production of same-sign*  
 2150 *W boson pairs in the two jet and two same-sign lepton final state in proton-proton collisions*  
 2151 *at  $\sqrt{s} = 13$  TeV*, arXiv:1709.05822 [hep-ex]. 5
- 2152 [46] C. Bittrich, W. K. Di Clemente, et al., *Support note for measurement of electroweak*  
 2153  *$W^\pm W^\pm jj$  production at  $\sqrt{s} = 13$  TeV*, Tech. Rep. ATL-COM-PHYS-2018-252, CERN,  
 2154 Geneva, Mar, 2018. <https://cds.cern.ch/record/2309552>. 5, 5.3.3, 2, 4, 5.4.3
- 2155 [47] B. W. Lee, C. Quigg, and H. B. Thacker, *The Strength of Weak Interactions at Very*  
 2156 *High-Energies and the Higgs Boson Mass*, *Phys. Rev. Lett.* **38** (1977) 883–885. 5.0.2
- 2157 [48] S. D. Rindani, *Strong gauge boson scattering at the LHC*, in *Physics at the Large Hadron*  
 2158 *Collider*, A. Datta, B. Mukhopadhyaya, A. Raychaudhuri, A. K. Gupta, C. L. Khetrapal,  
 2159 T. Padmanabhan, and M. Vijayan, eds., pp. 145–155. 2009. arXiv:0910.5068 [hep-ph]. 5.0.2
- 2160 [49] A. Alboteanu, W. Kilian, and J. Reuter, *Resonances and Unitarity in Weak Boson Scattering*  
 2161 *at the LHC*, *JHEP* **11** (2008) 010, arXiv:0806.4145 [hep-ph]. 5.0.2, 5.1
- 2162 [50] J. M. Campbell and R. K. Ellis, *Higgs Constraints from Vector Boson Fusion and Scattering*,  
 2163 *JHEP* **04** (2015) 030, arXiv:1502.02990 [hep-ph]. 5.0.2, 5.0.3
- 2164 [51] M. Szleper, *The Higgs boson and the physics of WW scattering before and after Higgs*  
 2165 *discovery*, arXiv:1412.8367 [hep-ph]. 5.0.2
- 2166 [52] E. Accomando, A. Ballestrero, A. Belhouari, and E. Maina, *Isolating Vector Boson Scattering*  
 2167 *at the LHC: Gauge cancellations and the Equivalent Vector Boson Approximation vs complete*  
 2168 *calculations*, *Phys. Rev.* **D74** (2006) 073010, arXiv:hep-ph/0608019 [hep-ph]. 5.0.2
- 2169 [53] P. Anger, B. Axen, et al., *Same Sign  $W^\pm W^\pm$  Production and Limits on Anomalous Quartic*  
 2170 *Gauge Couplings*, Tech. Rep. ATL-COM-PHYS-2013-990, CERN, Geneva, Jul, 2013.  
 2171 <https://cds.cern.ch/record/1561731>. Internal note for approved paper STDM-2013-06.  
 2172 5.0.3, 5.1, 5.7

- 2173 [54] J. Almond, L. Bianchini, et al., *Search for heavy neutrino,  $W_R$  and  $Z_R$  gauge bosons in events*
- 2174 *with two high- $P_T$  leptons and jets with the ATLAS detector in pp collisions at  $\sqrt{s} = 8$  TeV*,
- 2175 Tech. Rep. ATL-COM-PHYS-2013-810, CERN, Geneva, Jun, 2013.
- 2176 <https://cds.cern.ch/record/1555805>. Supporting note for EXOT-2012-24, published as
- 2177 JHEP07 (2015) 162. 5.0.4
- 2178 [55] ATLAS Collaboration, M. Aaboud et al., *Luminosity determination in pp collisions at  $\sqrt{s} = 8$  TeV using the ATLAS detector at the LHC*, Eur. Phys. J. **C76** (2016) no. 12, 653,
- 2179 [arXiv:1608.03953 \[hep-ex\]](https://arxiv.org/abs/1608.03953). 5.1
- 2180 [56] G. Avoni et al., *The new LUCID-2 detector for luminosity measurement and monitoring in ATLAS*, JINST **13** (2018) no. 07, P07017. 5.1
- 2181 [57] ATLAS Collaboration, G. Aad et al., *The ATLAS Simulation Infrastructure*, Eur. Phys. J. **C70** (2010) 823–874, [arXiv:1005.4568 \[physics.ins-det\]](https://arxiv.org/abs/1005.4568). 5.1.1
- 2182 [58] S. Agostinelli et al., *GEANT4 - a simulation toolkit*, Nucl. Instrum. Meth. **A506** (2003)
- 2183 250–303. 5.1.1
- 2184 [59] T. Sjostrand, S. Mrenna, and P. Skands, *A Brief Introduction to PYTHIA 8.1*, Comput. Phys. Commun. **178** (2008) 852–867, [arXiv:0710.3820 \[hep-ph\]](https://arxiv.org/abs/0710.3820). 5.1.1
- 2185 [60] T. Gleisberg et al., *Event generation with SHERPA 1.1*, JHEP **02** (2009) 007,
- 2186 [arXiv:0811.4622 \[hep-ph\]](https://arxiv.org/abs/0811.4622). 5.1.1
- 2187 [61] S. Schumann and F. Krauss, *A parton shower algorithm based on Catani-Seymour dipole*
- 2188 *factorization*, JHEP **03** (2008) 038, [arXiv:0709.1027 \[hep-ph\]](https://arxiv.org/abs/0709.1027). 5.1.1
- 2189 [62] S. Höche, F. Krauss, S. Schumann, and F. Siegert, *QCD matrix elements and truncated*
- 2190 *showers*, JHEP **05** (2009) 053, [arXiv:0903.1219 \[hep-ph\]](https://arxiv.org/abs/0903.1219). 5.1.1
- 2191 [63] R. D. Ball et al., *Parton distributions for the LHC Run II*, JHEP **04** (2015) 040,
- 2192 [arXiv:1410.8849 \[hep-ph\]](https://arxiv.org/abs/1410.8849). 5.1.1
- 2193 [64] S. Alioli, P. Nason, C. Oleari, and E. Re, *A general framework for implementing NLO*
- 2194 *calculations in shower Monte Carlo programs: the POWHEG BOX*, JHEP **06** (2010) 043,
- 2195 [arXiv:1002.2581 \[hep-ph\]](https://arxiv.org/abs/1002.2581). 5.1.1
- 2196 [65] A. Ballestrero et al., *Precise predictions for same-sign W-boson scattering at the LHC*, Eur. Phys. J. **C78** (2018) no. 8, 671, [arXiv:1803.07943 \[hep-ph\]](https://arxiv.org/abs/1803.07943). 5.1.1
- 2197 [66] J. Alwall, R. Frederix, S. Frixione, V. Hirschi, F. Maltoni, O. Mattelaer, H. S. Shao,
- 2198 T. Stelzer, P. Torrielli, and M. Zaro, *The automated computation of tree-level and*
- 2199 *next-to-leading order differential cross sections, and their matching to parton shower*
- 2200 *simulations*, JHEP **07** (2014) 079, [arXiv:1405.0301 \[hep-ph\]](https://arxiv.org/abs/1405.0301). 5.1.1
- 2201 [67] H.-L. Lai, M. Guzzi, J. Huston, Z. Li, P. M. Nadolsky, J. Pumplin, and C. P. Yuan, *New*
- 2202 *parton distributions for collider physics*, Phys. Rev. D **82** (2010) 074024, [arXiv:1007.2241](https://arxiv.org/abs/1007.2241)
- 2203 [\[hep-ph\]](https://arxiv.org/abs/hep-ph/0603175). 5.1.1
- 2204 [68] T. Sjostrand, S. Mrenna, and P. Skands, *PYTHIA 6.4 physics and manual*, JHEP **05** (2006)
- 2205 026, [arXiv:0603175 \[hep-ph\]](https://arxiv.org/abs/0603175). 5.1.1

- 2211 [69] ATLAS Collaboration, G. Aad et al., *Muon reconstruction performance of the ATLAS*  
 2212 *detector in proton-proton collision data at  $\sqrt{s} = 13$  TeV*, Eur. Phys. J. **C76** (2016) no. 5, 292,  
 2213 arXiv:1603.05598 [hep-ex]. 5.2.1.1, 12
- 2214 [70] ATLAS Collaboration, *Electron efficiency measurements with the ATLAS*  
 2215 *detector using the 2015 LHC proton-proton collision data*, Tech. Rep.  
 2216 ATLAS-CONF-2016-024, CERN, Geneva, Jun, 2016.  
 2217 <https://cds.cern.ch/record/2157687>. 5.2.1.2
- 2218 [71] M. Cacciari, G. P. Salam, G. Soyez, *The anti- $k_t$  jet clustering algorithm*, JHEP **04** (2008) 063,  
 2219 arXiv:0802.1189 [hep-ph]. 5.2.1.3, 6.4.1
- 2220 [72] ATLAS Collaboration, M. Aaboud et al., *Jet energy scale measurements and their systematic*  
 2221 *uncertainties in proton-proton collisions at  $\sqrt{s} = 13$  TeV with the ATLAS detector*, Phys.  
 2222 Rev. **D96** (2017) no. 7, 072002, arXiv:1703.09665 [hep-ex]. 5.2.1.3
- 2223 [73] *Tagging and suppression of pileup jets with the ATLAS detector*, Tech. Rep.  
 2224 ATLAS-CONF-2014-018, CERN, Geneva, May, 2014.  
 2225 <http://cds.cern.ch/record/1700870>. 5.2.1.3
- 2226 [74] D. Adams, C. Anastopoulos, et al., *Recommendations of the Physics Objects and Analysis*  
 2227 *Harmonisation Study Groups 2014*, Tech. Rep. ATL-PHYS-INT-2014-018, CERN, Geneva,  
 2228 Jul, 2014. <https://cds.cern.ch/record/1743654>. 5.2.1.4
- 2229 [75] ATLAS Collaboration, M. Aaboud et al., *Measurement of the cross-section for producing a  $W$*   
 2230 *boson in association with a single top quark in  $pp$  collisions at  $\sqrt{s} = 13$  TeV with ATLAS*,  
 2231 JHEP **01** (2018) 063, arXiv:1612.07231 [hep-ex]. 5.2.1.4
- 2232 [76] ATLAS Collaboration, M. Aaboud et al., *Performance of missing transverse momentum*  
 2233 *reconstruction with the ATLAS detector using proton-proton collisions at  $\sqrt{s} = 13$  TeV*, Eur.  
 2234 Phys. J. **C78** (2018) no. 11, 903, arXiv:1802.08168 [hep-ex]. 5.2.2
- 2235 [77] ATLAS Collaboration, M. Aaboud et al., *Measurements of  $b$ -jet tagging efficiency with the*  
 2236 *ATLAS detector using  $t\bar{t}$  events at  $\sqrt{s} = 13$  TeV*, JHEP **08** (2018) 089, arXiv:1805.01845  
 2237 [hep-ex]. 5.2.2
- 2238 [78] J.-F. Arguin, J. Claude, G. Gonella, B. P. Kersevan, K. Koneke, K. Lohwasser, K. Mochizuki,  
 2239 M. Muskinja, C. Piaulet, and P. Sommer, *Support Note for Electron ID: charge*  
 2240 *mis-identification*, Tech. Rep. ATL-COM-PHYS-2017-1014, CERN, Geneva, Jul, 2017.  
 2241 <https://cds.cern.ch/record/2273365>. 5.3.3
- 2242 [79] C.-H. Kom and W. J. Stirling, *Charge asymmetry in  $W + \text{jets}$  production at the LHC*, Eur.  
 2243 Phys. J. **C69** (2010) 67–73, arXiv:1004.3404 [hep-ph]. 5.4
- 2244 [80] R. Steerenberg, *LHC Report: Another run is over and LS2 has just begun...*,  
 2245 [https://home.cern/news/news/accelerators/](https://home.cern/news/news/accelerators/lhc-report-another-run-over-and-ls2-has-just-begun)  
 2246 [lhc-report-another-run-over-and-ls2-has-just-begun](https://home.cern/news/news/accelerators/lhc-report-another-run-over-and-ls2-has-just-begun), 2018. Accessed: 2018-12-14. 6
- 2247 [81] *Letter of Intent for the Phase-I Upgrade of the ATLAS Experiment*, Tech. Rep.  
 2248 CERN-LHCC-2011-012. LHCC-I-020, CERN, Geneva, Nov, 2011.  
 2249 <https://cds.cern.ch/record/1402470>. 6

- 2250 [82] G. Apollinari, I. Bjar Alonso, O. Brning, M. Lamont, and L. Rossi, *High-Luminosity Large*  
2251 *Hadron Collider (HL-LHC): Preliminary Design Report*. CERN Yellow Reports: Monographs.  
2252 CERN, Geneva, 2015. <https://cds.cern.ch/record/2116337>. 6
- 2253 [83] ATLAS Collaboration Collaboration, ATLAS Collaboration, *ATLAS Phase-II Upgrade*  
2254 *Scoping Document*, Cern-lhcc-2015-020, Geneva, Sep, 2015.  
2255 <http://cds.cern.ch/record/2055248>. 6
- 2256 [84] D. Espriu and B. Yencho, *Longitudinal WW scattering in light of the “Higgs boson”*  
2257 *discovery*, Phys. Rev. D **87** (2013) 055017, arXiv:1212.4158 [hep-ph]. 6, 6.1
- 2258 [85] ATLAS Collaboration Collaboration, *Prospects for the measurement of the  $W^\pm W^\pm$  scattering*  
2259 *cross section and extraction of the longitudinal scattering component in pp collisions at the*  
2260 *High-Luminosity LHC with the ATLAS experiment*, Tech. Rep. ATL-PHYS-PUB-2018-052,  
2261 CERN, Geneva, Dec, 2018. <http://cds.cern.ch/record/2652447>. 6
- 2262 [86] ATLAS Collaboration Collaboration, *Studies on the impact of an extended Inner Detector*  
2263 *tracker and a forward muon tagger on  $W^\pm W^\pm$  scattering in pp collisions at the*  
2264 *High-Luminosity LHC with the ATLAS experiment*, Tech. Rep. ATL-PHYS-PUB-2017-023,  
2265 CERN, Geneva, Dec, 2017. <https://cds.cern.ch/record/2298958>. 6
- 2266 [87] T. Sjöstrand, S. Ask, J. R. Christiansen, R. Corke, N. Desai, P. Ilten, S. Mrenna, S. Prestel,  
2267 C. O. Rasmussen, and P. Z. Skands, *An Introduction to PYTHIA 8.2*, Comput. Phys.  
2268 Commun. **191** (2015) 159–177, arXiv:1410.3012 [hep-ph]. 6.2
- 2269 [88] ATLAS Collaboration Collaboration, *Expected performance for an upgraded ATLAS detector*  
2270 *at High-Luminosity LHC*, Tech. Rep. ATL-PHYS-PUB-2016-026, CERN, Geneva, Oct, 2016.  
2271 <http://cds.cern.ch/record/2223839>. 6.3
- 2272 [89] P. C. Bhat, H. B. Prosper, S. Sekmen, and C. Stewart, *Optimizing Event Selection with the*  
2273 *Random Grid Search*, Comput. Phys. Commun. **228** (2018) 245–257, arXiv:1706.09907  
2274 [hep-ph]. 6.5.1
- 2275 [90] G. Cowan, K. Cranmer, E. Gross, and O. Vitells, *Asymptotic formulae for likelihood-based*  
2276 *tests of new physics*, Eur. Phys. J. **C71** (2011) 1554, arXiv:1007.1727 [physics.data-an].  
2277 [Erratum: Eur. Phys. J.C73,2501(2013)]. 6.5.1